Weill Cornell Medicine
Anesthesiology

15th Annual Research Exposition

75 YEARS OF EXCELLENCE

Tuesday
October 31, 2023

Oral Presentations
3:00-4:00 pm in M309

Special Research Seminar
4:00-4:30 pm in M309

Reception
4:30-5:00 pm outside P300

Poster Presentations
5:00-6:00 pm in P300

3:00-4:00 pm

Oral Presentations

"High-speed atomic force microscopy captures a rare and transient protein state"

Shifra Lansky, PhD
The Scheuring Lab
Weill Cornell Medicine

"Chronic pain, deportation stress, and cardiovascular risk in refugee torture survivors: determining the links and establishing a diagnostic system"

Gunisha Kaur, MD, MA
Associate Professor of Anesthesiology
Director of Human Rights Impact Lab
Co-Medical Director of Weill Cornell Center for Human Rights
Weill Cornell Medicine

"Multi-omics for Precision Medicine and Health Intelligence"

Joseph Scarpa, MD, PhD
Van Poznak Research Scholar
Liver Transplant Anesthesia Fellow
Instructor, Department of Anesthesiology
Weill Cornell Medicine

4:00-4:30 pm

Special Research Seminar

"Speeding Recovery from Pain and Disability After Surgery"

James C. Eisenach, MD
FM James III, Professor of Anesthesiology
Wake Forest University School of Medicine
Winston Salem, NC
President, Foundation for Anesthesia Education and Research

Department of Anesthesiology • 525 East 68th Street, P3
For more information contact: **Michele Steinkamp, RN**
212-746-2953 or mls9004@med.cornell.edu

WELCOME TO THE 15TH ANESTHESIOLOGY RESEARCH EXPOSITION

October 31st 2023

Oral Presentations

"High-speed atomic force microscopy captures a rare and transient protein state"

Shifra Lansky, PhD
The Scheuring Lab
Weill Cornell Medicine

"Chronic pain, deportation stress, and cardiovascular risk in refugee torture survivors: determining the links and establishing a diagnostic system"

Gunisha Kaur, MD, MA
Associate Professor of Anesthesiology
Director of Human Rights Impact Lab
Co-Medical Director of Weill Cornell Center for Human Rights
Weill Cornell Medicine

"Multi-omics for Precision Medicine and Health Intelligence"

Joseph Scarpa, MD, PhD
Van Poznak Research Scholar
Liver Transplant Anesthesia Fellow
Instructor, Department of Anesthesiology
Weill Cornell Medicine

3:00 – 4:00pm, M309

Special Research Seminar

"Speeding Recovery from Pain and Disability After Surgery"

James C. Eisenach, MD
FM James III, Professor of Anesthesiology
Wake Forest University School of Medicine Winston Salem, NC
President, Foundation for Anesthesia Education and Research

4:00pm – 4:30pm, M309

Reception

4:30pm – 5:00pm
Outside P300

Poster Presentations

5:00pm – 6:00pm
P300

Table of Contents

Department of Anesthesiology Research Divisions

Hugh C. Hemmings, Jr, MD, PhD, FRCA
Senior Associate Dean of Research
Joseph F. Artusio Professor
Chair of Anesthesiology

Kane O. Pryor, MD
Executive Vice Chair for Academic Affairs
Director of Clinical Research
Director of Education

Hannah Wunsch, MD
Vice Chair for Research
Director of Outcomes Research

Anesthesia Trials Group

Kane O. Pryor, MD **Lisbeth A. Evered, PhD**

David Cabello, BS
Claudia Hatef, BS
Nidhi Kanchumarthi, BA
Abha Kasubhai, BA
Avika Kasubhai, BA
Michele Steinkamp, RN
Hannah Leibowitz, BS
Jay Sangwan, BS
Jessica Wang, BA
Julianna Zeepvat, BS

Center for Perioperative Outcomes

Zachary A. Turnbull, MD, MBA, MS

Silis Y. Jiang, PhD
Camdyn Anders, BS
Raquel Cyril, BS
Abbey Gilman, BS
Suma Gopal, BS
Briana Lui, BS
Samson Obembe, BS
Melissa Sanchez, BS
Virginia Tangel, MA, MSc

High-Speed Atomic Force Microscopy Laboratory

Simon Scheuring, MS, PhD

Atsushi Miyagi, MS, PhD
Motonori Imamura, PhD
Shifra Lansky, PhD
Yangang Pan, PhD
Sichen Pan, PhD
Runze Ma, PhD
Linlin Li, PhD
Eun-Ji Shin, PhD
Tim John Joseph, PhD
Zhaokun Wang
Yining Jiang, PhD
John (Michael) Betancourt

Paul Riegelhaupt, MD, PhD

Leila Khajoueinejad, PhD
Elena Riel, PhD
Gagandeep Singh, BS

Daniel Cook, MD

Laboratory of Molecular Anesthesiology

Hugh C. Hemmings, Jr, MD, PhD, FRCA
Jimcy Platholi, PhD

Karl Herold, MD, PhD
Irem Atasoy, PhD
Kishan Patel, BS
Azliana Jafri, PhD
Jiabin Tang, PhD
Jiaxin "Jessica" Xiang, MEng
Donghang Zhang, MD, PhD
Alexander Donatelle, BA
Cameron Swope, BS

Alessio Accardi, PhD

Eleanora Di Zanni, PhD
Sangyun Lee, PhD
Zheng Fang, PhD
Omar Alvarenga, BA
David Ballesteros Gomez
Nicole Rychlik, MS

Crina Nimigean, PhD

Elizabeth Kim, PhD
Shubhangi Agarwal, PhD
TaeHyun Park, PhD
Chieh-Chin Li, PhD
Hee-Seop Yoo, PhD

CV Starr Laboratory for Molecular NeuroPharmacology

Latrice C. Goss, BS
Nithatari Cornibert
Cynthia L. Guzman

Diany Paola Calderon, MD, PhD

Iryna Popovych, PhD
Amanda Simon, BA

Peter A. Goldstein, MD

Gareth Tibbs, PhD
Tristan Wellner, BS

Jyun-you Liou, MD, PhD

Aditya Iyer, BS

Department of Anesthesiology Research Divisions

General Clinical Research

Noemi Balogh, MD
Seema Brar, MD
Eric D. Brumberger, MD
Lisbeth Evered, PhD
Farida Gadalla, MD
Peter Goldstein, MD
Shreyajit Kumar, MD
Philip Kuo, MD
Christine Lennon, MD
Jaideep Malhotra, MD
Danielle McCullough, MD
Matthew Murrell, MD, PhD
Anup Pamnani, MD
Rohan Panchamia, MD
Kane Pryor, MD
Melinda Randall, MD
John Rubin, MD
Lori Rubin, MD
Jon Samuels, MD
Jacques Scharoun, MD
Liang Shen, MD
Sheida Tabaie, MD

Human Rights Impact Lab

Gunisha Kaur, MD, MA
Richard Boyer, MD, PhD
Leslie Bull, MA
Celeste Cheung, BS
Nihan Ercanli
Claudia Hatef, BS
Jacob Lurie, MD, MPH
Omri Maayan, BS
Andrew Milewski, MD, PhD
Tanzilya Oren, PhD
Luiza Perez, BA
Harlan Pietz, BS
Sanjana Ravi, BS
Sheida Tabaie, MD
Samantha Tham, BA
Sargun Virk, MD

Pain Clinical Research

Neel Mehta, MD
Shakil Ahmed, MBBS
Alina Boltunova, MD
Jatin H. Joshi, MD
Rohan Jotwani, MD, MBA
Tiffany Lin, MD
Daniel Pak, MD
Philip Petrou, MD
Mohammad Piracha, MD, MBA, MSc
Lisa R. Witkin, MD, MS

Pediatrics Clinical Research

Aarti Sharma, MD
Michael Green, MD
Jennifer Lee, MD
Jyun-you Liou, MD, PhD
Roshan Patel, MD

Cardiac Clinical Research

Meghann Fitzgerald, MD
Natalia Ivascu Girardi, MD
Shanna Sykes Hill, MD
Marguerite Hoyler, MD
Mandisa-Maia Jones, MD
Diana Khatib, MD
Adam Lichtman, MD
Sagar Navare, MD
James Osorio, MD
Olga Rozental, MD, PhD
Ankur Srivastava, MD
Maria Walline, MD

Dr. Rong Research Team

Lisa Q. Rong, MD
Bassam Osman, MD

Obstetrics/Gynecological Clinical Research

Jaime Aaronson, MD
Sharon Abramovitz, MD
Farida Gadalla, MD
Hilary Gallin, MD
Michael Kim, MD
Klaus Kjaer, MD
Robert White, MD, MS

Education Research

Kane Pryor, MD
June Chan, MD
Ruth Gotian, EdD, MS
Dana Gurvitch, MD
Rohan Jotwani, MD, MBA
Deirdre Clare Kelleher, MD
Daniel Pak, MD
Liang Shen, MD
John Rubin, MD

MADE Lab

Richard Boyer, MD, PhD
Iqram Hussein, PhD
Seyed Safavynia, MD, PhD
Joseph Scarpa, MD, PhD
Julia Scarpa, MD, PhD

Regional Anesthesia Clinical Research

Tiffany Tedore, MD
Neil Borad, MD
Justin Chung, MD
Rohan Jotwani, MD, MBA
John Rubin, MD
Nicolas Salvatierra, MD, MBA
Marissa Weber, MD

Department of Population Health Sciences Division of Biostatistics and Epidemiology

Paul Christos, DrPH, MS
Linda Gerber, PhD
Jessica Kim, MS
Brady Rippon, MS

P-03 Poster Map

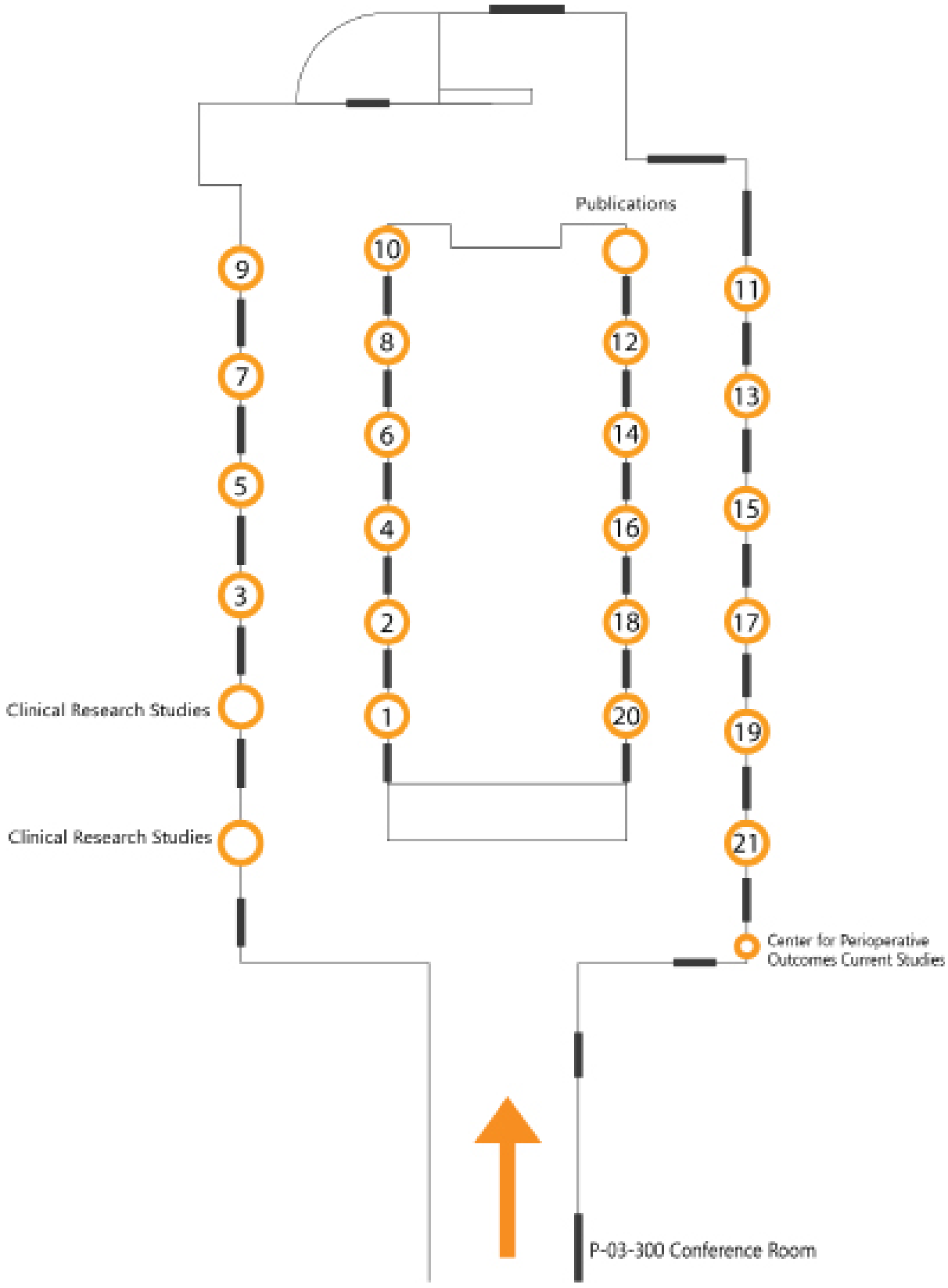

P-03 Poster Map Key

1. **Evaluation of Wearables for Preoperative Cardiorespiratory Fitness Screening and Risk Stratification in Geriatric Surgery**
   Richard Boyer, Iqram Hussain, Julianna Zeepvat, Cary Reid, Sara Czaja, Kane Pryor

2. **Reported Methods, Distributions, and Frequencies of Torture Globally: A Systematic Review and Meta-Analysis**
   Andrew Milewski MD PhD, Eliana Weinstein BS, Jacob Lurie MD MPH, Annabel Lee BA, Faten Taki PhD, Tara Pilato MD, Caroline Jedlicka MLS MSW, Gunisha Kaur MD MA

3. **Machine Learning-based Detection of Intraoperative Ischemia Utilizing the VitalDB Database**
   Iqram Hussain, Balaji Pandian, Julianna Zeepvat, Antonis A. Armoundas, Richard Boyer

4. **Neurophysiological correlates of delayed recovery of consciousness in a critically-ill COVID-19 patient with repeated cardiac arrest**
   Seyed A. Safavynia MD PhD, Jessica Wang BA, Jacky M. Choi MPH, Natalia Roszkowska BS, Joseph Chiaro DO, Padmaja Kandula MD, Sophia Hu, Jonathan D. Victor MD PhD, Nicholas D. Schiff MD

5. **Variation in Internal and External Respiratory Motions among Healthy Volunteers**
   Andrew Milewski MD PhD, Guang Li PhD

6. **United States rural residence is associated with increased acute maternal end-organ injury or mortality after birth: a retrospective multi-state analysis, 2007–2018**
   Rahul Chaturvedi MD, Briana Lui BS, Virginia Tangel MA MSc, Sharon E. Abramovitz MD, Kane O. Pryor MD, Grace Lim MD MS, Robert S. White MD MS

7. **Accurate prediction of respiratory motion using long, short-term—memory deep learning**
   Andrew R. Milewski, Fayed Uddin, Vyas Gupta, Xingyu Nie, Guang Li

8. **Larger Decrease From Baseline Transglomerular Pressure Gradient Associated With Acute Kidney Injury In Cardiac Surgical Population**
   Ryan Price MD, Sanya Rastogi BS, Christina Zecca MD, Klint Smart MD, Emily Eruysal MD, Avika Kasubhai BA, Sagar Navare MD, James Osorio MD, Christopher Lau MD, Ankur Srivastava MD

9. **Overlap between perioperative neurocognitive disorders and long covid**
   Dylan Bitensky BS, Hannah Leibowitz BS, Seyed A. Safavynia MD PhD, Lisbeth A. Evered MSc PhD

10. **An artificial intelligence-powered, patient-centric digital tool for self-management of chronic pain: A prospective, multicenter clinical trial**
    Maria L. Rosén Klement PhD, Antje M. Barreveld MD, Sophia Cheung, Ulrika Axelsson PhD, Jade I. Basem, Anika S. Reddy, Carl AK Borrebaeck DSc, Neel Mehta MD

11. **Improving Response to Routine and Difficult Airways at Weill Cornell Medicine/ NewYork-Presbyterian Hospital**
Ingharan Siddarthan MD, Emily Rose Eruysal MD, Rahul Chaturvedi MD, Amal Mansur Javaid MD, Michelle Tiangco MS, Deirdre C. Kelleher MD

12. **Multilevel Social Determinants of Health Disparities In Postpartum Readmissions In The United States: A Multistate Analysis 2015-2020**
Briana Lui BS, Elizabeth Khusid BA, Virginia E. Tangel MA MSc, Silis Y. Jiang PhD, Sharon E. Abramovitz MD, Corrina M. Oxford MD, Robert S. White MD MS

13. **Carotid Doppler Imaging Correlation with Pulmonary Artery Catheters As A Marker For Fluid Responsiveness**
James Osorio MD, Ankur Srivastava MD, Samir Sethi MD, Natalia Ivascu Girardi MD, Leonard Girardi MD, Mario Gaudino MD, Brady Rippon MS, Joydeep Baidya BS, Sanya Rastogi BS, Alexandra Lopes BA, Avika Kasubhai BA, Kane Pryor MD

14. **The IMPACT Score: Does Sex Matter?**
Mandisa Jones MD, Virginia Tangel MA MSc, Robert S. White MD MS, Lisa Q. Rong MD MSCE

15. **Measuring Ascending Aortic Aneurysms with Intraoperative TEE: Validation via CMR**
Lisa Q. Rong MD, Sena Chun MD, Hannah Agoglia BA, Pablo Villar Calle MD, Richard Thalappillil MD, Andrew Martinez BA, Aneri Patel BA, Jiwon Kim MD, Leonard N. Girardi MD, Richard B. Devereux MD, Mario Gaudino MD PhD, Jonathan W. Weinsaft MD

16. **Perioperative Pulmonary Artery Catheter Use is Associated with Increased In-Hospital Mortality in Cardiac Surgical Patients: A Systematic Review and Meta-Analysis**
Grant Luhmann MM, Arnaldo Dimagli MD, Antonino Di Franco, Michelle Demetres MLS, Sena Chun MD, Lisa Q. Rong MD

17. **Distal Aortic Biomechanics after Transcatheter versus Surgical Aortic Valve Replacement**
William Zheng, Andrew Martinez, Richard Devereux MD, Jonathan Weinsaft MD, Mario Gaudino MD, Lisa Q. Rong MD

18. **Perioperative mortality in paediatric patients: a systematic review of risk assessment tools for use in the preoperative setting**
Virginia E. Tangel MA MSc, Stephan D. Krul, Robert Jan Stolker MD PhD, Wichor M. Bramer PhD, Jurgen C. de Graaff MD PhD, Sanne E. Hoeks PhD

19. **Gender Difference in Authorship and Quality of Anesthesia Clinical Practice Guidelines from 2016-2020 using the Appraisal of Guidelines for Research & Evaluation II Instrument**
Lisa Q. Rong, Andrew P. Martinez, Mohamed Rahouma, Alexandra J. Lopes, Jerry Y. Lee, Drew N. Wright, Michelle Demetres, Bessie Kachulis, Sinead M. O'Shaughnessy

20. **The Development and Analysis of a Chronic Pain & Multidisciplinary Spine Outcomes Registry**
Lisa R. Witkin MD MS, Jacky Choi MPH, Jessica Kim MS, Abbey Gilman BS, Silis Jiang PhD, Abha Kasubhai BA, Jonathan Tobin PhD

21. **Multicenter Perioperative Outcomes Group (MPOG)**
WCM MPOG Leadership: Hugh Hemmings MD PhD, Patricia Mack MD, Kane Pryor MD, Zachary Turnbull, MD MBA MS

M Corridor Poster Map

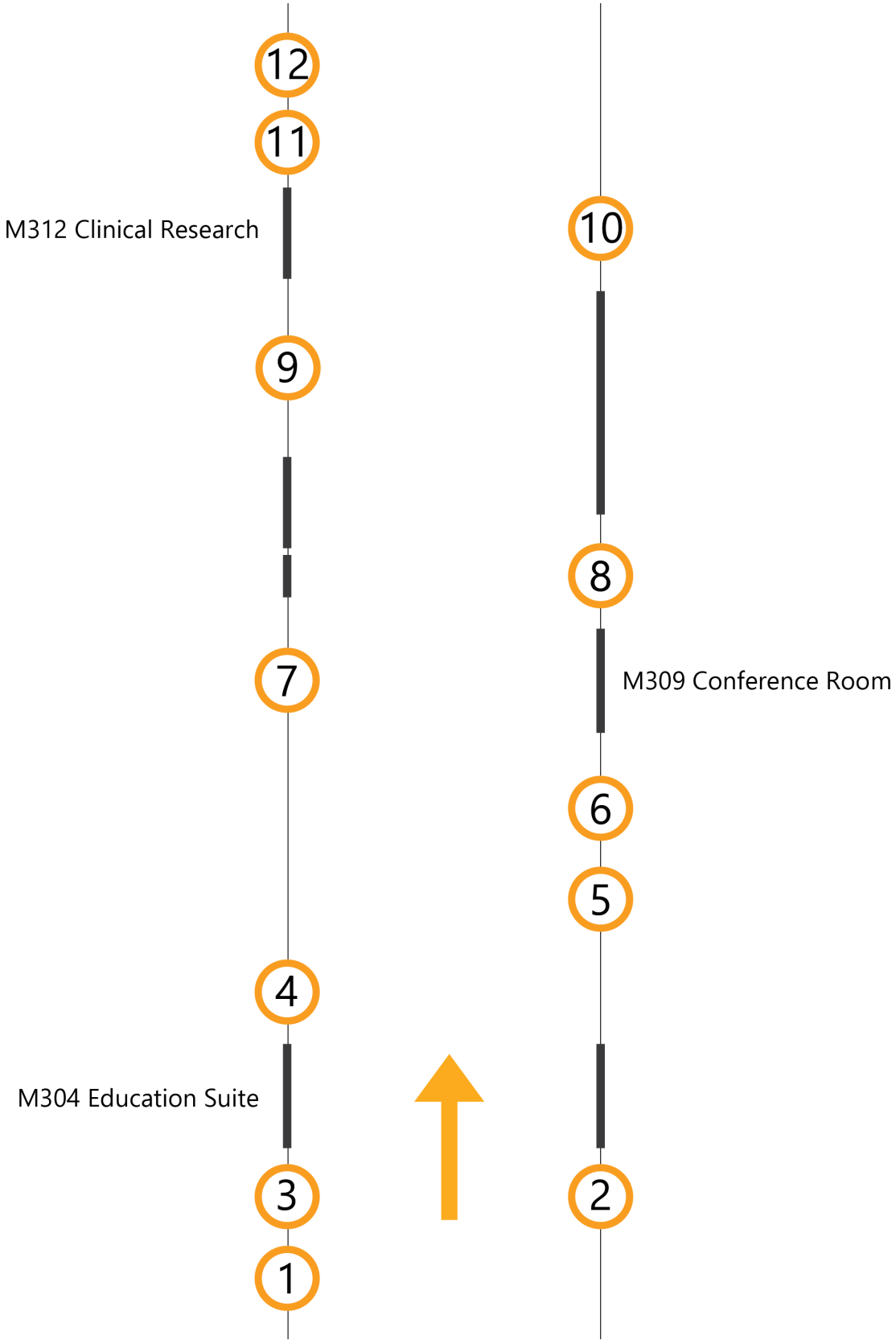

M Corridor Poster Map Key

1. **Engineering novel pharmacology for the TREK1 K2P channel**
   Leila Khajoeinejad, Elena Riel, Gagandeep Singh, Paul M. Riegelhaupt

2. **High-Resolution (3.3 Å) Cryo-EM 3D model of the TASK-1 K2P Channel**
   Gagandeep Singh, Paul Riegelhaupt

3. **Engineering an off-switch for background TREK1 potassium channels**
   Elena B. Riel, Louis Goldberg, Paul Riegelhaupt

4. **Isoflurane alters presynaptic endoplasmic reticulum calcium dynamins in Wild-Type and malignant hypothermia susceptible rodent hippocampal neurons**
   Vanessa Osman PhD, Iris Speigel PhD, Kishan Patel, Hugh C. Hemmings Jr MD PhD

5. **Propofol restores HCN1 epilepsy mutants and reveals non-canonical voltage-dependent gating in HCN channels**
   Elizabeth D. Kim, Xiaoan Wu, Sangyun Lee, Gareth R. Tibbs, Kevin P. Cunningham, Marta E. Perez, Peter A. Goldstein, Alessio Accardi, H. Peter Larsson, and Crina M. Nimigean

6. **Calcium-gated potassium channel blockade via membrane-facing fenestrations**
   Chen Fan, Emelie Flood, Nattakan Sukomon, Shubhangi Agarwal, Toby W. Allen, Crina M. Nimigean

7. **HS-AFM Single-Molecule Structural Biology Uncovers Basis of Transporter Wanderlust Kinetics**
   Yining Jiang, Simon Scheuring

8. **Synaptic metabolic vulnerability is cell- and phenotype-specific in hippocampal neurons from rats**
   Daniel Cook MD, Kirsten Bredvik BS, Timothy Ryan PhD

9. **Blast injury induces sex-dependent changes in structural connectivity along nociceptive fiber tracts**
   Amanda Simon, Keith Jamison, Iryna Popovych, Amy Kuceyeski, Paola Calderon

10. **Structural basis of pH-dependent activation in CLC transporters**
    Eva Fortea, Sangyun Lee, Rahul Chadda, Janice L. Robertson, Olga Boudker, Alessio Accardi

11. **Cryo-EM structures and functional characterization of the human TMEM16E protein and GDD associated mutations**
    Eleonora Di Zanni, Nicole Rychlik, Zhang Feng, Elizabeth D. Kim, Alessio Accardi

12. **Structural basis of closed groove scrambling by a TMEM16 protein**
    Zhang Feng, Omar Alvarenga, Alessio Accardi

Clinical Research, Quality Improvement, and Center for Perioperative Outcomes Posters

MADE
Medical Accelerator & Digital Engineering

Weill Cornell Medicine
Anesthesiology

Evaluation of Wearables for Preoperative Cardiorespiratory Fitness Screening and Risk Stratification in Geriatric Surgery

Richard Boyer[1], Iqram Hussain[1], Julianna Zeepvat[1], Cary Reid[2], Sara Czaja[2], Kane Pryor[1]

1. Department of Anesthesiology, Weill Cornell Medicine, New York, NY
2. Division of Geriatrics and Palliative Medicine, Weill Cornell Medicine, New York, NY

FAER
Foundation for Anesthesia Education and Research

NIH National Institute on Aging

Introduction

- Poor cardiorespiratory fitness (CRF) is a major contributor to increased surgical risk in older adults.
- Several studies have shown that preoperative CRF, as measured by maximal oxygen uptake (VO2max), is highly predictive of surgical morbidity and mortality.
- Consumer wearable health and fitness monitors are capable of accurately predicting VO2max as compared to indirect calorimetry and the 6-minute walk test (6MWT) in young, healthy adults.
- Wearable estimates of CRF have not been rigorously studied in older adults for surgical risk stratification.

Methods

- Utilizing data from older adults scheduled for major surgery, this prospective, observational clinical study evaluates 1) the agreement of wearable VO2max, 6-MWD and CPET VO2max, and 2) the correlation of wearable CRF metrics with postoperative complications.

Wearable Features Assessed – Definitions

Activity States & Metabolic Equivalent of Task (MET):

- Light activity: 1<METs2
- Moderate activity: 2<METs4
- Heavy activity: 4<METs6
- Extreme activity: 6<MET

Heart Rate Variability (HRV) Features:

- SDNN, RMSSD, and SDSD
- pNN50
- Respiratory Sinus Arrhythmia (RSA)
- LF/(LF + HF), HF/(LF + HF), LF/HF
- Entropy
- Fractal Detraction analysis (DFA1, DFA2)
- Poincare plot (Slope)

Heart Rate (HR) Recovery Features:

- 5th min HR recovery
- 4th min HR recovery
- 3rd min HR recovery
- 2nd min HR recovery
- 1st min HR recovery

Other Features

- aEEmax , HR slope/work (calories) , HR intercept/work (calories)

Target Variable: VO2peak estimated

Equation for Estimated VO2 Peak

*VO2max_6MWT = 59.44 - 3.83 * gender - 0.56 (age_years + age_months /12) - 0.48 * bmi + 0.04 * 0.3048 * mwt_distance*

Feature Selection: SelectKBest (feature with highest 20 kernel scores)
Machine-learning algorithms: Random forest regressor, Linear regression.
Machine-learning library & platform: Anaconda, JupyterLab 4.0.7, Scikit-learn, Python 3.11.4
Explainable AI: Interpretation of ML models → Shapley Additive Explanations (SHAP)

Hypothesis

We conducted a prospective, observational clinical study to test the hypothesis that wearable measurements of cardiorespiratory fitness (CRF) are predictive of postoperative complications in older adult patients undergoing major surgery.

Results

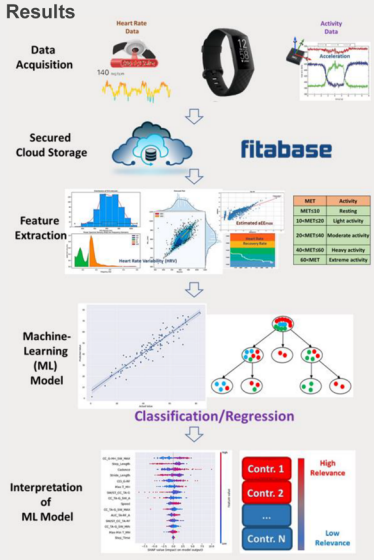

Figure 1: *Overview of methodology for estimation of Maximal Oxygen Uptake (VO2peak) through wearable Fitness tracker using machine-learning approach.*

Results

- The coefficient of determination (R^2) of the regression model was 0.87 and 0.73 for estimating VO2peak using Random forest regressor and Linear regression, respectively.
- SHAP analysis revealed that HR recovery, non-linear HRV features, and HR/calories matrices have higher contributions in estimating VO2peak in Random forest model.
- SHAP analysis shows that HR features in diverse activity states, linear HRV, and HR/calories features have higher contributions in estimating VO2peak in linear regression model.

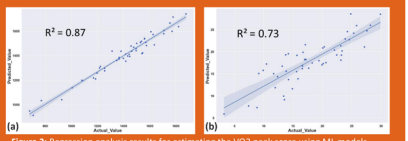

Figure 2: Regression analysis results for estimating the VO2 peak score using ML models based on wearable cardiorespiratory features. (a) Regression performance of Regression Random forest regression model, (b) Regression performance of Linear regression model.

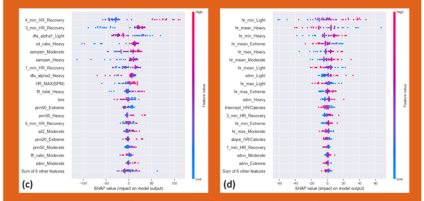

Figure 3: Interpretation of Regression model for estimating the VO2 peak score using SHAP based on wearable cardiorespiratory features. (c) SHAP analysis of Regression Random forest regression model, (d) SHAP analysis of Linear regression model.

Conclusions

- Wearable cardiorespiratory fitness monitors have strong potential for preoperative assessment of VO2peak in older adult surgical patients and is a promising tool for geriatric surgical risk stratification.

Reported Methods, Distributions, and Frequencies of Torture Globally:A Systematic Review and Meta-Analysis

Andrew Milewski, MD, PhD; ElianaWeinstein, BS; Jacob Lurie,MD, MPH; Annabel Lee, BA; Faten Taki, PhD; Tara Pilato, MD; Caroline Jedlicka, MLS, MSW; Gunisha Kaur,MD, MA

Background

Despite its prohibition by the United Nations Convention against Torture and other international treaties, torture has been perpetrated against countless individuals worldwide, and health care practitioners globally are increasingly encountering refugee torture survivors in their clinical practices. The methods, geographic distribution, and frequency of torture globally are not well described, which limits health care practitioners' ability to adequately diagnose and treat the sequelae of torture.

Methods

For this systematic review and meta-analysis, Ovid MEDLINE, Ovid Embase, Web of Science, and The Cochrane Library were searched from inception to July 2021. Included studies were peer-reviewed articles in English, contained an independent sample population of individuals who experienced torture, and outlined the type(s) of torture experienced. Excluded studies were not peer reviewed, lacked an independent sample population, or did not specify torture methods. Overall, 266 articles—15.3%of the 1739 studies initially identified for full review—met the inclusion criteria. Torture methods were ranked by their average frequencies, numbers of reporting studies, and numbers of countries wherein the methods occurred.

Table 1: Study Demographics

Number of tortured individuals per study	**Studies, No. (%) (N = 266)**
1 - 9	94 (35.3)
10 - 99	112 (42.1)
100 - 999	55 (20.7)
1,000 - 9,999	4 (1.5)
≧ 10,000	1 (0.4)
Number of reported torture methods per study	
1 - 10	198 (74.4)
11 - 20	58 (21.8)
21 - 30	7 (2.6)
≧ 31	3 (1.1)
Number of countries where torture was reported per study	
1	143 (53.8)
2 - 10	53 (19.9)
> 10	11 (4.1)
Country of torture could not be determined[a]	59 (22.2)
Gender(s) specified	
Men and women	113 (42.5)
Only men	82 (30.8)
Only women	27 (10.2)
Gender of could not be determined[b]	44 (16.5)
Gender of individuals across all articles	**Individuals, No. (%) (N = 103,604)**
Men	13,350 (12.9)
Women	5,610 (5.4)
Unspecified	84,644 (81.7)

[a]No country of torture was specified or only a multi-country region was specified.
[b]The gender of the participants was not specified for the study's entire sample or for the subsample that could be included for analysis.

Table 2: Top 10 Physical Torture Methods

Physical Torture Methods	Average frequency[a]	No. studies	No. countries
Beating or blunt-force trauma	62.4 (57.7-67.1)	208	59
Electrical torture	17.2 (15.0-19.4)	114	28
Starvation or dehydration	12.7 (10.2-15.2)	65	26
Foot whipping	12.6 (11.6-13.6)	65	23
Suspension	11.0 (8.3-13.7)	75	21
Asphyxiation or suffocation	8.9 (5.6-12.2)	68	21
Binding or restricted movement	8.3 (5.9-10.7)	51	21
Other forced positions	8.0 (7.0-9.0)	57	18
Sharp objects or penetrating trauma	7.8 (4.1-11.5)	65	24
Burning	6.9 (6.3-7.5)	84	25

[a]Average frequency reported as %, (95% CI)
The listed physical torture methods all ranked among the top ten physical methods by all three ranking strategies.

Fig. 1: Minimal Geographic Extent of Torture and the Migration of Torture Survivors

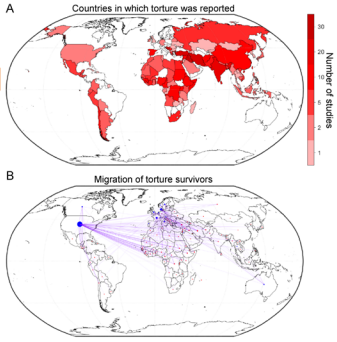

(B) Red and blue dots indicate where individuals were tortured and encountered for study, respectively. The size of the dots indicates the number of studies for which individuals reported torture or were encountered for study. Each purple line designates a single migratory pathway. Multiple pathways may arise from a single study. Only those studies that listed a single encounter location and listed locations of torture were used to generate the map, and locations of encounters that coincided with locations of torture are not shown. Consequently, data from 180 studies were included in the map.

Fig. 2: Similarity between Studies

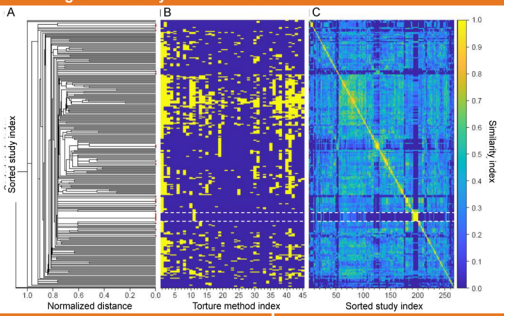

(A) A dendrogram shows the normalized distance between studies, indicated by the location of the vertical line that joins 2 or more studies. The branches of the dendrogram are arranged in an order that minimizes the distance between clusters. Red lines identify clusters wherein the reported torture methods overlap perfectly. (B) A matrix displays the torture methods that were reported by each study. (C) A heat map portrays the degree of similarity between each pair of studies. A higher similarity index indicates greater overlap in the number of torture methods reported by both studies. Several small clusters are seen, including a cluster of 9 studies (white, dashed lines) that reported only foot whipping.

Fig. 3: Differences in Torture-Method Frequencies between Men and Women

Torture	Men Yes/No	Women Yes/No	Conditional OR (95%CI)
Rape	41/9782	45/12674	0.03 (0.02-0.04)
Denailing	10/11777	25/4886	0.17 (0.08-0.35)
Sharp objects or penetrating trauma	49/6538	97/2939	0.23 (0.16-0.32)
Burning	62/6425	48/2672	0.52 (0.36-0.76)
Other psychological torture	918/4149	544/1500	0.61 (0.54-0.69)
Other physical torture	877/10420	287/4281	1.26 (1.09-1.44)
Beating or blunt-force trauma	1794/1579	652/986	1.72 (1.52-1.94)
Electrical torture	236/8302	63/4030	1.82 (1.37-2.41)
Sham executions	76/11637	15/4929	2.15 (1.23-3.74)
Witnessing torture	777/9384	118/2491	2.28 (1.86-2.91)
Whipping	68/12406	11/5120	2.55 (1.35-4.83)
Verbal abuse or threats	551/10104	76/4095	2.94 (2.31-3.74)
Isolation or solitary confinement	513/10570	64/4429	3.37 (2.59-4.38)
Other forced positions	368/8106	36/3115	3.93 (2.78-5.55)
Starvation or dehydration	191/11301	15/4604	5.19 (3.06-8.78)
Forced prolonged standing	162/10692	12/5021	6.34 (3.52-11.41)
Stripped naked	333/11537	20/4790	6.91 (4.40-10.87)
Foot whipping	300/9118	19/4539	7.86 (4.94-12.51)
Binding or restricted movement	91/11844	4/4885	9.59 (3.52-26.10)
Suspension	178/9763	7/4453	11.60 (5.45-24.70)
Other sexual torture	82/9891	3/4238	11.71 (3.70-37.09)
Exposure to bright light	301/11912	10/4920	12.43 (6.62-23.36)
Prevention of hygiene	157/11921	5/4900	12.91 (5.29-31.46)
Exposure to extreme hot or cold	507/10415	17/4902	14.04 (8.65-22.79)
Blindfolding	547/11283	7/4875	33.76 (16.03-71.21)
Sleep deprivation	506/11002	1/4741	218.65 (30.65-1551.38)

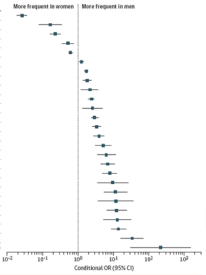

A forest plot depicts the conditional odds ratios (ORs) and 95%CIs for the torture methods that were reported more frequently for 1 gender. For every listed torture method, P < .006. Torture methods that were applied to only 1 gender had infinite odds ratios and are not included: female genital mutilation or cutting was reported only for women; gunshot, muscle crushing with roller (ghotna), deprivation of medical care, pharmacological torture, loud noises, and genital trauma were clearly reported only for men.

Results

A total of 9937 titles and abstracts were screened, and 266 studies encompassing103 604 individuals (13 350 men, 5610 women, and 84 644 unspecified) were analyzed. Torture was reported for 105 countries; 21 methods accounted for 84%of all reported methods and 10 methods accounted for 78%of all physical tortures. The top 3 methods were beating or blunt-force trauma (reported in 208 studies and 59 countries; average frequency, 62.4%; 95%CI, 57.7%-67.1%), electrical torture (reported in 114 studies and 28 countries; average frequency, 17.2%; 95%CI, 15.0%-19.4%), and starvation or dehydration (reported in 65 studies in 26 countries; average frequency, 12.7%; 95%CI, 10.2%-15.2%).

Conclusions

The findings of this study suggest that torture remains widespread. Although innumerable torture methods exist, a limited number account for the vast majority of reported tortures. So that targeted therapies may be developed, additional investigation is needed to better elucidate the sequelae associated with the most common torture methods, described here.

Machine Learning-based Detection of Intraoperative Ischemia Utilizing the VitalDB Database

Iqram Hussain [1], Balaji Pandian [1], Julianna Zeepvat [1], Antonis A. Armoundas [2,3], Richard Boyer [1]

1. Dept of Anesthesiology, Weill Cornell Medicine, New York, NY
2. Cardiovascular Research Center, Massachusetts General Hospital, Boston, MA,
3. Broad Institute, Massachusetts Institute of Technology, Cambridge, MA

Introduction

- Perioperative myocardial infarction after non-cardiac surgery is increasing with our aging population and increases mortality risk by approximately 10-fold.
- Intraoperative monitoring of myocardial ischemia via computerized ST-segment analysis is limited by lead selection and placement, filter selection, gain adjustment, noise, and interpretability.
- This study aims to develop a machine learning (ML) model to detect intraoperative ischemia using electrocardiogram (ECG) features from a single lead.

Methods

- The study utilized the VitalDB database, a comprehensive repository of intraoperative data of 6,388 patients, including ECG-II, invasive arterial BP recordings, and other vital signs.
- Beat-by-beat ECG fiducial features (PQRST waveform profiles) were extracted and mean arterial pressure (MAP) was derived from invasive BP systolic and diastolic values.

ECG Features Assessed – Beat by Beat

Wave Features (P, Q, R, S, and T):
- Amplitude and Delta-Amplitude from Baseline
- Duration and Delta-Duration from Baseline

ST Features:
- ST Amplitude and Delta-Amplitude from Baseline
- ST Duration and Delta-ST Duration from Baseline
- ST Area and Delta-ST Area from Baseline
- ST Slope and Delta-ST Slop from Baseline

Other Features:
- QT Duration and Delta-QT Duration from Baseline
- J-Amplitude and Delta-J Amplitude from Baseline

Annotation Criteria for Ischemia

- **Key assumption: Ischemia present during persistent hypotension with ST change > 0.1 mV in lead II.**
- Hypotension: MAP < 65 mmHg for at least 2 minutes
- Normotension: MAP > 75 mmHg for at least 2 minutes
- ST change (+) : Delta ST >= 0.1 mV (each beat)
- ST change (-) : Delta ST < 0.1 mV (each beat)
- 4 Classes: ST(+)/Hypo, ST(+)/Normo, ST(-)/Hypo, ST(-)/Normo

- Data partition: Training dataset (80%) and testing dataset (20%).
- Machine-learning algorithms: Random forest classifier, Gradient boosting classifier.

Hypothesis

We hypothesize that machine learning algorithms can detect changes in ECG during ischemic episodes associated with prolonged hypotension.

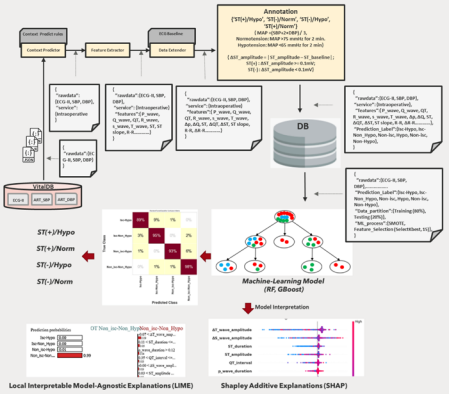

Figure 1: Overview of methodology for classifying the intraoperative ischemia events using ML.

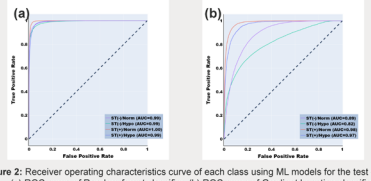

Figure 2: Receiver operating characteristics curve of each class using ML models for the test dataset. (a) ROC curve of Random forest classifier, (b) ROC curve of Gradient boosting classifier.

Results

- The accuracy of the 4-class model was 96% and 79% using Random forest and Gradient boosting classifier, respectively.
- SHAP plots shows the contributions of ECG fiducial features in classifying ischemic events in ML models with T-wave delta, S-wave delta, and wave durations having the greatest importance.

ML Model	Accuracy	Precision	Recall	F1-score
Random forest	0.96	0.96	0.96	0.96
Gradient boosting	0.79	0.84	0.79	0.81

Figure 3: Classification Performance matrix of ML models.

Figure 4: Confusion Matrices of ML models for test dataset (a) Random forest classifier, (b) Gradient boosting classifier.

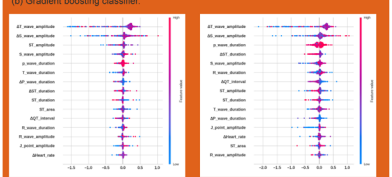

Figure 5: Interpretation of ML models for classifying the Intraoperative Ischemia events using SHAP based on ECG features. (a) SHAP analysis of Random forest classifier, (b) SHAP analysis of Gradient boosting classifier.

Conclusions

- These results demonstrate the potential utility of ML-based identification of ECG features in accurately identifying ischemic episodes during prolonged hypotension.

Neurophysiological correlates of delayed recovery of consciousness in a critically-ill COVID-19 patient with repeated cardiac arrest

Weill Cornell Medicine

Seyed A. Safavynia, MD, PhD, Jessica Wang, BA, Jacky M. Choi, MPH, Natalia Roszkowska, BS, Joseph Chiaro, DO, Padmaja Kandula, MD, Sophia Hu, Jonathan D. Victor, MD, PhD, Nicholas D. Schiff, MD

NewYork-Presbyterian

[1]Department of Anesthesiology, Weill Cornell Medical College [2]Division of Biostatistics, Department of Population Health Sciences, Weill Cornell Medical College [3]School of Medicine, Weill Cornell Medical College
[4]Department of Neurology, University of Washington [5]Department of Neurology, Weill Cornell Medical College [6]University of California, Los Angeles [7]Feil Family Brain and Mind Research Institute, Weill Cornell Medical Center

Introduction

We have recently shown in a cohort of over 1200 patients that delayed recovery of consciousness (RoC) following mechanical ventilation and sedation in patients with critically-ill COVID-19 infection is common, often occurring without evidence of structural neurologic injury[1]. Further, the delayed RoC is significantly associated with hypoxemia in a graded fashion independent of demographics, disease severity, and sedation exposure[1]. Similarly, patients with prolonged in-field anoxia associated with cardiac arrests and post-arrest coma can have delayed RoC long after withdrawal of sedative agents, suggesting a potential common underlying mechanism between these conditions.

At a neuronal level, the late recovering post-arrest patients uniformly exhibited burst suppression (BSP) on electroencephalography (EEG), with RoC occurring long after EEG activity slowly restored. Moreover, an increasing intra-burst peak frequency within the theta range (~4-7 Hz) during BSP was associated with recovery[2]. However, no prior evidence links similar neurophysiological changes to brief hypoxic insults as seen in our COVID-19 cohort, nor how they may correlate with the time course of neuronal and behavioral recovery in this population.

We present a patient with both critically-ill COVID and short cardiac arrests occuring in a monitored setting while oxygenated on mechanical ventilation with 26 days of EEG monitoring, providing a unique window on the possible connection across these phenomena. We examine the detailed evolution of his hospital course, including increased metaoblic stress from severe COVID-19 infection, bouts of intermittently severe hypoxemia ($PaO_2 \leq 55$ mmHg) and two cardiac arrests (with recovery of spontaneous circulation (ROSC) at 2 and 6 min), all in the setting of prolonged GABA-mediated sedation.

Methodology

This study was approved by the Institutional Review Board (IRB 20-08022490) using data from the Weill Cornell Registry of SARS-COV 2 Patients (IRB 20-03021689), Weill Cornell COVID-19 Observational Research Cohort (IRB 20-03021681), and Weill Cornell Registry and Biobank of Critically Ill Patients (IRB 1405011116).

Patient's clinical course was reviewed using daily progress notes of primary and consult medical teams. Other clinical variables of interest included: PaO_2 values, sedation records, Glasgow Coma Scale (GCS) component scores, CT/MRI neuroimaging, and EEG data.

Sedation exposure. Bolus and infusion administration doses were extracted hourly. Sedative exposure was estimated by applying a half-life function to each hourly dose and applying a recency-weighted sum of weight-adjusted doses at each time point[3]. Half-lives used: midazolam 150 minutes, propofol 40 minutes, dexmedetomidine 120 minutes, ketamine 150 minutes, fentanyl 360 minutes, rocuronium 80 minutes. Exposures were averaged daily and normalized to maximum sedative dose for visualization.

EEG composite scoring. Continuous EEGs were reviewed and scored on a qualitative scale (0-11; higher scores being more normal) encompassing: continuity (2 points), best rhythm (2 points), reactivity/variability (1 point), state changes (1 point), symmetry/focality (3 points), and seizure/discharges (2 points).

EEG spectral analysis. Raw 10-20 continuous EEG data were recorded at 256 Hz. Data were downsampled to 128 Hz, band-pass filtered from 0.7-70 Hz with a notch filter at 60 Hz, and a Hjorth Laplacian was applied to each channel. For each day, 2-3 hour long EEG segments containing burst suppression or burst attenuation were exported. Burst activity was parsed into ≥ 50 3-second windows and concatenated for spectral analysis using the multi-taper method (Chronux, mtspectrumc.m) in MATLAB. Peak theta frequency was estimated using the FOOOF algorithm[4]; band power was calculated using the cumulative trapezoid method.

Results

Hospital course reflects several metabolic insults and delayed recovery of consciousness without evidence of structural neurologic injury

Presentation: A 68 year-old man with history of hypertension, diabetes, atrial fibrillation, **chronic anemia** (baseline Hb 8) and **COVID-19 infection** (~1 week before admission) **admitted for acute hypoxemic respiratory failure** (SpO_2 83% on room air) and atrial fibrillation with rapid ventricular response in March 2020. Patient noted to have a tracheostomy in 2010 following an elective cholecystectomy.

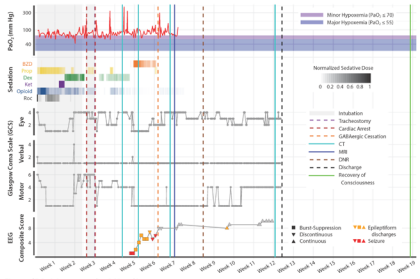

Figure 1. Clinical time course of variables of interest.

- Patient intermittently following commands until second cardiac arrest, then not again for remainder of hospital course (44 days following cessation of sedative agents)
- CT and MRI head imaging repeatedly negative for any structural neurologic injury
- Patient became comatose (GCS 3) shortly after initiating midazolam sedation
- EEG records show an abrupt shift from organized (alpha/beta) background activity into BSP, with gradual restoration of background activity prior to discharge
- Per medical records at a subsequent admission 49 days later, patient was noted to have returned to near his cognitive baseline, recognizing himself and having discussions with his family over video chat for hours

Intra-burst spectral EEG content comports with a favorable neurologic outcome, consistent with cardiac arrest data

Figure 2. Evolution of spectral content for intra-burst EEG over seven days corresponding to a behaviorally comatose (GCS 3) state. EEG segments are taken from gray shaded regions.

Figure 2A: Power spectral density (PSD) estimates for channel Pz. Pink shaded rectangle denotes theta band, and blue shaded rectangle denotes alpha band.

Figure 2B: peak theta frequency by brain region. Note day one is dominated by alpha, not theta activity. Blue trace, frontal channels; light green trace, centroparietal channels; dark green trace, temporo-occipital channels.

Figure 2C: normalized weighted sedation exposure (WSE) for midazolam.

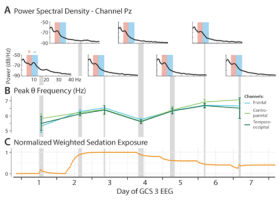

- Initial EEG reveals intra-burst alpha/beta organization in the presence of low-level midazolam administration
- EEG shifts to a theta-dominant rhythm with increasing midazolam exposure
  - Dominant theta frequency increases over course of BSP activity, consistent with patients with favorable outcomes following post-cardiac arrest coma
  - Theta frequency lowered following prolonged high midazolam exposure and recovering with lowering of sedation

Conclusion/Future Directions

Taken together, our case presents evidence for the hypothesis that hypoxia/anoxia and marked increase in GABAergic tone can trigger a global suppression of brain activity and late recovery of neurological function. Moreover, spectral analysis of burst suppression periods reveal a consistent signature linked to favorable outcomes after prolonged coma and recovery of neurological function multiple weeks after sedation cessation. Our results thus bridge the prior findings in out-of-hospital cardiac arrest coma to a broader range of metabolic insults. As has been further postulated[5], delayed RoC in COVID may reflect an unmasking of neural protective strategies in the setting of hypoxemic injury that is conserved across species; our findings of BSP show consistency with EEG data from anoxia-tolerant vertebrates. Further studies are needed to more rigorously model the relative contributions and interactions of each insult (e.g., hypoxemia, anoxia, sedation) at both patient and population levels.

Acknowledgements

SAS is awarded a JumpStart Career Development Grant from Weill Cornell Medical College. The authors thank Elizabeth Leon for assistance in obtaining continuous EEG data.

References

[1]Hoshijo CF, Safavynia SA*, Ibarra ME*, et al. Prolonged unconsciousness is common in COVID-19 and associated with hypoxemia. Ann Neurol. 2022;91(6):740-755.
[2]Forgacs PB, Devinsky O, Schiff ND. Independent functional outcomes after prolonged coma following cardiac arrest: A mechanistic hypothesis. Ann Neurol. 2020;87(4):618-632.
[3]Ibarra ME*, Safavynia, SA*, Der Nigoghossian CY, et al. Delayed recovery of consciousness after anesthetic coma in survivors of COVID-19 hypoxemic respiratory failure. In review.
[4]Donoghue T, Haller M, Peterson EJ, et al. Parameterizing neural power spectra into periodic and aperiodic components. Nat Neurosci. 2020;23:1655–1665.
[5]Schiff ND, Brown EN. Protective down-regulated states in the human brain: A possible lesson from COVID-19. Proc Natl Acad Sci USA. 2022;119(40):e2202211119.

Variation in Internal and External Respiratory Motions among Healthy Volunteers

Weill Cornell Medicine
NewYork-Presbyterian

Andrew Milewski, MD PhD[1] and Guang Li, PhD[2]

[1]Department of Anesthesiology, Weill Cornell Medicine, New York-Presbyterian Hospital, New York, NY
[2]Department of Medical Physics, Memorial Sloan Kettering Cancer Center, New York, NY

the ANESTHESIOLOGY annual meeting American Society of Anesthesiologists®

Background

Automated classification of respiratory waveforms may permit early identification of pathological states or enable sorting patients into categories of distinct respiratory mechanics. Schemes for classifying capnogram waveforms and distinguishing between normal and abnormal states have been advanced previously [1-3]. Obtaining an accurate capnogram often requires intubation or wearing an uncomfortable device on the face. A variety of non-invasive tools for monitoring patients' breathing have recently been developed, including stretch sensors worn over the chest or abdomen [4]. Here we undertake an analysis of the variation in respiratory motion among healthy volunteers measured by a stretch sensor and compared to a measure of internal respiratory motion.

Methods

Ten healthy volunteers participated in this IRB-approved study. During 4DMRI scans, a bellows placed on the subjects' upper abdomen measured external respiratory motion while an MR navigator interrogated the position of the left diaphragm's dome to concurrently acquire the internal-motion waveforms. Approximately ten minutes of data were obtained for each subject.

An automated algorithm segmented each waveform into its individual cycles. After folding all cycles for a waveform onto a single period, an average cycle was calculated, thereby generating an archetype cycle for each subject. The correlation between a volunteer's individual navigator cycles and the archetype waveform were calculated using Spearman's correlation coefficient, and the same was done for the individual navigator cycles and the archetype navigator waveform. The resulting distributions of navigator and bellows correlations were then compared using Student's t-test (*a priori* statistical significance set at $p < 0.05$).

The archetype bellows cycles were also compared to each other by calculating the maximum cross-correlation between each pair of archetypical cycles, and the same was done for the archetype navigator cycles. Specifically, the archetype waveforms were circularized and one waveform was phase-shifted with respect to another waveform until the correlation reached a maximum value. The difference between the maximum cross-correlations revealed whether the navigator or bellows archetype waveforms were more similar for each pair of volunteers.

Figure 1: Example Waveforms

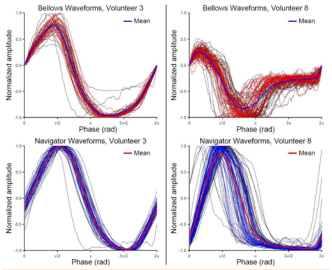

Example bellows (top) and navigator (bottom) waveforms for two volunteers after segmenting into individual cycles and rescaling the period and amplitude. Averaging the individual cycles yields the archetype waveform. Greater variation is seen for volunteer 8 (right) than for 3 (left).

Figure 2: Archetype Waveforms

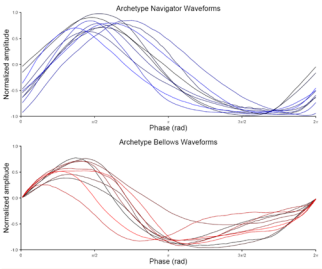

Archetype navigator (top) and archetype bellows (bottom) waveforms for all ten volunteers. Qualitatively, the shapes of the waveforms are similar. There appears, however, to be greater variation in the shapes of the archetype bellows waveforms.

Figure 3: Correlation between Individual and Archetype Waveforms

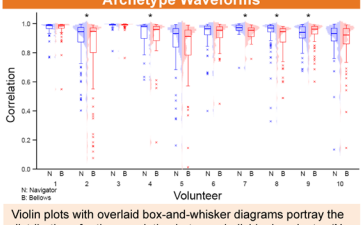

Violin plots with overlaid box-and-whisker diagrams portray the distributions for the correlation between individual navigator (N, blue) or bellows (B, red) waveform cycles and a volunteer's archetype navigator or bellows waveform. An asterisk indicates a statistically significant difference between means of the navigator and bellows correlation distributions ($p < 0.05$, Student's t-test). For volunteers 2, 4, 7, and 8, the correlation was greater between individual navigator cycles and the archetype waveform.

Figure 4: Difference between Bellows and Navigator Archetype Max Cross-Correlations

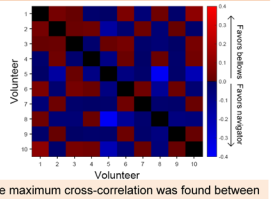

The maximum cross-correlation was found between each pair of volunteers' archetype navigator waveforms and the same for the archetype bellows waveforms. A matrix portrays the difference between those maximum cross-correlations: red squares indicate the maximum cross-correlation was higher among the archetype bellows pairs; blue indicates it was higher for the archetype navigator pairs.

Results

The respiratory waveforms for two volunteers (1 and 3) were highly regular and more variable for the others (Figures 1 and 3). In comparing the variation among navigator and bellows waveforms, there was no statistically significant difference for 5 volunteers, the bellows waveforms were more variable for 4 volunteers, and the navigator waveforms were more variable for one volunteer (Figure 3). Consequently, it was more common to observe a higher degree of variability in the shapes of the individual bellows cycles than in the shapes of the individual navigator cycles.

The maximum cross-correlations were calculated between every pair of archetype bellows waveforms and every pair of archetype navigator waveforms. The maximum cross-correlation between pairs of navigator waveforms was more often greater than that between pairs of archetype bellows waveforms (26 out of 45 pairs compared to 19 out of 45), indicating greater variation in the bellows waveforms between volunteers (Figure 4).

Conclusions

A relative degree of similarity was found for the average respiratory cycles among the ten healthy volunteers in this study. Nevertheless, some differences were seen between the navigator and bellows archetypes, namely there was slightly greater variation among the bellows archetypes compared to the navigator archetypes, the latter of which provide ground truth. In using non-invasive devices to measure respiratory motion, care must be taken to understand the variation that is added by the measuring apparatus.

References

1. Herry CL, Townsend D, Green GC, Bravi A, Seely AJ. Segmentation and classification of capnograms: application in respiratory variability analysis. Physiol Meas. 2014 Dec;35(12):2343-58. doi: 10.1088/0967-3334/35/12/2343. Epub 2014 Nov 12. PMID: 25389703.
2. Mieloszyk RJ, Verghese GC, Deitch K, Cooney B, Khalid A, Mirre-Gonzalez MA, Heldt T, Krauss BS. Automated quantitative analysis of capnogram shape for COPD-normal and COPD-CHF classification. IEEE Trans Biomed Eng. 2014 Dec;61(12):2882-90. doi: 10.1109/TBME.2014.2332954. Epub 2014 Jun 24. PMID: 24967981.
3. Jaffe MB. Using the features of the time and volumetric capnogram for classification and prediction. J Clin Monit Comput. 2017 Feb;31(1):19-41. doi: 10.1007/s10877-016-9830-z. Epub 2016 Jan 18. PMID: 26780902.
4. Monaco V, Stefanini C. Assessing the Tidal Volume through Wearables: A Scoping Review. Sensors (Basel). 2021 Jun 16;21(12):4124. doi: 10.3390/s21124124. PMID: 34208468; PMCID: PMC8233785.

United States rural residence is associated with increased acute maternal end-organ injury or mortality after birth: a retrospective multi-state analysis, 2007–2018

Primary Investigator: Robert White, MD, MS.

Department of Anesthesiology 15th Research Exposition | October 31, 2023

Weill Cornell Medicine
NewYork-Presbyterian

Investigators:

(project-specific PIs are represented in bold)

Rahul Chaturvedi, MD. Briana Lui, BS. Virginia Tangel, MA, MSc. Sharon E. Abramovitz, MD. Kane O. Pryor, MD. Grace Lim, MD, MS. **Robert S. White, MD, MS.**

Background

Geographic-based healthcare determinants and choice of anesthesia have been shown to be associated with maternal morbidity and mortality. In a 2012–2017 analysis of the National Inpatient Sample (NIS), a database created for the Healthcare Cost and Utilization Project (HCUP) that contains national estimates of inpatient access, cost, outcomes and quality measurements from approximately 7 million hospital visits annually in the USA, women in the most urban (such as central large metropolitan areas) and the most rural counties (non-metropolitan or micropolitan areas) experienced higher odds of combined SMM and mortality compared with women from smaller cities (such as small metropolitan and micropolitan areas). Anesthetic choice also impacts maternal morbidity and mortality; a cross-sectional study found that neuraxial analgesia is associated with lower rates of SMM during vaginal births, possibly explained by increased access to anesthesiologists who have critical care training. We explored whether differences in maternal outcomes based on maternal residence, and anesthesia type for cesarean and vaginal birth, exist.

Proportion of Mothers by Residence

Full sample (FL, MD, KY, WA 2007-2018, NY 2007-2016, CA: 2007-2011): 9,561,813	
Central large metropolitan (%)	4,320,749 (45.2)
Fringe large metropolitan county (%)	2,445,444 (25.6)
Medium metropolitan county (%)	1,523,728 (15.9)
Small metropolitan county (%)	564,400 (4.9)
Micropolitan county (%)	422,520 (4.4)
Not metro or micro (%)	256,077 (2.7)
Missing (%)	28,895 (0.3)

NY only (anesthesia type analyses): 2,269,375	
Central large metropolitan (%)	1,302,620 (57.4)
Fringe large metropolitan county (%)	515,324 (22.7)
Medium metropolitan county (%)	229,669 (10.1)
Small metropolitan county (%)	70,805 (3.1)
Micropolitan county (%)	105,125 (4.6)
Not metro or micro (%)	37,943 (1.7)
Missing (%)	7,889 (0.4)

Project Summary

This study was a retrospective multi-state analysis; patient residence was the predictor variable of interest and a composite binary measure of maternal end-organ injury or inpatient mortality was the primary outcome. Our secondary outcomes included a binary measure of anesthesia type for cesarean birth (general vs. neuraxial [NA]) and NA analgesia for vaginal birth (no NA vs. NA). Our predictor variable of interest was patient residency (reference category central metropolitan areas of >1 million population), fringe large metropolitan county, medium metropolitan, small metropolitan, micropolitan, and non-metropolitan or micropolitan county.

Mortality or End-Organ Damage According to Residency (Urban–Rural Status)

County Type	Number with outcome (%)	Rate of mortality or end-organ damage per 10,000	Crude OR (95% CI)	Adjusted OR (95% CI)	SMD between central counties and each category
Central large metropolitan	24,716 (0.6)	57.2	(reference)	(reference)	(reference)
Fringe large metropolitan	13,085 (0.5)	53.5	1.06 (1.03 to 1.10)**	1.03 (1.00 to 1.07)	0.005
Medium metropolitan	6,620 (0.4)	43.4	1.20 (1.13 to 1.28)***	1.09 (1.03 to 1.16)**	0.019
Small metropolitan	2,061 (0.4)	36.5	1.27 (1.17 to 1.38)***	1.13 (1.04 to 1.22)**	0.030
Micropolitan	1,737 (0.4)	41.1	1.36 (1.26 to 1.47)***	1.17 (1.09 to 1.27)***	0.023
Not metro or micro	1,032 (0.4)	40.3	1.29 (1.17 to 1.41)***	1.14 (1.04 to 1.24)**	0.024

OR: odds ratio. CI: confidence interval. SMD: standardized mean difference. Percent may not sum to 100 due to rounding and missing values. Geographic locality defined as, central counties with metro areas of > 1 million population [urban; reference], fringe counties of metro areas of > 1 million population [suburban], counties with metro areas of 250,000–999,999 population [medium county], counties with at least one metro area of 50,000–249,999 population [small county], counties with population cores of 10,000–49,999 population [micropolitan rural], and non-core counties, which contain no city or town of < 10,000 population [non-core rural]. *P < 0.05.**P < 0.01.***P < 0.001.

Results

Separate outcomes of a) general anesthesia for cesarean deliveries and b) no neuraxial analgesia for vaginal births, by categories of geographic locality

Outcome	No. (%)	Adjusted OR (95% CI)
General anesthesia for cesarean deliveries		
Central large metropolitan	34,159 (15.1)	1.00 (reference)
Fringe large metropolitan	6,901 (5.8)	**0.47 (0.46 to 0.49)*** **
Medium metropolitan	3,063 (4.9)	**0.56 (0.53 to 0.58)*** **
Small metropolitan	934 (6.1)	**0.68 (0.63 to 0.74)*** **
Micropolitan	2,056 (9.0)	1.06 (1.00 to 1.12)
Not metro or micro	589 (8.5)	1.00 (0.91 to 1.09)
No neuraxial analgesia for vaginal births		
Central large metropolitan	296,771 (55.7)	1.00 (reference)
Fringe large metropolitan	143,191 (58.8)	**1.84 (1.81 to 1.86)*** **
Medium metropolitan	56,932 (52.0)	**1.33 (1.31 to 1.36)*** **
Small metropolitan	22,089 (62.0)	**1.57 (1.53 to 1.61)*** **
Micropolitan	27,462 (65.3)	**2.07 (2.02 to 2.12)*** **
Not metro or micro	9,672 (66.7)	**2.25 (2.16 to 2.34)*** **

Multivariable logistic regression models were adjusted for variables representing primary insurance payer, race/ethnicity, income quartile by ZIP Code, birthing type, maternal age at birth, Bateman comorbidity index score, year of birth, hospital quartile of birthing volume, Black-serving delivery unit status, and hospital safety net burden. Table only depicts findings for discussed primary covariate of interest geographic locality. Percent may not sum to 100 due to rounding.

Women residing in micropolitan (OR 1.17; 95% CI 1.09 to 1.27) and non-metropolitan or micropolitan counties (OR 1.14; 95% CI 1.04 to 1.24) had the highest adjusted increased odds of adverse maternal outcomes. Those residing in suburban, medium, and small metropolitan areas underwent general anesthesia less often during cesarean births than those residing in urban areas. Patients residing in micropolitan rural (OR 2.07; 95% CI 2.02 to 2.12) and non-metropolitan or micropolitan (2.25; 95% CI 2.16 to 2.34) counties underwent vaginal births without NA analgesia more than twice as often as those residing in urban areas. Conclusions: Rural-urban disparities in maternal end-organ damage and mortality exist and anesthesia choice may play an important role in these disparate outcomes.

References

- Hoyert DL. Maternal mortality rates in the United States, 2020. Centers for Disease Control and Prevention (CDC). Centers for Disease Control and Prevention (CDC).
- King JC. Maternal mortality in the United States – why is it important and what are we doing about it? Semin Perinatol. 2012;36:14–18. https://doi.org/10.1053/j. Semper.2011.09.004.
- Wang E. Glazer KB. Howell EA. Janevic TM. Social Determinants of pregnancy related mortality and morbidity in the United States. Obstet Gynecol. 2020;135:896–915. https://doi.org/10.1097/AOG.0000000000003762.
- Williams AM. Chaturvedi R. Pollatis I. Ibarra-Colanni J. Aaronson JA. White RS. Associations between state policies, race, ethnicity and rurality, and maternal mortality and morbidity following the United States Supreme Court Dobbs v Jackson Women's Health Organization ruling. Br J Anaesth. 2022;129:e140–e147. https://doi.org/10.1016/j.bja.2022.08.016.
- Guglielminotti J. Landau R. Daw J. et al. Use of labor neuraxial analgesia for vaginal delivery and severe maternal morbidity. JAMA Netw Open. 2022;5: e220137.
- von Elm E. Altman DG. Egger M. et al. The Strengthening the Reporting of Observational Studies in Epidemiology (STROBE) statement: guidelines for reporting observational studies. J Clin Epidemiol. 2008;61:344–349.https://doi. Org/10.1016/j.jclinepi.2007.11.008.
- Kuklina EV. Whiteman MK. Hillis SD. et al. An enhanced method for identifying obstetric deliveries: implications for estimating maternal morbidity. Matern Child Health J. 2008;12:469–477.https://doi.org/10.1007/s10995-007-0256-6.
- Bateman BT. Mhyre JM. Hernandez-Diaz S. et al. Development of a comorbidity index for use in obstetric patients. Obstet Gynecol. 2013;122:957–965. https://doi. Org/10.1097/AOG.0b013e3182a603bb.

AAPM 2023
JULY 23–27 | HOUSTON, TX
65TH ANNUAL MEETING & EXHIBITION

Accurate prediction of respiratory motion using long, short-term—memory deep learning

ANDREW R. MILEWSKI[1], FAYED UDDIN[2], VYAS GUPTA[2], XINGYU NIE[3], and GUANG LI[2]
[1] Department of Anesthesiology, NewYork-Presbyterian Hospital/Weil Cornell Medicine
[2] Department of Medical Physics, Memorial Sloan-Kettering Cancer Center, New York, New York
[3] Department of Radiology, University of Kentucky, Lexington, KY

Memorial Sloan Kettering Cancer Center
Weill Cornell Medicine
NewYork-Presbyterian

INTRODUCTION

Although it has been proposed and attempted for treating patients, respiratory-gated radiotherapy (RGRT) has not been widely used in radiotherapy clinics: To date, real-time external indicators cannot provide accurate and reliable signals to turn radiation beams on and off within the desired gating windows. Owing to their inaccuracies, correlation-based, intra-fractional motion prediction models require frequent radiographic imaging to ensure the target is within the beam, precluding widespread application of these models for clinical purposes.

With the recent advances in deep learning (DL) and its applications in radiotherapy—including image segmentation and image modality conversion—many DL algorithms have been developed and tested, such as U-net-based convolution neural networks. The long short-term—memory (LSTM) algorithm has been thoroughly investigated in computer-vision research for automatic driving, including single-point forecasting in the immediate future and multi-point to multi-point learning and prediction [1-3].

AIM

To develop a deep learning (DL) model that accurately predicts internal-respiratory motion from an external surrogate using a long-short-term memory (LSTM) algorithm and to assess the model's stability over 30 minutes.

METHODS

An in-house MatLab program was developed with the LSTM-DL algorithm to build and test a prediction model. Five volunteer subjects participated in this IRB-approved 4DMRI study and concurrent external and internal motion waveforms were acquired during the 4DMRI scan using both a bellows on the upper abdomen and an MR navigator at the diaphragm's dome. Each of the subjects was scanned twice: every scan collected approximately 10 minutes of data, and 30 minutes elapsed before the same subject was scanned again.

For each subject, approximately 50% of only the first scan's data was used to train the model and the remaining data from both scans was used to test the accuracy of the predicted waveforms. Specifically, the agreement between the actual and predicted waves was evaluated by measuring the point-by-point correlation and by calculating the differences between the actual and predicted locations of the waveforms' peaks and troughs.

A range of training parameters were examined and, to account for stochasticity in the LSTM-DL algorithm, five replicates were performed for each set of training parameters. After averaging over the five replicates, the best set of training parameters were identified for each volunteer. The results for only the best training parameters are presented. The performance of the LSTM-DL algorithm was also compared to that of a previously developed model that corrects the phase shift between the bellows and navigator waveforms.

RESULTS

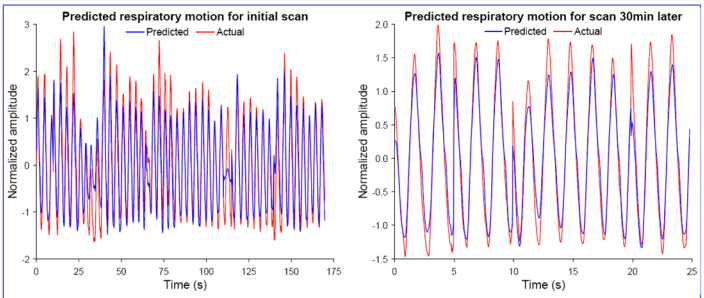

Figure 1. An example of the actual (red) diaphragm motion and the waveform predicted by the LSTM-DL algorithm (blue) for the scan containing the training data (left) and for a scan of the same subject 30 minutes later (right). Although errors exist between the actual and predicted heights of the waveform's peaks and troughs, the LSTM-DL algorithm accurately predicts the temporal locations of the peas and troughs.

	Scan 1	Correlations, Scan 1 ± S.D.			Avg. Error in Peak	Avg. Error in Troughs	Scan 2	Correlations, Scan 2 ± S.D.			Avg. Error in Peak	Avg. Error in Troughs
Subject	Length (s)	Ori	LSTM	PSC	Location ± S.D. (s)	Location ± S.D. (s)	Length (s)	Ori	LSTM	PSC	Location ± S.D. (s)	Location ± S.D. (s)
1	267.0	0.72 ± 0.10	0.92 ± 0.01	0.90 ± 0.05	0.05 ± 0.01	0.21 ± 0.05	42.5	0.79 ± 0.01	0.99 ± 0.00	0.96 ± 0.01	0.10 ± 0.03	0.13 ± 0.02
2	313.2	0.40 ± 0.11	0.97 ± 0.01	0.79 ± 0.12	0.10 ± 0.05	0.16 ± 0.01	50.0	0.59 ± 0.04	0.97 ± 0.01	0.93 ± 0.01	0.09 ± 0.02	0.13 ± 0.02
3	350.0	0.52 ± 0.27	0.84 ± 0.07	0.82 ± 0.14	0.18 ± 0.03	0.23 ± 0.06	266.6	0.59 ± 0.14	0.83 ± 0.08	0.87 ± 0.09	0.17 ± 0.12	0.24 ± 0.05
4	600.0	0.03 ± 0.10	0.97 ± 0.01	0.69 ± 0.10	0.18 ± 0.04	0.29 ± 0.02	325.7	0.10 ± 0.09	0.96 ± 0.02	0.70 ± 0.09	0.18 ± 0.06	0.20 ± 0.01
5	442.4	0.66 ± 0.13	0.81 ± 0.05	0.82 ± 0.13	0.21 ± 0.02	0.36 ± 0.08	39.2	0.47 ± 0.56	0.90 ± 0.05	0.64 ± 0.31	0.21 ± 0.17	0.78 ± 0.64
Mean	329.4	0.47 ± 0.27	0.90 ± 0.07	0.80 ± 0.08	0.14 ± 0.07	0.25 ± 0.08	144.8	0.51 ± 0.26	0.93 ± 007	0.82 ± 0.14	0.15 ± 0.05	0.30 ± 0.27

Table 1. Correlation enhancement achieved by the LSTM-DL model and error in locating waveforms' peaks and troughs. Ori: Correlation between the original bellows and navigator waveforms. LSTM: Correlation between the actual navigator waveform and the waveform predicted by the LSTM-DL algorithm (averaged over the five replicates for the best set of training parameters. Phase-shift corrected (PSC): Correlation between the navigator and bellows waveforms after correcting their waveforms. Scan 1 contained the data used for training the LSTM-DL model for each subject. The correlation between the actual waveform and the waveform predicted by the LSTM-DL algorithm almost always exceeded that achieved by the PSC method. Applying the trained model to the second scan generated predicted waveforms that correlated strongly with the actual waveforms as measured by point-by-point correlation and by comparing the locations of the actual and predicted peaks and troughs in the respiratory waveforms. For the average error in the peaks' and troughs' location, an average was first taken over all of the identified peaks or troughs, and a subsequent average was then taken over the five replicates for the best set of training parameters. Because the troughs of the waveforms are usually broader than the peaks, we expect larger errors in identifying the temporal locations of troughs. Indeed, for every volunteer the error in locating the waveform's troughs is greater than that for the waveform's peaks.

DISCUSSION

- Within the same 4DMRI scan and in a subsequent scan 30 minutes later, the LSTM-DL method accurately predicts the motion of the diaphragm for all five subjects (Figure 1).
- The predicted waveforms achieve point-by-point correlations of 0.83 or greater for all scans (Table 1), values that almost always exceed the enhanced correlation achieved by the phase-shift—correction model.
- For the scans containing the training data, the LSTM-DL algorithm accurately predicts the locations of peaks in the respiratory waveform to within 0.14 ± 0.07 seconds on average, and to within 0.15 ± 0.05 seconds on average for the subsequent scans performed 30 minutes later. Moreover, the average error in locating the waveform's peaks never exceeded 0.25 seconds.
- The LSTM-DL algorithm also predicted the locations of troughs in the respiratory waveform to within 0.25 ± 0.08 seconds on average in the first scan and to within 0.30 ± 0.27 seconds on average in the second scan. Owing to the shapes of the waveforms, locating the respiratory waveforms' troughs is expected to be less accurate than locating the peaks.

CONCLUSION

- The LSTM-DL method accurately predicts the motion of internal organs from external-motion data, and the model's accuracy is comparable or superior to that of a physical model.
- Before clinical applications in radiotherapy can be developed from LSTM-DL algorithms, further study with more data is required, especially with regard to the long-term stability of LSTM-DL models.

ACKNOWLEDGEMENTS

This study is in part supported by the NIH (U54CA137788). The authors thank participating volunteers and Philips Healthcare for technical support.

REFERENCES

[1] Lin H, Shi C, Wang B, Chan MF, Tang X, Ji W. Towards real-time respiratory motion prediction based on long short-term memory neural networks. Physics in medicine and biology. 2019;64(8):085010.

[2] Wang G, Li Z, Li G, et al. Real-time liver tracking algorithm based on LSTM and SVR networks for use in surface-guided radiation therapy. Radiat Oncol. 2021;16(1):13.

[3] Nie X, Li G. Real-Time 2D MR Cine From Beam Eye's View With Tumor-Volume Projection to Ensure Beam-to-Tumor Conformality for MR-Guided Radiotherapy of Lung Cancer. Frontiers in oncology. 2022;12:898771.

CONTACT INFORMATION

E-mail for corresponding author: lig2@mskcc.org (G. Li).

Larger Decrease From Baseline Transglomerular Pressure Gradient Associated With Acute Kidney Injury In Cardiac Surgical Population

Ryan Price MD, Sanya Rastogi BS, Christina Zecca MD, Klint Smart MD, Emily Eruysal MD, Avika Kasubhai BA, Sagar Navare MD, James Osorio MD, Christopher Lau MD, Ankur Srivastava MD

Department of Anesthesiology, Weill Cornell Medicine, NewYork-Presbyterian Hospital, New York, NY

Introduction

Acute kidney injury (AKI) after cardiac surgery is associated with increased mortality. Optimizing hemodynamics is imperative. The **transglomerular pressure gradient** relates the interplay of forward perfusion pressure and opposing back pressure. This gradient is represented by **mean perfusion pressure (MPP), defined as [mean arterial pressure (MAP) – central venous pressure (CVP)].**

A study of vasopressor-dependent cardiac surgical patients found those with AKI to have higher baseline MPP, and more notably a larger change from this baseline postoperatively.[1] This change was termed percent deficit. A possible limitation is its lack of invasive CVP measurements. Through standardized right heart catheterization (RHC), our study aims to most accurately determine perioperative transglomerular pressure gradient values to evaluate risk for AKI in a cardiac surgical population. **We hypothesize an increased percent deficit will be associated with increased risk for AKI.**

Study Design

This retrospective observational study evaluates patients who underwent elective cardiac surgery at a large academic center from 2018-2022. Chart review was performed using EPIC Electronic Medical Record (EMR). Patient demographics and preoperative hemoglobin, creatinine, and hemodynamic values through RHC were obtained. Intraoperative and postoperative hemodynamic values through RHC, and postoperative hemoglobin, creatinine, lactate, and urine output were obtained for comparison. **Percent deficit**, which can be defined as the **percent change from baseline pressure parameter**, was calculated as **[(Postoperative Pressure Parameter– Preoperative Pressure Parameter) / (Preoperative Pressure Parameter)].** Percent deficit was determined for MPP across postoperative days 0-4 (POD 0-4).

Study Design (cont.)

A case-control study was conducted by separating the patient sample according to the presence or absence of the primary endpoint, AKI, as defined by Kidney Disease: Improving Global Outcomes (KDIGO) score. Secondary endpoints included operative mortality and adverse outcomes after cardiac surgery. Patients excluded had a history of end stage renal disease, intraoperative deep hypothermic circulatory arrest, emergent surgery, endovascular surgery, or required post operative mechanical cardiovascular support. Statistical significance was calculated utilizing the Mann-Whitney U test for continuous variables and the Chi-Squared test for categorical variables. A p-value of less than 0.05 was considered statistically significant.

Table 1: Baseline Characteristics

	All Patients	AKI	No AKI	p-value
Number of Patients (% of total)	249	207 (83.13%)	42 (16.87%)	N/A
Age	64.18	63.23	69.10	*0.01*
Male (% of group)	171	139 (67.15%)	33 (78.57%)	0.14
Creatinine	1.01	0.98	1.14	*0.05*
Hemoglobin	12.68	12.72	12.49	0.06
PVD (% of group)	14	11 (5.31%)	3 (7.14%)	0.64
CPB Time	119.98	116.90	135.14	*0.05*
CABG + Valve (% of group)	40	29 (14.01%)	11 (26.19%)	*0.05*

Results

There were 42 instances of AKI across 249 patients (16.87%). Patients with AKI compared to those without, had a higher preoperative MPP (84.45 to 78.74). MPP percent deficit was consistently larger (more negative) for patients with AKI. Averaged across POD 0-4, **patients with AKI had an average MPP percent deficit of -24.99%, compared to -15.14% for those without.** Differences in MPP percent deficit between patients with and without AKI were **statistically significant for each individual postoperative day.**

Figure 1: MPP Deficit Across Postoperative Days 0-4

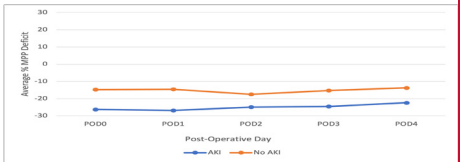

Discussion

In this retrospective case-control study utilizing invasive hemodynamic measurements throughout the perioperative period of cardiac surgery, there was a **consistently larger decrease in MPP from baseline for patients with AKI than for patients without.**

The concept of elevated back pressure playing a role in AKI development has been discussed in multiple settings.[2] An elevated MAP goal has been supported to reduce the risk of AKI in chronically hypertensive patients.[3] By highlighting the importance of achieving baseline transglomerular perfusion pressure to account for back pressure of the kidney, the synergism of these concepts is emphasized in our study.

Patients with a larger change, or percent deficit, in transglomerular pressure gradient from preoperative baseline were at a higher risk for AKI. **These preliminary results suggest that a higher transglomerular pressure would be an appropriate perioperative target for patients with a higher baseline to reduce risk for AKI.**

References

1. Saito S, Uchino S, Takinami M, Uezono S, Bellomo R. Postoperative blood pressure deficit and acute kidney injury progression in vasopressor-dependent cardiovascular surgery patients. *Crit Care*. 2016;20:74. doi:10.1186/s13054-016-1253-1
2. Chen CY, Zhou Y, Wang P, Qi ET, Gu WJ. Elevated central venous pressure is associated with increased mortality and acute kidney injury in critically ill patients: a meta-analysis. *Crit Care*. 2020;24:80. doi:10.1186/s13054-020-2770-5
3. Leone M, Asfar P, Radermacher P, Vincent JL, Martin C. Optimizing mean arterial pressure in septic shock: a critical reappraisal of the literature. *Crit Care*. 2015;19(1):101. doi:10.1186/s13054-015-0794-z

An artificial intelligence-powered, patient-centric digital tool for self-management of chronic pain: A prospective, multicenter clinical trial

Maria L Rosén Klement, PhD, Antje M Barreveld, MD, Sophia Cheung, Ulrika Axelsson, PhD, Jade I Basem, Anika S Reddy, Carl AK Borrebaeck, DSc, Neel Mehta, MD

Conclusion

- The Paindrainer™ digital device, powered by a neural network, improved daily function and or reduced pain interference in 72.5% of chronic back and neck pain patients over a 12-week period.
- Secondary outcomes, including anxiety, depression, and pain intensity, pain catastrophizing also improved significantly.
- The 360° patient-centric pain management tool could potentially revolutionize chronic pain care, offering effective individualized, accessible, and cost-effective solutions.

Introduction

Chronic pain, impacting quality of life for millions worldwide, poses a substantial public health problem with extensive societal and economic consequences. Access to effective treatments is limited, driving innovative solutions. Personalized, patient-centric approaches are crucial in addressing the multifaceted nature of chronic pain, where the newly developed Paindrainer™ tool offers an innovative solution to pain management. The present study explores the efficacy of an neural network-driven digital tool, Paindrainer™, grounded in acceptance and commitment therapy, designed to empower individuals in controlling and managing chronic pain.

Method

Paindrainer™ analyze the relationship between the individual user's daily activities and their experienced pain level. For a patient to take control of their pain, activities and pain levels are processed by the proprietary neural network. Since the human brain can only process around four parameters at a given time[1] and daily activities and combination thereof are many more, finding the right activity balance is difficult for patients. Inaccurate conclusions lead to problems, such as fear avoidance and catastrophizing or even hyperactivity. A digital device, using artificial intelligence can quantify and decipher the relationship of all daily activities and coach the patients to maximize their desired activities, guide in gradual behavior changes, without causing undesirable high pain levels.

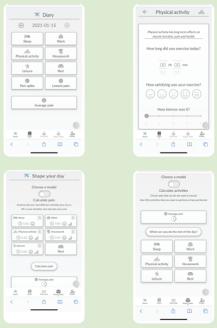

Figure 1: Layout of the Paindrainer Tool and its Functions, Including the Diary, Activity Logging, and the "Shape your day" planning feature. Users can calculate the optimal activity balance at a designated pain level or view the expected pain level after completing a predefined set of activities.

- **Study Design:** Prospective, multicenter, single-arm, open-label study.
- **Participants:** Chronic back and neck pain patients (n=43) at Newton-Wellesley Hospital and New York-Presbyterian/Weill Cornell Medical Center.
- **Inclusion Criteria**: Age > 18, > 3 months of low back or neck pain.
- **Intervention:** 12 weeks regular use of the digital platform Paindrainer™
- **Outcome Measurments:**
  - Primary outcome - Pain interference measured by PROMIS 6a
  - Secondary outcomes - Physical function 10a, anxiety 4a, depression 4a, pain intensity, pain catastrophizing, and Chronic Pain Acceptance questionnaire.

Results

Primary Outcome: Significant decrease in pain interference at 6 weeks (p<0.0001) and 12 weeks (p=0.020). About 60% of subjects achieved meaningful improvement in Pain Interference, above MID of 2.4.

Secondary Outcomes: Significant improvement in physical function (p=0.0008), anxiety (p=0.0001), and pain intensity (p<0.05). Improvements exceeded minimal important differences.

A decrease in T-score for PROMIS depression 4a above MID was observed in all subjects (p=0.003) with a baseline score above 55.

Work Capacity: Around 50% of subjects increased daily work capacity by over an hour, and up to 4 hours.

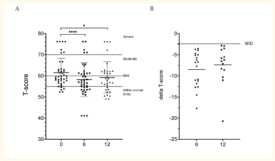

Figure 2. A; Clinical significant change in PROMIS Pain Interference 6a from pre-treatment to week 6 and 12. B; Reduction in T-score for responding patients (MID < 2.4), mean change in delta T-score 8.5 (6w) and 7.4 (12w). ***p <0.0001, *0.016

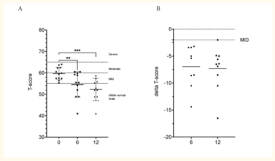

Figure 3. A; Clinical significant change in PROMIS Depression 4a from pre-treatment to week 6 and 12 in patient with a T-score above 55 at start of study. Reduction in T-score for responding patients (MID < -3.0) mean change -6.9 (6w) and -8.4 (12w) . *** p=0.0010, **p= 0.003

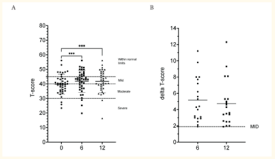

Figure 4. A; Clinical significant change in PROMIS Physical function 10a from pre-treatment to week 6 and 12. B: Increase in Delta T-score for responding patients (MID >1.9) mean average change over MID, 5.2 (6w) and 4.7 (12w)
*** p = 0.0008, *** p=0.0008.

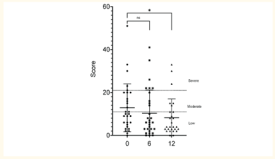

Figure 5. Significant change in Pain Catastrophizing from baseline to week 12, mean score at baseline 12.9 to 8.2 * p=0.024

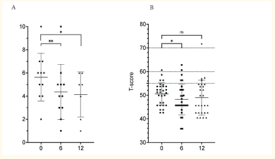

Figure 6. A; NRS pain score at pre-treatment and 6, 12w, decrease in mean score from 5.6 to 4.4 at 6 weeks and to 4.1 at 12 weeks. *p=0.03; **p=0001.
B; T-score at pre-treatment and 6, 12w , using PROMIS questionnaire Pain intensity 3a. With a recorded decrease in mean score from 50.5 to 48.0 at 6 weeks (n=30) and to 49.0 at 12 weeks (n=27) *p = 0.022

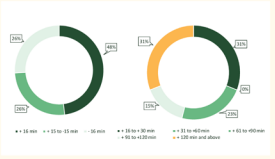

Figure 7. Change in capacity to work, average increase in minutes per day per week

1) Halford GS et al (2005) Psychol Sci

Mass General Brigham
Newton-Wellesley Hospital

Weill Cornell Medicine
Anesthesiology

Tufts University
School of Medicine

Lunds Universitet

Paindrainer

Nordic Health App Award 2023

FDA Registered Medical Device Class 1

CE

Improving Response to Routine and Difficult Airways at Weill Cornell Medicine/NewYork-Presbyterian Hospital

Ingharan Siddarthan, M.D., Emily Rose Eruysal, M.D., Rahul Chaturvedi, M.D., Amal Mansur Javaid, M.D., Michelle Tiangco, M.S., Deirdre C. Kelleher, M.D.

Department of Anesthesiology, Weill Cornell Medicine, NewYork-Presbyterian Hospital, New York, NY

Introduction

When a patient suffers cardiac arrest, shorter times to securing an airway are associated with better neurological outcomes.[1] Emergency airway management may be difficult, with 9-12% identified as challenging, and with complication rates up to 28%.[2]

After discontinuing pagers, our institution no longer had an efficient and systematic approach to airway consultation.

Objectives

- Identify perceived barriers to rapid and safe non-operating room airway interventions
- Improve communication between primary team and consulting anesthesiologist
- Identify potential difficult airways prior to evaluating the patient, to recruit necessary personnel and equipment

Investigation Methods

Survey Conducted - perceived barriers to urgent airway care and indications for advanced airway equipment/ personnel

Initial results - need for non-emergent airway consult, and opportunity to identify potential difficult airway prior to arrival

Initial intervention - development of airway consult order in EMR for non-emergent airway evaluation

Figure 1: Fishbone Diagram

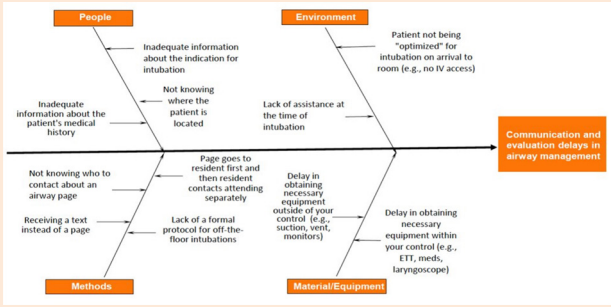

Figure 2: Airway Consult Order in EMR

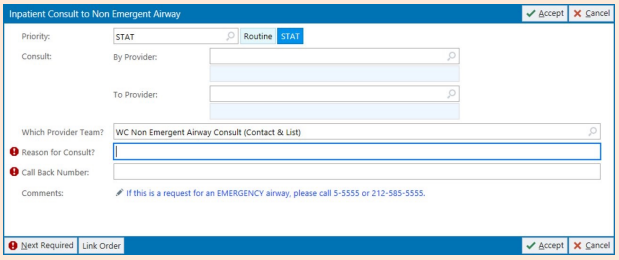

Discussion

- Prior to airway consult order, airway consultation was initiated via single page or EMR text chat without important patient info.
- **Initial identified needs**:
  - **Anesthesiology** – identification of urgency of airway and necessary information/equipment prior to arriving at the bedside; direct and immediate access to the patient chart
  - **Primary teams/unit staff** - means to contact anesthesiology reliably & efficiently depending on urgency of airway needs
- **Proposed solution**:
  - Maintain the emergency airway ("STAT INTUBATION") system to contact airway team during true emergency
  - Create airway consult order for urgent airway consultation and evaluation, facilitating rapid notification of multiple providers and providing immediate chart access. It also provides method of direct communication with primary team
- **Future directions**:
  - **Apply PDSA** method: assess frequency of STAT vs consult order and patient outcomes, refine intervention as indicated
  - **Create "Difficult Airway Response Team"** to address need for systematic response to more difficult airways

References

1. Steffen R, Hischier S, Roten FM, Huber M, Knapp J. Airway management during ongoing chest compressions-direct vs. video laryngoscopy. A randomised manikin study. PLoS One. 2023 Feb 9;18(2):e0281186. doi: 10.1371/journal.pone.0281186. PMID: 36757942; PMCID: PMC9910718.
2. Mark LJ, Herzer KR, Cover R, Pandian V, Bhatti NI, Berkow LC, Haut ER, Hillel AT, Miller CR, Feller-Kopman DJ, Schiavi AJ, Xie YJ, Lim C, Holzmueller C, Ahmad M, Thomas P, Flint PW, Mirski MA. Difficult airway response team: a novel quality improvement program for managing hospital-wide airway emergencies. Anesth Analg. 2015 Jul;121(1):127-139.

Abbreviations: EMR – electronic medical record.

Multilevel Social Determinants of Health Disparities in Postpartum Readmissions In the United States: A Multistate Analysis 2015-2020

Briana Lui, BS[1], Elizabeth Khusid, BA[1], Virginia E. Tangel, MA, MSc[2], Silis Y. Jiang, PhD[2], Sharon E. Abramovitz, MD[2], Corrina M. Oxford, MD[3], Robert S. White, MD, MS[2]

Background

- The reduction of preventable hospital readmissions to improve the quality of healthcare and reduce costs has been a national priority in recent decades.
- In the United States, the leading cause of hospital admission is related to pregnancy and delivery, accounting for nearly 4 million hospitalizations and costing $16.1 billion annually.
- Currently, there does not exist a standardized metric for calculating risk-adjusted readmission rates following childbirth.
- Studies examining disparities in postpartum readmission by patient- and hospital-level social risk factors are limited and/or dated.
- The aim of our study was to identify patient and hospital-level disparities in 30-day all-cause readmission following delivery hospitalization.

Methods

- Data source: State Inpatient Databases, Healthcare Cost and Utilization Project, Agency for Health Research and Quality from the states of Florida (2015-2019), Maryland (2015-2020), New York (2015-2017), and Washington (2015-2020)
- Patient-level variables of interest: race and ethnicity, primary insurance status, median household income by ZIP code, and rural-urban status
- Hospital-level variables of interest: Black-serving delivery unit, hospital safety-net burden
- Outcome of interest: 30-day readmission rate
- Generalized linear mixed models were used to estimate the effects of individual patient- and hospital-level social risk factors on odds of 30-day readmission after controlling a priori for patient-, hospital-, and procedure-level confounding variables.
- Statistical significance was evaluated at an adjusted alpha value of 0.0019 (0.05/27) after applying the Bonferroni correction.
- Secondary analysis stratified by mode of delivery and anesthesia type (NYS only).

Acknowledgements

Thank you to my research mentor, Dr. Robert S. White, the Center for Perioperative Outcomes, and the entire research team for their invaluable guidance and support with this project. Thank you to the Weill Cornell Medicine Areas of Concentration Program and Office of Medical Student Research for funding medical student research endeavors like this one.

Table 1. Adjusted odds ratios for 30-day postpartum readmissions by patient- and hospital-level social risk factors

	n (%)	aOR	95% CI	P-value
Race and ethnicity				
White	14463 (41.1)	Reference		
Black	10441 (29.6)	1.57	1.52-1.61	**<.0001**
Hispanic	6356 (18)	1.04	1.00-1.07	0.038
Other	3424 (9.7)	0.97	0.93-1.01	0.095
Missing	533 (1.5)	0.85	0.78-0.93	**<.0001**
Primary insurance payer				
Private insurance	15909 (45.2)	Reference		
Medicare	594 (1.7)	2.13	1.95-2.32	**<.0001**
Medicaid	17378 (49.3)	1.14	1.11-1.17	**<.0001**
Other	863 (2.5)	1.14	1.06-1.22	**<.0001**
Self-pay / No charge	472 (1.3)	1.06	0.97-1.16	0.220
Missing	<11 (0)	0.54	0.08-3.90	0.544
Median household income				
First quartile (poorest)	11376 (32.3)	Reference		
Second quartile	8922 (25.3)	0.94	0.92-0.97	**<.0001**
Third quartile	8157 (23.2)	0.94	0.91-0.97	**<.0001**
Fourth quartile (richest)	6497 (18.4)	0.86	0.83-0.89	**<.0001**
Missing	265 (0.8)	0.99	0.87-1.14	0.931
Rural-urban status				
Urban	14,025 (39.9)	Reference		
Suburban	11,750 (33.4)	1.07	1.04-1.12	**<0.0001**
Medium city	6,315 (18)	1.06	1.00-1.13	0.035
Small city	1,666 (4.7)	1.04	0.95-1.13	0.403
Micropolitan rural	995 (2.8)	1.03	0.94-1.12	0.539
Noncore rural	422 (1.2)	0.88	0.79-0.99	0.034
Missing	44	1.34	0.96-1.87	0.081
Black-serving delivery unit				
Bottom 75%	23957 (68)	Reference		
>5% to <= 25%	10254 (29.1)	1.09	1.00-1.19	0.047
Top 5%	1006 (2.9)	1.14	0.93-1.40	0.196
Safety-net burden				
Low burden	3411 (9.7)	Reference		
Medium burden	14055 (39.9)	1.01	0.90-1.14	0.824
High burden	17751 (50.4)	1.05	0.93-1.19	0.423

Results

- Our study cohort consisted of a total of 2,073,489 delivery hospitalizations, of which 35,217 (1.7%) patients were readmitted within 30 days post-delivery.
- Patient-level results showed that after adjusting for confounders, Black mothers had a 1.6 times greater adjusted odds of 30-day readmission than White mothers (aOR 1.57, 95% CI 1.52-1.61).
- Mothers with public insurance vs private insurance were more likely to be readmitted: Medicare: aOR 2.13 (95% CI 1.95-2.32), Medicaid: aOR 1.14 (95% CI 1.11-1.17).
- Compared to mothers in the poorest median income quartile, those in the richest quartile experienced a 14% reduction in adjusted odds of 30-day readmission (aOR 0.86, 95% CI 0.83-0.89).
- No significant associations were observed between mothers from rural areas compared to urban areas.
- Hospital-level results showed no significant associations between 30-day readmission and black-serving delivery unit and hospital safety-net burden.
- Stratified analyses showed that Black mothers were more likely than White mothers to be readmitted within 30 days of delivery regardless of delivery type, regardless of whether they received epidural vs no analgesia for vaginal births, and if they received regional anesthesia for cesarean births.

Discussion

- Our study demonstrated substantial disparities in 30-day postpartum readmission by patient-level factors, including race and ethnicity, insurance status, and household income.
- Stratified analyses suggested that Black race was the strongest predictor of 30-day readmission following delivery.
- Potential policies designed to incentivize lower maternal readmissions may disproportionately penalize hospitals that serve vulnerable populations.

References

1. Combs CA, Goffman D, Pettker CM: Society for Maternal-Fetal Medicine Special Statement: A critique of postpartum readmission rate as a quality metric. Am J Obstet Gynecol 2022; 226: B2-b9
2. Baker MC, Alberti PM, Tsao TY, Fluegge K, Howland RE, Haberman M: Social Determinants Matter For Hospital Readmission Policy: Insights From New York City. Health Aff (Millwood) 2021; 40: 645-654
3. Matthews KC, Tangel VE, Abramovitz SE, Riley LE, White RS: Disparities in Obstetric Readmissions: A Multistate Analysis, 2007–2014. American journal of perinatology 2022; 39: 125-133

Carotid Doppler Imaging Correlation with Pulmonary Artery Catheters As A Marker For Fluid Responsiveness

James Osorio MD[1], Ankur Srivastava MD[1], Samir Sethi MD[1], Natalia Ivascu Girardi MD[1], Leonard Girardi MD[2], Mario Gaudino MD[2], Brady Rippon MS, Joydeep Baidya BS[1], Sanya Rastogi BS[1], Alexandra Lopes BA[1], Avika Kasubhai BA[1], Kane Pryor MD[1]

1 Department of Anesthesiology, Weill Cornell Medical College, New York City, NY

2 Department of Cardiothoracic Surgery, Weill Cornell Medical College, New York City, NY

Background:

- Identification of patients who are fluid-responsive is important in the management of those who are hemodynamically unstable.
- Using static measures such as CVP, does not always accurately and reliably identify fluid responsiveness.
- Several studies suggested that there is a correlation between cardiac US measures and invasive cardiac output (CO) via pulmonary artery catheter (PAC), and therefore point-of-care US can be potentially used to determine fluid responsiveness in critically ill and surgical patients.

Objective:

To determine a correlation between carotid US and PAC CO measures in postoperative cardiac surgery patients.

Methods:

Study Design: Prospective cohort study

Patient Population: Postoperative cardiac surgery patients

Measurements: Carotid US images were obtained concurrently with PAC CO measurements upon arrival to the ICU and 1-hour after arrival.

All measurements were obtained before and after a fluid challenge (passive leg raise).

Fluid responsiveness by carotid US:

1) Increase in carotid blood flow by 10% after a fluid challenge (after passive leg raise)
2) Increase in corrected flow time (FTc) challenge by 7 msec (after passive leg raise)
3) Change in respiratory peak carotid systolic velocity by 10% (at baseline, prior to passive leg raise)

Statistical analysis: Sample size calculation estimated that 50 patients would have 90% power to detect a correlation of 0.59 (alpha = 0.05). The correlation between changes in US and PAC measures was evaluated first with Pearson's correlation coefficients. These associations were further tested using standardized linear regression models in a sensitivity analysis. Agreement between carotid US fluid responsiveness categories (outlined above) and cardiac classifications (by 10% change) was evaluated using a weighted Cohen's kappa. Results are reported at an α = 0.05 significance level.

Figure 1

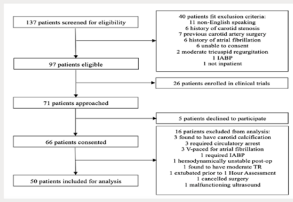

Figure 2

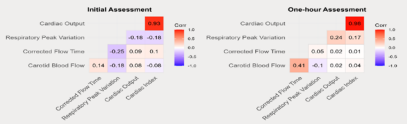

Pearson's correlations comparing the change from pre- to post-passive leg raise in carotid measures and change in PAC cardiac output measures.

Table 1

Variable	Initial Assessment β (95% Confidence Interval)		One Hour Assessment β (95% Confidence Interval)	
	Cardiac Output	Cardiac Index	Cardiac Output	Cardiac Index
Model 1 (Unadjusted)				
Carotid Blood Flow	0.08 (-0.22, 0.38)	-0.08 (-0.39, 0.22)	0.02 (-0.29, 0.32)	0.04 (-0.27, 0.35)
Corrected Flow Time	0.09 (-0.22, 0.39)	0.10 (0.20, 0.40)	0.02 (-0.28, 0.33)	0.01 (0.29, 0.32)
Respiratory Peak Variation	-0.18 (-0.48, 0.11)	-0.18 (-0.48, 0.12)	0.24 (-0.06, 0.54)	0.18 (-0.12, 0.48)
Model 2 (Adjusted)				
Carotid Blood Flow	0.12 (-0.22, 0.46)	-0.05 (-0.38, 0.29)	-0.15 (-0.44, 0.14)	-0.10 (-0.41, 0.21)
Corrected Flow Time	0.13 (-0.19, 0.46)	0.14 (-0.17, 0.46)	0.06 (-0.23, 0.35)	0.06 (-0.24, 0.37)
Respiratory Peak Variation	-0.18 (-0.51, 0.15)	-0.15 (-0.47, 0.17)	0.14 (-0.16, 0.46)	0.06 (-0.26, 0.38)

Associations between change in carotid measures and change in PAC cardiac output measures from pre- to post-passive leg raise. Results are reported as standardized betas from linear regressions with corresponding 95% confidence intervals. **Model 1** reports a crude association while **Model 2** reports an association adjusted for sex, body surface area, and disease history.

Results:

- Fifty patients who met inclusion criteria were enrolled in this study (Figure 1)
- Correlation analysis between carotid US and PAC measurement did not show any significant association (Figure 2) However, weak correlations between change in respiratory peak variation and both cardiac output and cardiac index were observed. (Figure 2).
- These associations were further analyzed through linear regression models, both unadjusted and adjusted for demographics (Table 1). No significant associations were detected between US and PAC measurements
- Carotid and cardiac PAC measures were further analyzed using sensitivity analysis by categorizing changes from pre- to post-passive leg raise. There was no significant agreement between any dichotomized changes in carotid measures (-10%, +10%) and any dichotomized changes in cardiac measures (all p >0.10 for weighted kappa) for either assessment interval (data not shown).

Limitations:

- Single center study
- Relatively small sample size

Conclusion:

- In this study of 50 patients, we were not able to detect a meaningful association between changes in carotid PoCUS measures with changes in cardiac output as measured by PAC after a passive leg raise that served as a surrogate fluid bolus.
- Additional studies with larger sample sizes are needed to evaluate the use of PoCUS of the carotid artery as a non-invasive method to accurately and reliably assess fluid responsiveness in postoperative cardiac surgery patients.

Weill Cornell Medicine

ISHLT 2023 43rd ANNUAL MEETING & SCIENTIFIC SESSIONS
Wednesday, 19 April – Saturday, 22 April
Colorado Convention Center | Denver, CO USA

The IMPACT Score: Does Sex Matter?

Mandisa Jones MD[1], Virginia Tangel MA, MSc[2], Robert S White MD, MS[1], Lisa Q Rong MD, MSCE[1]

[1]*Anesthesiology, Weill Cornell NY Presbyterian, New York, NY,*
[2]*Anesthesiology, Weill Cornell, New York, NY*

Introduction

Women account for 58% of annual heart failure related deaths. The primary objective of this study was to externally validate the IMPACT score and assess differences in score performance between male and female orthotopic heart transplant (OHT) recipients.

Methods

First time adult single OHT recipients from 2009-2018 in ISHLT registry were included. An IMPACT score was calculated and logistic regression models constructed for entire sample and stratified by sex. Model discrimination was assessed with AUROC and calibration was assessed graphically.

Results

For 1-yr mortality, the AUROC (95% CI) for the full sample was 0.59 (0.57-0.60); 0.58 (0.55-0.61) for women; 0.59 (0.59-0.61) for men. 1-yr mortality was 9.4% in the overall cohort, with no difference in mortality by sex (9.0% vs 9.6% women vs men, p=0.22).

Conclusions

IMPACT score exhibited poor discrimination and calibration in the ISHLT 2009-2018 cohort overall and by sex. There was no 1-yr mortality difference between the sexes. This challenges the assignment of 3 additional points for female sex in the calculation of this score, resulting in higher IMPACT scores for women despite equivalent 1-yr survival with men.

Table 1 Baseline Characteristics of the Study Population

Variable[a]	Study cohort (N = 20,921)	Females (N=5,411)	Males (N=15,510)	P value
Age, years	56 (47-63)	54 (42-61)	57 (48-63)	<0.001
Heart Failure etiology				
Idiopathic	7,495 (35.7%)	2,061 (38.1%)	5,414 (34.9%)	<0.001
Ischemic	6,475 (32.2%)	901 (16.7%)	5,844 (37.7%)	<0.001
Congenital	603 (2.9%)	230 (4.3%)	373 (2.4%)	<0.001
Other	2,101 (10.0%)	667 (12.3%)	1,434 (9.3%)	<0.001
Hypertension	6,637 (31.7%)	1,465 (27.1%)	5,172 (33.4%)	<0.001
Diabetes mellitus	5,747 (27.5%)	1,217 (22.5%)	4,530 (29.2%)	<0.001
Creatinine clearance,[b] ml/min	79.5 (60.8 – 103.7)	72.0 (53.9-96.1)	81.8 (63.5-105.7)	<0.001
Dialysis	492 (2.4%)	109 (2.0%)	383 (2.5%)	0.06
Serum bilirubin, mg/dl	0.7 (0.5 – 1.1)	0.65 (0.4-1.0)	0.8 (0.5-1.2)	<0.001
Mechanical ventilation	342 (1.6%)	86 (1.6%)	256 (1.7%)	0.76
Temporary circulatory support[c]	569 (2.7%)	161 (3.0%)	408 (2.6%)	0.179
Ventricular assist device				
Early generation[d]	331 (1.6%)	86 (1.6%)	245 (1.6%)	0.961
Late generation[e]	2,721 (13.0%)	641 (11.9%)	2,080 (13.4%)	0.003
HeartMate II/III	6,051 (28.9%)	1,098 (20.3%)	4,953 (31.9%)	<0.001
Intra-aortic balloon pump	1,298 (6.2%)	340 (6.3%)	958 (6.2%)	0.779
Ischemic time, hours	3.13 (2.40 – 3.81)	3.13 (2.38-3.82)	3.13 (2.40-3.82)	0.5511

[a]Continuous data are presented as median (interquartile range) and categoric data as number (%) of the overall cohort, unless otherwise specified.
[b]Based on Cockcroft-Gault calculation: = {[140 – age (years)] × weight (kg)/[72 × plasma creatinine (mg/dl)]} × (0.85 if female).

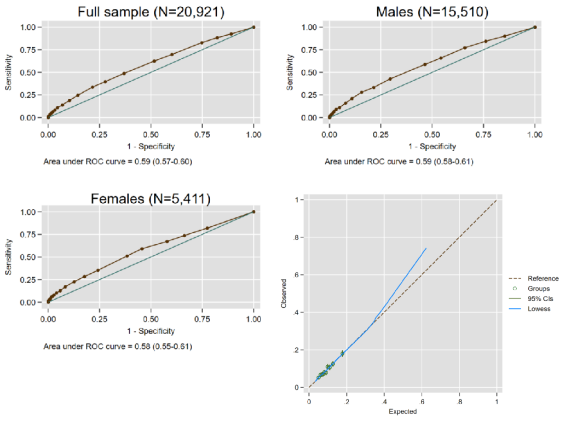

Measuring Ascending Aortic Aneurysms with Intraoperative TEE: Validation via CMR

Lisa Q. Rong, MD, Sena Chun, MD, Hannah Agoglia BA, Pablo Villar Calle MD, Richard Thalappillil MD, Andrew Martinez BA, Aneri Patel BA, Jiwon Kim MD, Leonard N. Girardi MD, Richard B. Devereux MD, Mario Gaudino MD PhD, Jonathan W. Weinsaft MD
Department of Anesthesiology, Weill Cornell Medicine, New York-Presbyterian Hospital, New York, NY

Introduction

- For patients with ascending aortic aneurysms, aorta size plays a significant role in risk stratifying patients and guiding clinical management. Aortic diameter is the greatest predictor of acute aortic syndromes – dissection and rupture.
- While the gold standard of measuring AA aneurysms is by CT and CMR, TEE is an alternative aortic imaging modality that has the benefit of providing real-time information during surgery.
- We hypothesized that TEE would be an accurate modality to measuring ascending and descending aortic diameters compared to CMR.

Methods

- Study population included a prospective cohort of 30 patients with ascending aortic aneurysms undergoing surgery.
- Patients had CMR within 30 days prior to surgery. Intraoperative TEE was performed by cardiac anesthesiologist and standard TEE views were obtained in 2D and 3D.
- Statistical Analysis: Paired t-tests were completed to compare measurement means between the 2 imaging modalities. Pearson's correlation was performed to assess the relationship between TEE and CMR. Bland–Altman analysis was used to determine the bias and limits of agreement between the measurements.

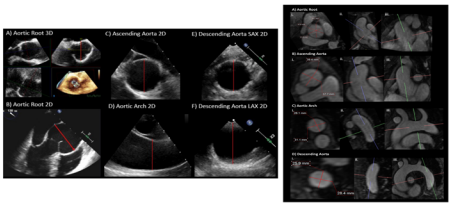

Figures 1 and 2: Representative examples of thoracic aortic diameter measurements from intraoperative TEE (left) and CMR (right). On left in TEE A) aortic root 3D, B) aortic root 2D, C) ascending aorta 2D, D) aortic arch 2D, E) descending in short axis, and F) descending aorta in long axis. On right in CMR A) aortic root, B) ascending aorta, C) aortic arch, D) descending aorta. All TEE measurements were taken with a leading-edge to leading-edge convention during end diastole and before surgical incision, during a hemodynamically stable point of surgery. All CMR measurements were taken with an inner-edge to inner-edge convention.

Results

- 30 patients were included in the study - mean age 53 years old with 25 male and 5 female patients. Mean time between the preoperative CMR and surgery was 14 days.
- 73% had valve-sparing procedures, 33% had bicuspid aortic valves, and 23% had genetically mediated aortopathies with 16.7% being Marfan's.

Aortic Segments	MRI/TEE n	MRI/ TEE mean diameter in cm ± SD (dependent variable)	TEE n	TEE mean diameter in cm ± SD (independent variable)	r value	P value ¶	Bias (cm)	Standard Deviation (cm)	Lower LOA (cm)	Upper LOA (cm)
Aortic Root	30	4.53 ± 0.52	25	4.54 ± 0.59	0.94	<0.001	**0.04**	0.22	-0.39	0.48
Ascending Aorta	30	4.39 ± 0.96	27	4.19 ± 0.86	0.98	<0.001	**0.14**	0.19	-0.23	0.51
Aortic Arch	30	2.90 ± 0.36	29	2.84 ± 0.41	0.88	<0.001	**0.05**	0.20	-0.33	0.44
Mid-Descending Aorta	30	2.66 ± 0.34	30	2.52 ± 0.34	0.91	<0.001	**0.13**	0.14	-0.15	0.41
Aortic Root (MRI) vs. Aortic Root 2D (TEE)	30	4.53 ± 0.52	30	4.45 ± 0.57	0.95	<0.001	**0.08**	0.18	-0.28	0.44
Ascending Aorta (MRI) vs. Ascending LAX 2D (TEE)	30	4.39 ± 0.96	30	4.27 ± 0.86	0.97	<0.001	**0.12**	0.24	-0.36	0.60
Aortic Root Sinus (MRI) vs. Aortic Root 3D (TEE)	30	4.67 ± 0.55	25	4.54 ± 0.59	0.97	<0.001	**0.18**	0.16	-0.13	0.50
Aortic Root Sinus (MRI) vs. Aortic Root 2D (TEE)	30	4.67 ± 0.55	30	4.45 ± 0.57	0.97	<0.001	**0.22**	0.13	-0.04	0.48
Aortic Root 3D (TEE) vs. Aortic Root 2D (TEE)	25	4.54 ± 0.59	30	4.45 ± 0.57	0.97	<0.001	**0.06**	0.15	-0.25	0.36
Ascending Aorta 3D (TEE) vs. Ascending LAX 2D (TEE)	27	4.19 ± 0.86	30	4.27 ± 0.86	0.95	<0.001	**-0.03**	0.26	-0.54	0.49

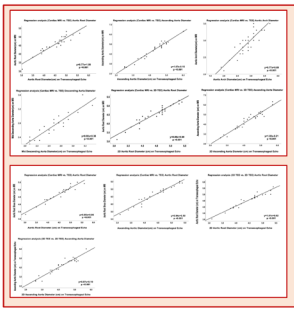

Figure 3: Pearson's correlations between intraoperative TEE and CMR-derived thoracic aortic diameters.

Ascending aortic diameters via CMR and intraoperative TEE correlated significantly at all levels with r values ranging between 0.88 at the aortic arch to 0.98 at the ascending aorta, p < 0.001 for all.

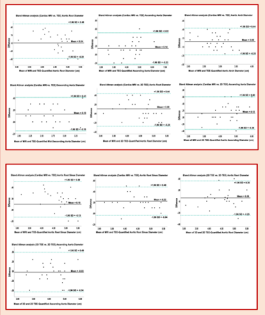

Figure 4: Bland Altman analysis of TEE and CMR derived thoracic aortic diameters.

Absolute TEE measurements were smaller than CMR-derived measurements. However, Bland-Altman analysis demonstrates a small mean difference between the two imaging modalities - varying from 0.04 cm at the aortic root to 0.22 cm at the aortic root sinus (CMR) vs. aortic root 2D (TEE) and was less than 5% at all levels. The average mean difference was 0.11 cm. There were also relatively narrow limits of agreement, ranging from 0.52 cm at the aortic root sinus (CMR) vs. aortic root 2D (TEE) to 1.03 cm at the ascending aorta 3D (TEE) vs. 2D LAX (TEE).

Discussion/ Conclusion

- We found excellent correlation between MRI measurements of the thoracic aorta and intraoperative TEE measurements.
- TEE did slightly underestimate CMR measurements; however, the mean difference between the two measurements was small and the limits of agreement were narrow.
- This study supports the use of TEE to assist surgical decision-making on aortic intervention in the OR in patients undergoing cardiac surgery with concurrent aortic disease by demonstrating excellent correlation in aortic diameter between MRI and TEE.

References

1. Hiratzka LF, Bakris GL, Beckman JA, et al. 2010 ACCF/AHA/AATS/ACR/ASA/SCA/SCAI/SIR/STS/SVM guidelines for the diagnosis and management of patients with Thoracic Aortic Disease: a report of the American College of Cardiology Foundation/American Heart Association Task Force on Practice Guidelines, American Association for Thoracic Surgery, American College of Radiology, American Stroke Association, Society of Cardiovascular Anesthesiologists, Society for Cardiovascular Angiography and Interventions, Society of Interventional Radiology, Society of Thoracic Surgeons, and Society for Vascular Medicine. *Circulation* 2010; **121**: e266-369.
2. Nienaber CA, Eagle KA. Aortic dissection: new frontiers in diagnosis and management: part I: from etiology to diagnostic strategies. *Circulation* 2003; **108**: 628-35.
3 Nicoara A, Skubas N, Ad N, et al. Guidelines for the Use of Transesophageal Echocardiography to Assist with Surgical Decision-Making in the Operating Room: A Surgery-Based Approach: from the American Society of Echocardiography in Collaboration with the Society of Cardiovascular Anesthesiologists and the Society of Thoracic Surgeons. *J Am Soc Echocardiogr* 2020; **33**: 692-734
4. Hahn RT, Abraham T, Adams MS, et al. Guidelines for performing a comprehensive transesophageal echocardiographic examination: recommendations from the American Society of Echocardiography and the Society of Cardiovascular Anesthesiologists. *J Am Soc Echocardiogr* 2013; **26**: 921-64
5. Lang RM, Badano LP, Mor-Avi V, et al. Recommendations for cardiac chamber quantification by echocardiography in adults: an update from the American Society of Echocardiography's Guidelines and Standards Committee and the Chamber Quantification Writing Group, developed in conjunction with the European Association of Echocardiography, a branch of the European Society of Cardiology. *J Am Soc Echocardiogr* 2005; **18**: 1440-63
6. Rodriguez-Palomares JF, Teixido-Tura G, Galuppo V, et al. Multimodality Assessment of Ascending Aortic Diameters: Comparison of Different Measurement Methods. *J Am Soc Echocardiogr* 2016; **29**: 819-26.e4
7. Rong LQ, Palumbo MC, Rahouma M, et al. Descending aortic strain quantification by intra-operative transesophageal echocardiography: Multimodality validation via cardiovascular magnetic resonance. *Echocardiography* 2020; **37**: 1820-7

Weill Cornell Medicine
NewYork-Presbyterian

Perioperative Pulmonary Artery Catheter Use is Associated with Increased In-Hospital Mortality in Cardiac Surgical Patients: A Systematic Review and Meta-Analysis

Grant Luhmann MM[1], Arnaldo Dimagli MD[2], Antonino Di Franco[2], Michelle Demetres MLS[3], Sena Chun MD[1], Lisa Q. Rong MD[1]

[1]Department of Anesthesiology, Weill Cornell Medicine, New York, NY, USA
[2]Department of Cardiothoracic Surgery, Weill Cornell Medicine, New York, NY, USA
[3]Information Technology and Services, Weill Cornell Medicine, New York, NY, USA.

Contact: Grant Luhmann gml4001@med.cornell.edu

Introduction

- Pulmonary artery catheters (PACs) provide real-time hemodynamic feedback e.g. PA pressure, cardiac output and are widely used in the cardiac operating room
- However, no large-scale randomized trials have been conducted on their use in the cardiac surgical population
- We hypothesized that, in patients undergoing cardiac surgery, PACs are associated with decreased in-hospital mortality compared to patients who do not receive a PAC
- Secondary Outcomes: length of ICU stay, cost of hospitalization, fluid volume given, intubation time, inotrope use, acute kidney injury (AKI), stroke, myocardial infarction (MI), and infection risk

Methods

Design: Systematic review and meta-analysis according to Preferred Reporting Items for Systematic Reviews and Meta-Analysis (PRISMA) statement[1]

Inclusion Criteria

- Patients undergoing cardiac surgery
- Randomized controlled trials or comparative observational studies
- Intervention group receives PAC, comparator does not
- In-hospital mortality is reported

Exclusion Criteria

- Potential patient overlap in database studies

Analysis: RStudio

- Outcomes assessed using random-effects model and heterogeneity assessed with I^2 test
- Binary outcomes summarized as odds ratios (OR) with 95% confidence interval (CI). Continuous outcomes summarized as standardized mean difference (SMD)
- Bias risk assessed by 2 authors using ROBINS-I tool[2] (bias can be rated low, moderate, serious, critical)

Fig. 1. PRISMA flow diagram of screened studies

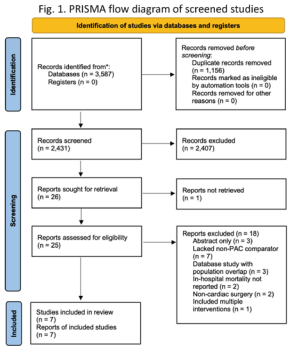

Table 1. Characteristics of included studies

Author	Year	N	Design	Month/year of surgery	ROBINS-I Bias Risk	Surgical Population	Exclusion criteria	Comparison	Statistical Adjustment
Brown et al.	2021	7,038	Retrospective observational, single-center	2010-2018	Low	CABG, single valve, CABG + single valve	Procedures not listed to the left	CVC	Propensity matched cohorts
Pearson et al.	1989	226	Prospective randomized	N/A; 9-month enrollment	Serious	CABG, valve, CABG + valve	Non-elective surgical status	CVC	None
Ramsey et al.	2000	13,907	Retrospective observational, database	1997	Serious	CABG	Emergent surgical status	No PAC	Multivariate regression
Schwann et al.	2011	2,456	Retrospective observational, database	11/1996-6/2000	Low	CABG	Subjects receiving TEE	No PAC	Propensity matched cohorts
Stewart et al.	1998	194	Retrospective observational, single-center	4/1996-10/1996	Serious	Low-risk CABG	N/A; eligibility for CVC based on specific criteria	CVC	Multivariate regression
Tuman et al.	1989	1,094	Prospective observational	N/A	Serious	CABG	Non-elective surgical status	CVC	Stratified patients into 3 levels of preoperative risk, analyzed independently
Xu et al.	2015	848	Retrospective observational, single-center	6/2012-12/2012	Low	CABG	Repeat surgery	No PAC	Propensity matched cohorts

Fig. 2. Forest plot of odds ratios (PAC vs. no PAC) for in-hospital mortality of cardiac surgery patients in included studies

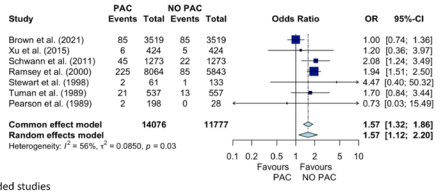

Results

2,431 records screened ➔ 7 studies analyzed totaling 25,853 unique patients

- 14,076 patients with PACs
- 11,777 without PACs
- 22,927 (88.6%) underwent CABG

PAC use was associated with significantly increased in-hospital mortality (OR 1.57; 95% CI 1.12-2.20, p = 0.04)

- PAC use was also associated with significantly increased odds of intraoperative inotrope use, longer ICU stay, and longer intubation time
- No significant differences between groups in fluid volume administered or odds of postoperative MI, AKI, stroke, or infection

Discussion

In this systematic review and meta-analysis, we found that PAC use in cardiac surgery patients was associated with significantly increased risk of in-hospital mortality.

Limitations:

- Sicker patients possibly more likely to receive PACs
- 88.6% of patients received CABG, a lower-mortality surgery
- Most studies observational, 4 out of 7 have serious risk of bias per ROBINS-I

Conclusion

PAC use was associated with significantly increased in-hospital mortality as well as significantly increased odds of intraoperative inotrope use, longer ICU stay, and longer intubation time. However, applicability of findings is limited as several studies had high risk of bias and overall population had low representation of valvular procedures.

References:
1. Page MJ, McKenzie JE, Bossuyt PM, Boutron I, Hoffmann TC, Mulrow CD, et al. The PRISMA 2020 statement: an updated guideline for reporting systematic reviews. BMJ 2021;372:n71. doi: 10.1136/bmj.n71
2. Sterne JAC, Higgins JPT et al. ROBINS-I: a tool for assessing risk of bias in non-randomized studies of interventions. BMJ 2016; 355: i4919; doi: 10.1136/bmj.i4919.

Distal Aortic Biomechanics after Transcatheter versus Surgical Aortic Valve Replacement

William Zheng[1], Andrew Martinez[1], Richard Devereux MD[1], Jonathan Weinsaft MD[1], Mario Gaudino MD[1], Lisa Q. Rong MD[1]

[1]Department of Anesthesiology, Weill Cornell Medicine, New York, NY 10065

Introduction

- Previous studies have demonstrated similar efficacy and outcomes for patients who undergo transcatheter aortic valve replacement (TAVR) and surgical aortic valve replacement (SAVR), and there is an ongoing trend to expand TAVR interventions to a younger population.
- However, the differential impact of these two procedures on aortic biomechanics is not well understood. Aortic valve disease is often associated with concurrent aortopathy, and changes in distal aortic energy propagation after TAVR vs SAVR may affect distal aortic aneurysm growth and aortic disease progression.
- Global circumferential strain (GCS) is a well-validated measurement of arterial stiffness and aortic biomechanics that can be derived from two-dimensional echocardiographic images of the aorta.
- This study utilized echo-derived GCS to assess changes in distal aortic biomechanics after TAVR and SAVR.
- We hypothesized that TAVR would increase GCS compared to SAVR due to the larger device footprint compared to bioprosthetic surgical valves.

Methods

- 40 patients undergoing TAVR and 40 patients undergoing SAVR for aortic stenosis were included.
- Transesophageal (TEE) and transthoracic (TTE) echocardiography short-axis images of the descending aorta were captured immediately before and after interventions.
- Image analysis was then performed with two-dimensional (2-D) speckle tracking echocardiography.
- GCS was calculated as: maximum deformation of the aortic circumference between systole and diastole
- Delta GCS was calculated as: post-procedural GCS – pre-procedural GCS

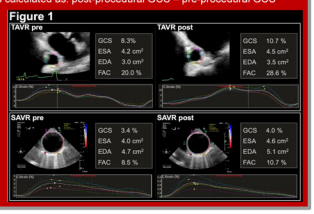

Figure 1: Representative example of patient who underwent TAVR and SAVR and their pre and post-procedural aortic strain measurements

Table 1: Descending Aortic Biomechanics Before and After Interventions

	SAVR (n=40)			TAVR (n=40)		
	Pre	Post	p	Pre	Post	p
Global circumferential strain, GCS [%]	4.4 [3.3, 5.3]	4.7 [3.9, 5.6]	0.32	10.7 [4.5, 14.6]	17.0 [6.1, 20.9]	**0.009**
Pulse Pressure Corrected Strain [%] (GCS/PP)	6.8 [5.5, 9.2]	7.6 [6.1, 10.8]	0.20	13.6 [8.6, 23.5]	26.8 [10.6, 32.0]	**0.012**
Time to Peak Strain, TTP [ms]	300 [270, 334]	195[167, 250]	<0.001	315 [285, 400]	300 [280, 385]	0.33
Δ Area/TTP [cm^2/s]	1.3 [0.9, 1.9]	2.5 [1.8, 3.1]	<0.001	2.2 [1.5, 3.7]	2.6 [1.8, 4.2]	0.22
Distensibility [10^{-3} mmHg^{-1}]	1.5 [1.1, 2.0]	1.4 [1.1, 1.7]	0.52	3.6 [1.9, 6.7]	4.9 [1.4, 7.6]	0.76
Δ Area [cm^2]	0.4 [0.3, 0.6]	0.5 [0.4, 0.6]	0.11	0.9 [0.4, 1.2]	0.7 [0.6, 1.4]	0.53
Fractional Area Change [%]	9.4 [6.8, 11.9]	10.5 [9.3, 13.5]	0.09	30.0 [9.1, 40.8]	32.9 [103, 57.1]	0.22
End Systolic Area [cm^2]	5.3 [4.1, 5.9]	4.8 [4.1, 6.0]	0.81	4.6 [3.7, 5.6]	4.4 [3.3, 5.7]	0.90
End Diastolic Area [cm^2]	4.8 [3.7, 5.7]	4.3 [3.6, 5.4]	0.65	3.3 [2.6, 4.9]	3.3 [2.5, 4.7]	0.76

Table 2: Absolute (Delta) and Relative (Percent Change) Differences Before and After Interventions

	Overall (n=80)	SAVR (n=40)	TAVR (n=40)	p
Delta GCS	1.5 [-0.1, 3.4]	0.15 [-0.6, 1.5]	2.8 [1.4, 6]	**<0.001**
Delta GCS (Mean (SE))	-----	-0.2 (0.8)	4.6 (0.8)	**0.001**
Delta GCS/PP	3.05 [-0.01, 7.7]	1.3 [-1.5, 3.2]	6.1 [1.6, 12.3]	**<0.001**
Percent_Change_GCS	21.2 [-2.3, 58]	4.4 [-10.6, 56]	28.8 [14.6, 64.6]	**0.006**
Percent_Change_GCS (Mean (SE))	-----	6.6 (12.8)	53.7 (12.8)	**0.044**
Percent_Change_GCS/PP	31.9 [0.14, 78.8]	24.5 [-17.5, 70]	36.9 [11.2, 83]	0.11
Delta EDA	-0.1 [-0.6, 0.3]	-0.04 [-0.36, 0.36]	-0.25 [-0.8, 0.3]	0.37
Delta ESA	-0.1 [-0.5, 0.5]	-0.02 [-0.36, 0.6]	-0.2 [-0.7, 0.26]	0.38
Delta FAC	1.6 [-1.8, 6.1]	1.3 [-0.5, 4.7]	1.9 [-2.1, 14.1]	0.45

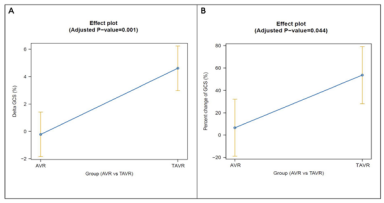

Figure 2: Effect ANCOVA plots showing A) percentage delta GCS and B) percentage delta GCS/PP (%)

Results

- The change in GCS was significant in the TAVR group but not in the SAVR group.
- Delta GCS was significantly higher in the TAVR group compared to the SAVR group.
- Percentage delta GCS was significantly higher in the TAVR group compared to the SAVR group.
- Pulse-pressure corrected GCS was significantly higher post-procedure in the TAVR group but not in the SAVR group.
- Pulse-pressure corrected delta GCS was significantly higher in the TAVR group compared to the SAVR group.
- In the fully adjusted ANCOVA model, the delta GCS and percentage delta GCS were both significantly greater in the TAVR compared to the SAVR group.
- Hemodynamic variables between the TAVR and SAVR groups were similar pre-procedurally and post-procedurally.

Conclusions

- Absolute and relative change in GCS of the descending aorta was significantly greater after TAVR than after SAVR.
- TAVR is associated with increased energy propagation, which may be associated with future adverse aortic remodeling such as aneurysm and dissection.
- With an increasing number of patients undergoing TAVR intervention, dedicated post-procedural follow-up surveillance imaging may be required, especially in high risk populations.

Limitations

- TAVR group primarily used TTE whereas SAVR group used TEE to evaluate differences in GCS.
- Findings limited to time point immediately post-procedure and further longitudinal studies are necessary to explore future changes in GCS.

References

1. Smith CR, Leon MB, Mack MJ, et al. Transcatheter versus surgical aortic-valve replacement in high-risk patients. *N Engl J Med*. Jun 9 2011;364(23):2187-98. doi:10.1056/NEJMoa1103510
2. Rong LQ, Palumbo MC, Rahouma M, et al. Differential Effects of Aortic Valve Replacement on Aortic Circumferential Strain in Aortic Stenosis and Aortic Insufficiency. *J Cardiothorac Vasc Anesth*. Sep 2021;35(9):2707-2714. doi:10.1053/j.jvca.2020.10.044
3. Rong LQ, Kim J, Gregory AJ. Speckle tracking echocardiography: imaging insights into the aorta. *Curr Opin Cardiol*. Mar 2020;35(2):116-122. doi:10.1097/HCO.0000000000000706
4. Alreshidan M, Shahmansouri N, Chung J, et al. Obtaining the biomechanical behavior of ascending aortic aneurysm via the use of novel speckle tracking echocardiography. *J Thorac Cardiovasc Surg*. Apr 2017;153(4):781-788. doi:10.1016/j.jtcvs.2016.11.056

Perioperative mortality in paediatric patients: a systematic review of risk assessment tools for use in the preoperative setting

12th European Congress for Paediatric Anaesthesiology

Virginia E. Tangel, Stephan D. Krul, Robert Jan Stolker, Wichor M. Bramer, Jurgen C. de Graaff, Sanne E. Hoeks | 29 September 2022

Introduction

- The aim of this study was to systematically describe and compare the existing studies of patient-specific multispecialty risk prediction scores for perioperative mortality in pediatric populations, with the goal of guiding clinicians on which may be most appropriate for use in the preoperative setting.

Methods

- A systematic literature review of published journal articles that presented the development, extension/updating, and/or validation of a risk score which predicted all-cause mortality (up to 30 days postoperatively) in pediatric patients undergoing a procedure in which anesthesia was used. Scores needed to be applicable to surgeries in more than one non-cardiac surgical specialty and had to be able to be calculated by the anesthesiologist at the time of the pre-anesthetic assessment.

Results

- From 1,681 titles, 10 studies met inclusion criteria: nine reported the development and validation of scores, and one was an external validation of an existing score.
- Seven studies used varying years of multicenter data from the National Surgical Quality Improvement Program (NSQIP) – Pediatric Participant Use File for development and/or validation.
- The unadjusted rate of mortality in the studies ranged from 0.3% to 3.6%.
- All models showed good discrimination upon validation (AUC > 0.8). Most risk scores had high or unclear risks of bias.

Conclusion

- Before any large-scale adaptation of a particular score, prospective, fully independent external validations and further refinement of existing scores need to occur—especially in non-US and low-resource settings.

Table 2. Prediction model Risk Of Bias ASsessment Tool (PROBAST) results.

		Risk of bias				Applicability			Overall	
	Study	Participants	Predictors	Outcome	Analysis	Participants	Predictors	Outcome	Risk of bias	Applicability
1	Akbilgic *et al.* 2018a	+	+	+	-	+	+	+	-	+
2	Akbilgic *et al.* 2018b	+	+	+	?	+	+	+	?	+
3	Cooper *et al.* 2018	+	+	+	-	+	+	+	-	+
4	Kraemer *et al.* 2016	+	+	+	?	+	+	+	?	+
5	Langham *et al.* 2015	+	+	+	-	+	+	+	-	+
6	Nasr *et al.* 2017	+	+	+	+	+	+	+	+	+
7	Nasr *et al.* 2019	+	+	+	+	+	+	+	+	+
8	Rhee *et al.* 2013	+	+	+	-	+	+	?	-	?
9	Terui *et al.* 2020	+	+	+	-	+	+	+	-	+
10	Valencia *et al.* 2019	+	+	+	-	+	+	+	-	+

"+" indicates low risk of bias/low concern regarding applicability, "–" indicates high risk of bias/high concern regarding applicability, and "?" indicates unclear risk of bias/unclear concern regarding applicability.

@VirginiaTangel

Table 1. Study characteristics

	Study	Development (+/- validation) or validation only study?	Country	Setting/population
1	Akbilgic *et al.* 2018a	Development and validation	United States (majority)	NSQIP-Pediatric of African-American and white children <18 years from 2012-2014
2	Akbilgic *et al.* 2018b	Development and validation	United States (majority)	NSQIP-Pediatric from 2012-2014
3	Cooper *et al.* 2018	Development and validation	United States (majority)	NSQIP-Pediatric from 2012-2013
4	Kraemer *et al.* 2016	Development and validation	United States (majority)	NSQIP-Pediatric from 2012-2014
5	Langham *et al.* 2015	Development and validation	United States	Single pediatric hospital for 2010-2012 for development
6	Nasr *et al.* 2017	Development and validation	United States (majority)	NSQIP-Pediatric from 2012-2013
7	Nasr *et al.* 2019	Development and validation	United States (majority)	NSQIP-Pediatric from 2012-2016
8	Rhee *et al.* 2013	Development and validation	United States	General pediatric surgical population from Nationwide Inpatient Sample & Kids' Inpatient Database from 1998-2005 & Kids' Inpatient Database 2006 for 1st validation. 2nd validation is CA data from 2005-2007.
9	Terui *et al.* 2020	Development and validation	Japan	National Clinical Database (national registry) for 12 major surgical procedures from 2015. Records from 2016 from same dataset are validation.
10	Valencia *et al.* 2019	Validation only	United States	All noncardiac surgical encounters from July 2017-July 2018 at a single pediatric hospital

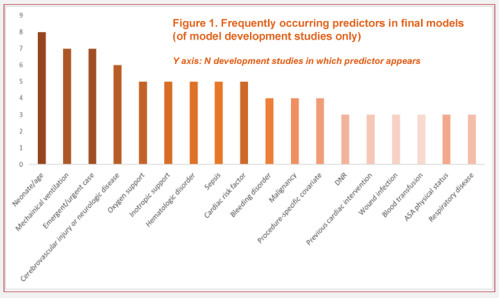

Gender Difference in Authorship and Quality of Anesthesia Clinical Practice Guidelines from 2016-2020 using the Appraisal of Guidelines for Research & Evaluation II Instrument

Lisa Q. Rong[1], Andrew P. Martinez[1], Mohamed Rahouma[3], Alexandra J. Lopes[2], Jerry Y. Lee[1], Drew N. Wright[4], Michelle Demetres[4], Bessie Kachulis[1], Sinead M. O'Shaughnessy[5]
[1] Department of Anesthesiology, Weill Cornell Medicine, New York, NY 10065, USA [2] University of California San Francisco School of Medicine, San Francisco, CA, 94143, USA [3] Department of Cardiothoracic Surgery, Weill Cornell Medicine, New York, NY 10065, USA
[4] Samuel J. Wood Library & C.V. Starr Biomedical Information Center, Weill Cornell Medicine, New York, NY 10065, USA [5] Department of Anaesthesiology, Mater Misericordiae University Hospital, Dublin. 7, Ireland

Weill Cornell Medicine
NewYork-Presbyterian

Introduction

- Women continue to be underrepresented in anesthesiology, disproportionately in academic and leadership roles. This study assessed published guidelines in leading anesthesia journals over the past 5 years, evaluating differences in women-led vs men-led guidelines in terms of author gender, quality and number.
- We hypothesized that anesthesia guidelines would be (1) predominately men-led (2) women-led guidelines would have a higher % of women authors and (3) women-led guidelines and guidelines with a higher percentage of women authors would be associated with higher quality.

Methods

Selection of journals and guidelines:

- All clinical practice guidelines published in the top 10 anesthesia journals were identified via Clarivate Analytics Impact Factor (2016-2020).
- Fifty-one guidelines were included for author, gender, and quality analysis using Appraisal of Guidelines for Research & Evaluation (AGREE) II instrument.

Extraction of Data and Guideline Classification:

- Data extracted: Year of publication, Altmetric score, number of citations, origin of first author, origin of affiliations for all authors, number and gender of authors, and appraisal tool used.
- We defined women-led as guidelines with a woman first-author and assumed that the first author was chair of the guideline committee and/or the most influential author in the guideline.

Table 1: Gender differences in authorship

n or median (IQR)	Level	Overall	Women	Men	P-value
		1052	255	797	
n		50	12	38	
Region (%)	Europe	19 (38.0)	5 (41.7)	14 (36.8)	0.21
	North America	8 (16.0)	0 (0.0)	8 (21.1)	
	Multiregional	23 (46.0)	7 (58.3)	16 (42.1)	
Journal name (%)	Anaesthesia	8 (15.7)	1 (8.3)	6 (15.8)	0.70
	Anesthesia and Analgesia	4 (7.8)	2 (16.7)	2 (5.3)	
	Anesthesiology	5 (9.8)	0 (0.0)	5 (13.2)	
	British Journal of Anaesthesia	5 (9.8)	2 (16.7)	3 (7.9)	
	Canadian Journal of Anesthesia	3 (5.9)	1 (8.3)	2 (5.3)	
	European Journal of Anaesthesiology	18 (35.3)	4 (33.3)	14 (36.8)	
	European Journal of Pain	1 (2.0)	0 (0.0)	1 (2.6)	
	Regional Anesthesia and Pain Medicine	7 (13.7)	2 (16.7)	5 (13.2)	
Specialty (%)	Cardiac	1 (2.0)	1 (8.3)	0 (0.0)	0.20
	ICU	5 (9.8)	1 (8.3)	4 (10.5)	
	OB	1 (2.0)	0 (0.0)	1 (2.6)	
	Pain	9 (17.6)	1 (8.3)	7 (18.4)	
	Pediatrics	1 (2.0)	1 (8.3)	0 (0.0)	
	Perioperative	34 (66.7)	8 (66.7)	26 (68.4)	
Total number authors		10.0 [5.0, 13.8]	9.0 [5.5, 18.8]	10.0 [5.0, 13.0]	0.69
Total number men authors		8.0 [4.0, 11.0]	7.0 [2.8, 11.8]	8.0 [4.0, 11.0]	0.75
Total number women authors		2.0 [1.0, 4.8]	3.5 [1.0, 6.0]	1.0 [1.0, 3.0]	**0.049**
Women authors per guideline (%)		25 [9, 50]	39 [32, 73]	20 [8, 40]	**0.012**
Number of societies		1 [1, 2]	1 [1, 1]	1 [1, 2]	0.61
Number of countries		3 [2, 4]	3 [2, 5]	3 [1, 4]	0.33
Number of institutions		8 [5, 11]	7 [4, 13]	8 [5, 11]	0.93
Altmetric score		29.0 [10.5, 69.5]	19.5 [8.3, 50.0]	30.0 [12.0, 71.3]	0.27
Number of citations		17.0 [9, 56]	13 [8, 40]	18 [9, 54]	0.77
Appraisal tool used (%)		39 (76.5)	9 (75.0)	29 (76.3)	0.93
Overall rating* > 5 (%)		20 (38.5)	2 (16.7)	17 (44.7)	0.16
Overall rating/ recommendation (%)	No	2 (3.9)	0 (0.0)	2 (5.3)	0.12
	Yes	20 (39.2)	2 (16.7)	17 (44.7)	
	Yes with modifications	29 (56.9)	10 (83.3)	19 (50.0)	
Objective high quality*	No	44 (86.3)	9 (75.0)	34 (89.5)	0.43
	Yes	7 (13.7)	3 (25.0)	4 (10.5)	

Figure 1: Trend of percentage and number of women authors per guideline over time from 2016-2020

P for trend= 0.593 for trend by actual number & 0.830 for trend by percent

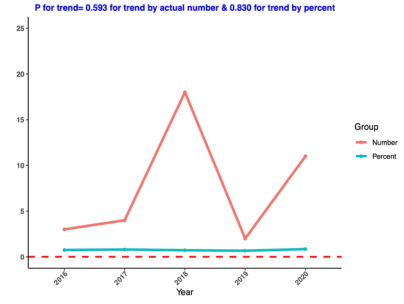

Figure 2: Assessment of trend of overall score from 2016-2020

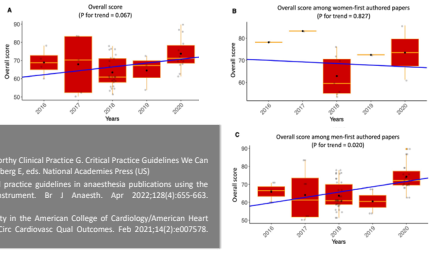

Statistical analysis

- Descriptive analyses were performed to compare men- and women-led guidelines. Linear regression was used to explore changes in the proportion of women authors through the study period as well as domain 3 score, mean overall rating, and mean overall score.

Results

- 50/51 guidelines were included: one excluded due to unidentifiable first author gender.
- 255 of 1052 (24%) of authors were women, and women-led guidelines (i.e. women first author) represented 12 out of 50 (24%) overall guidelines. (Table 1)
  - Eighteen percent (9/50) of guidelines had all-men authors, and a majority (26/50, 52%) had less than one-third women authors.
  - There was a significantly higher proportion of women authors in women-led vs. men-led guidelines, (0.39 [0.32, 0.73] vs 0.20 [0.08, 0.40], p=0.012. (Table 1)
- For quality, there was no significant difference in the overall rating or objective quality of women vs men-led guidelines.
  - There was a significant increase in the overall rating of all the guidelines over time (p=0.010), driven by the increase in overall rating among men-led guidelines, p=0.002.
  - The overall score of guidelines did not increase over time; however, they increased in men-led but not women-led guidelines (p=0.020 and 0.827, respectively). (Figure 2)

Conclusions

- There is a substantial disparity in the number of women leading and contributing to guidelines which has not improved over time.
- Women-led guidelines included more women authors.
- There was no difference in quality of guidelines by gender.

References

1. Institute of Medicine Committee on Standards for Developing Trustworthy Clinical Practice G. Critical Practice Guidelines We Can Trust. In: Graham R, Mancher M, Miller Wolman D, Greenfield S, Steinberg E, eds. National Academies Press (US)
2. O'Shaughnessy SM, Lee JY, Rong LQ, et al. Quality of recent clinical practice guidelines in anaesthesia publications using the Appraisal of Guidelines for Research and Evaluation II instrument. Br J Anaesth. Apr 2022;128(4):655-663. doi:10.1016/j.bja.2021.11.037
3. Rai D, Tahir MW, Waheed SH, et al. National Trends of Sex Disparity in the American College of Cardiology/American Heart Association Guideline Writing Committee Authors Over 15 Years. Circ Cardiovasc Qual Outcomes. Feb 2021;14(2):e007578. doi:10.1161/circoutcomes.120.007578

Contact: Lisa Q. Rong lir9065@med.cornell.edu

The Development and Analysis of a Chronic Pain & Multidisciplinary Spine Outcomes Registry

Primary Investigator: Lisa R. Witkin, MD, MS.
Department of Anesthesiology 15th Research Exposition | October 31, 2023

Weill Cornell Medicine
NewYork-Presbyterian

Investigators:

(project-specific PIs are represented in bold)

Lisa R. Witkin, MD, MS. Jacky Choi, MPH. Jessica Kim, MS. Abbey Gilman, BS. Silis Jiang, PhD. Abha Kasubhai, BA. Jonathan Tobin, PhD.

Background

Pain treatments should be selected according to patients' response to therapy, yet these outcomes are often not objectively measured. It is imperative to measure not just pain severity, but also the impact of chronic pain on overall functioning and health-related quality of life (HrQoL). An electronic new patient questionnaire and patient reported outcomes (PRO) was integrated into routine care in chronic pain management clinics across Weill Cornell Medical Center (WCMC), aligning with the IOM recommendations and the National Pain Strategy. The Patient Reported Outcomes Measurement Information System (PROMIS) is a psychometrically-validated dynamic tool to measure generic HrQoL outcomes from the patient perspective based on physical, social, mental, and global health domains. The objective of this research is to characterize the patient populations that present to our multidisciplinary spine center for evaluation and treatment, and to understand patient, sociodemographic, and disease characteristics and treatments that are associated with the most severe pain and impairment. The secondary objective is to identify patient, and disease and treatment characteristics that are associated with worse outcomes and to identify non-responders that fail to improve with treatment, in patients with radiculopathy.

Cohort Selection

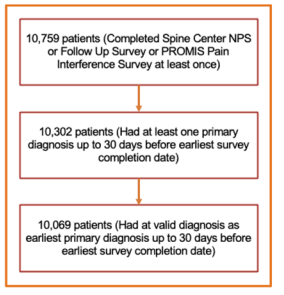

Distribution of Baseline Pain Severity Scores

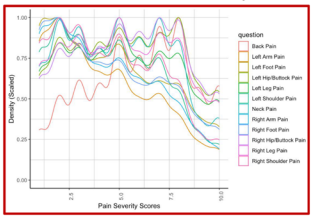

Baseline Pain Severity Score (Collapsed)	
Mean (SD)	5.1 (2.1)
Median (IQR)	5.0 (3.5, 6.5)
Missing	353

Mixed Model GLMM Results with Missing Indicators

Pain Severity

Characteristic	Estimate	95% CI[1]	p-value
Sex			
Male	—	—	
Female	0.43	0.17, 0.69	0.001
Missing	-0.43	-2.7, 1.8	0.70
Race			
White	—	—	
Black or African American	0.48	0.05, 0.91	0.030
Other	0.49	0.09, 0.88	0.016
Missing	0.15	-0.20, 0.51	0.40
Asian	0.41	-0.26, 1.1	0.23
Tobacco Use			
Never Smoker	—	—	
Current Smoker	0.67	0.21, 1.1	0.005
Former Smoker	0.08	-0.20, 0.35	0.58
Missing	-0.1	-1.0, 0.98	0.98
Insurance			
Private	—	—	
Medicare	0.40	0.07, 0.73	0.018
Missing	0.12	-0.51, 0.76	0.70
Medicaid	0.55	0.13, 0.97	0.010
Other	-1.8	-5.1, 1.4	0.26
Department			
WCMC NEUROLOGY SPINE CENTER	—	—	
WCMC NEURO SURG SPINE CENTER	-0.04	-0.58, 0.50	0.89
WCMC PAIN MGMT CENTER	0.16	-0.35, 0.66	0.54
WCMC REHAB MEDICINE SPINE CENTER	-0.17	-0.78, 0.43	0.57

PROMIS Pain Interference

Characteristic	Estimate	95% CI[1]	p-value
BMI			
Normal	—	—	
Obese	1.7	0.27, 3.2	0.021
Overweight	1.5	0.05, 2.9	0.043
Missing	1.4	-0.38, 3.1	0.12
Underweight	0.91	-2.1, 3.9	0.55
Race			
White	—	—	
Black or African American	1.2	-0.52, 3.0	0.17
Other	1.6	0.02, 3.2	0.048
Missing	0.90	-0.59, 2.4	0.24
Asian	3.4	0.59, 6.2	0.018
Department			
WCMC NEUROLOGY SPINE CENTER	—	—	
WCMC NEURO SURG SPINE CENTER	2.3	0.09, 4.5	0.041
WCMC PAIN MGMT CENTER	0.74	-1.3, 2.7	0.47
WCMC REHAB MEDICINE SPINE CENTER	1.4	-1.4, 4.2	0.32
Baseline Pain Severity			
Not severe	—	—	
Severe	4.4	2.7, 6.1	<0.001
PROMIS Sleep Measure			
Normal	—	—	
Severe	6.3	4.2, 8.4	<0.001
Moderate	3.5	2.2, 4.8	<0.001
Mild	2.0	0.61, 3.5	0.005
Missing	3.5	0.45, 6.5	0.024
PROMIS Composite Anxiety/Depression Measure			
No	—	—	
Missing	3.9	-2.0, 9.8	0.19
Yes	2.9	1.8, 4.0	<0.001

Results and Conclusions

- The Spine Center sees patients with high impact chronic pain, as defined by severe pain intensity, with moderate pain interference and impairment of physical functioning
- The longitudinal analysis of the radiculopathy cohort suggests that several key factors are associated with worse outcomes, including:
  - any level of sleep interference, and any level of depression or anxiety on PROMIS scales
  - several lifestyle, including smoking and BMI
  - sociodemographic factors, such as being female, or Black/African American, or Asian race
- This work begins to explore predictors of poor outcomes that highlight an opportunity for an intervention targeting modifiable risk factors
- Identification of health disparities with respect to gender and race/ethnicity, which require further research
- Ultimately, the goal is to improve chronic pain treatments, and reduce disability, which would result in significant cost-savings and a decreased public health burden.
- Given the aging population and the setting of the ongoing opioid epidemic, precision treatment of chronic pain will match the optimal treatments with patient characteristics to produce the best outcomes.

Citations

1. Relieving Pain in America: A Blueprint for Transforming Prevention, Care, Education, and Research. Washington (DC); 2011
2. Mehta N, Irrunse CE, Horn SD, Witkin LR. Using Chronic Pain Outcomes Data to Improve Outcomes. Anesthesiol Clin. 2016;34(2):395-408.
3. Ashburn MA, Witkin L. Integrating outcome data collection into the care of the patient with pain. Pain. 2012;153(9):1849-50.
4. Buchbinder R, Blyth FM, March LM, Brooks P, Woolf AD, Hoy DG. Placing the global burden of low back pain in context. Best Pract Res Clin Rheumatol. 2013;27(5):575-89.
5. Wu A, March L, Zheng X, Huang J, Wang X, Zhao J, et al. Global low back pain prevalence and years lived with disability from 1990 to 2017: estimates from the Global Burden of Disease Study 2017. Ann Transl Med. 2020;8(6):299.
6. Asad TD, Kalani M, Wolf T, Kearney A, Lee Y, Fiannery L, et al. Building an electronic health record integrated quality of life outcomes registry for spine surgery. J Neurosurg Spine. 2016;24(1):179-85.
7. Babington JR, Edwards A, Wright AK, Dykstra T, Friedman AS, Sethi RK. Patient-Reported Outcome Measures: Utility for Predicting Spinal Surgery in an Integrated Spine Practice. PM R. 2018;10(7):724-9.
8. Chapman JR, Norvell DC, Hermsmeyer JT, Bransford RJ, DeVine J, McGirt MJ, et al. Evaluating common outcomes for measuring treatment success for chronic low back pain. Spine (Phila Pa 1976). 2011;36(21 Suppl):S54-68.
9. Turk DC, Dworkin RH, Allen RR, Bellamy N, Brandenburg N, Carr DB, et al. Core outcome domains for chronic pain clinical trials: IMMPACT recommendations. Pain. 2003;106(3):337-45.
10. Dworkin RH, Turk DC, Farrar JT, Haythornthwaite JA, Jensen MP, Katz NP, et al. Core outcome measures for chronic pain clinical trials: IMMPACT recommendations. Pain. 2005;113(1-2):9-19.
11. Deyo RA, Dworkin SF, Amtmann D, Andersson G, Borenstein D, Carragee E, et al. Report of the NIH Task Force on Research Standards for Chronic Low Back Pain. Int J Ther Massage Bodywork. 2015;8(3):16-33.

Multicenter Perioperative Outcomes Group (MPOG)

Local MPOG Leadership: Hugh Hemmings, MD, PhD. Patricia Mack, MD. Kane Pryor, MD. Zachary Turnbull, MD, MBA, MS.

Department of Anesthesiology 15th Research Exposition | October 31, 2023

Weill Cornell Medicine
NewYork-Presbyterian

Investigators:

Hugh Hemmings, MD, PhD. Kane Pryor, MD. Lisa Rong, MD. Virginia Tangel, MA, MSc. Zachary Turnbull, MD, MBA, MS. Robert White, MD, MS.

Background

The Multicenter Perioperative Outcomes Group (MPOG [http://mpog.org]; founded 2008) is a perioperative registry of anesthesia care electronic health records from institutions located in the U.S and the Netherlands for surgical and diagnostic procedures. It contains over 24 million cases and 408 million medication records. The overall purpose of the database is to create a resource for clinical researchers to investigate outcomes following surgery. MPOG uses electronic health record and administrative data to analyze the interplay between patient comorbidities, surgical procedure, perioperative care, interventions, and postoperative outcomes. Researchers are able to query the database using standard database methods, and access enough patient records to identify trends that are not visible in single institutions.

Research

The goal of MPOG research is to accelerate outcomes research, investigate perioperative adverse events and publish in high impact journals to advance knowledge and improve patient care.

Quality

Our goal is to improve the care of patients undergoing anesthesia by reducing unexplained variation in practice and collaborating with anesthesia providers to define best practices.

Updates

Before the end of 2023, NYP Brooklyn Methodist Hospital will be added as a participant to the MPOG database and will be contributing their perioperative data for quality assurance purposes. This is currently in the legal contracting phase.

Participants

There are currently 71 consortiums that contribute to the MPOG database. Here are a few listed below:

- Weill Cornell Medicine
- University of Michigan
- Columbia University
- Stanford
- Johns Hopkins
- NYU Langone University
- Duke University
- Yale University
- Vanderbilt University
- Dartmouth College
- Memorial Sloan Kettering Hospital
- University of Pennsylvania

Current Projects in Progress

All of the current studies below are using the MPOG database to explore research questions:

- *Virginia's study*: define reference ranges for intraoperative hemodynamic measures for healthy pediatric patients undergoing non-cardiac surgery.
- *Dr. Rong's study*: describe benzodiazepine use and sources of variation during non-operating room cardiac procedures across patients, clinicians, and institutions.
- *Dr. Pryor's study*: determine (i) whether patients undergoing (a) major inpatient surgery, (b) minor inpatient surgery, or (c) outpatient surgery have a superior quality of recovery after INVA or TIVA and (ii) whether TIVA confers no more than a small (0.2%) increased risk of intraoperative awareness than INVA.
- *Dr. White's study*: examine if patient race/ethnicity is associated with the type of anesthesia (general or regional) administered in cesarean deliveries.

Project Intake

If you would like to use the MPOG database to answer research questions, please scan the QR code to put in a data request with the Center of Perioperative Outcomes (CPO).

Engineering novel pharmacology for the TREK1 K2P channel

Leila Khajoeinejad[1], Elena Riel, Gagandeep Singh, Paul M. Riegelhaupt[1*]

[1] Department of Anesthesiology, Weill Cornell Medical College Cornell Medical College

BACKGROUND

Tandem pore domain (K2P) potassium channels play a crucial role in modulating cellular resting membrane potential, thereby controlling cellular excitability. TREK1, a member of the mechanosensitive K2P subfamily, is modulated by a wide array of stimuli that include heat, stretch, pH, and volatile anesthetics, but TREK1 lacks specific and high affinity pharmacological modulators.

METHODS

In this study, we leveraged the high affinity binding of the immunomodulatory drug Rapamycin to the FKBP Rapamycin Binding (FRB) domain of mTOR, bioengineer a TREK1/FRB fusion protein sensitive to rapamycin. We designed multiple unique fusion constructs by inserting the FRB protein into the TM2/TM3 loop of TREK1 at a variety of alternative fusion sites. We then determined the functional behavior of these TREK1/FRB fusion proteins via two-electrode voltage clamp (TEVC) electrophysiology, characterizing the sensitivity of the TREK1/FRB fusions to gating by temperature.

Figure 1: Engineering a TREK1/FRB Fusion

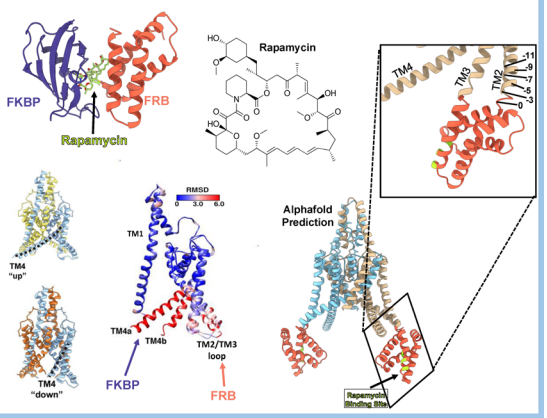

Figure 2: Functional characterization of alternative TREK1/FRB fusions by two electrode voltage clamp electrophysiology

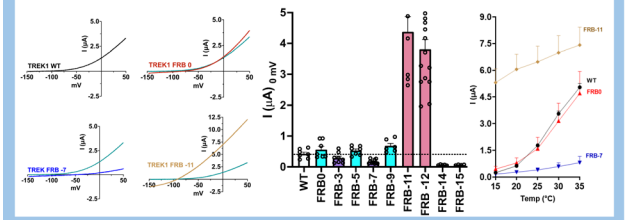

Figure 3: Rapamycin activates the engineered TREK1/FRB fusion K2P channels

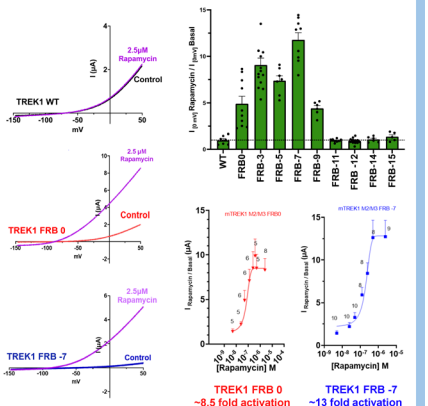

Figure 4: Utilizing rapamycin analogs that have no effect on mTOR

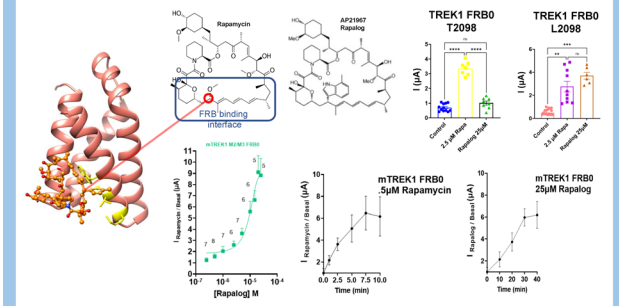

Future Plans: A TREK1 chemogenetic / optogenetic tool to silence neuronal signaling

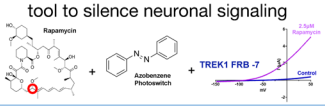

Discussion

Nearly all of the TREK1/FRB fusions yielded functional potassium channels, though altering the FRB fusion site led to varied basal channel activities and temperature sensitivities. Application of rapamycin to this panel of TREK1/FRB channels resulted in up to15-fold potentiation of TREK1 activity in the most sensitive fusion construct, with dose response studies demonstrating EC50 values as low as 63 nanomolar. By introducing a well characterized T2098L mutation into the FRB portion of the TREK1/FRB fusion protein, we were also able to activate the TREK1/FRB channel using an analog of rapamycin (AP21967) that lacks the immunomodulary activity of rapamycin.

CONCLUSION

This work yields a highly specific genetically encodable tool that can specifically activate the TREK1 channel for future in-vivo physiological studies.

Funding

NIGMS

K08GM132781

R01GM145918

High-Resolution (3.3 Å) Cryo-EM 3D model of the TASK-1 K2P Channel

Anesthesiology Research Exposition 2023

Gagandeep Singh, Paul Riegelhaupt | October 31 2023

Department of Anesthesiology, Weill Cornell Medicine, New York, NY

Background

Potassium (K+) channels are pivotal in regulating cellular electrical activity, with K2P (Two-Pore Domain Potassium) channels standing out for their distinctive structure and functional properties, contributing significantly to the maintenance of resting membrane potential and cellular excitability across various tissues [1].

Among the K2P channels, the TASK (TWIK-related acid-sensitive K+) family is notable for its extracellular pH sensitivity and is expressed widely in tissues, underscoring their broad physiological significance [2]. TASK-1, a member of this family, is particularly intriguing due to its influence on the resting membrane potential of excitable cells, such as its role in neuronal excitability, cardiac action potential duration, and renal acid-base regulation [3].

Beyond their fundamental roles, dysregulation of TASK-1 channels has been implicated in health conditions such as atrial fibrillation (AF), where altered atrial K+ currents mediated by TASK-1 channels may create a substrate for AF [4]. In pulmonary arterial hypertension (PAH), changes in TASK-1 channel expression and activity are associated with the pathophysiology of the condition, potentially increasing pulmonary vascular tone and contributing to the development of PAH [5]. In a broader context, TASK-1 channels have also been linked to pain sensation, with studies suggesting their role in influencing pain perception, thereby offering new avenues for the development of pain management strategies [6]. Cryo-EM is a unique tool to gain high-resolution structural insights governing TASK-1 channel function, with the potential to design future therapeutic applications.

Methods

Human TASK-1 protein was purified using size exclusion chromatography. Protein samples were frozen on R1.2/1.3 UltraAufoil 300 mesh grids using a Vitrobot Mark IV. Images were captured using a Krios 300kV electron microscope with a GatanK3 imaging system at 105,000X magnification. RELION was used for image processing and 3D modeling.

Results

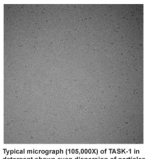

Typical micrograph (105,000X) of TASK-1 in detergent shows even dispersion of particles with minimal aggregation.

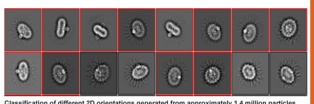

Classification of different 2D orientations generated from approximately 1.4 million particles. Red squares represent orientations used as template for initial 3D model (below).

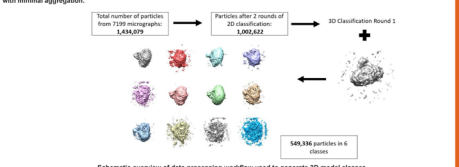

Schematic overview of data processing workflow used to generate 3D model classes.

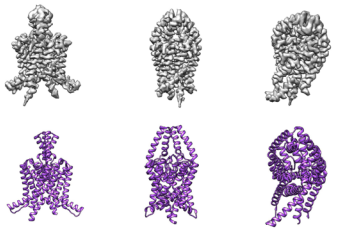

Refined 3D model of the human TASK1 K2P channel at 3.3 Å resolution is presented in front, side, and top views (from left to right). Corresponding views of the crystal structure map, 6RV3, are provided below.

Conclusions

We introduce a high-resolution 3D model of the human TASK-1 K2P ion channel, marking the first of its kind. Our 3D model validates the previously published X-ray crystallography structure[7]. Future studies will utilize this native closed-state structure to help elucidate mechanisms of ligand-protein interactions, with the aim of potentially developing innovative therapeutic applications.

References

- 1. Goldstein SA, et al. (2001). Potassium leak channels and the KCNK family of two-P-domain subunits. Nature Reviews Neuroscience, 2(3), 175-184.
- 2. Duprat F, et al. (2007). TASK, a human background K+ channel to sense external pH variations near physiological pH. The EMBO Journal, 26(5), 1034-1043.
- 3. Enyedi, P, & Czirják, G. (2010). Molecular Background of Leak K+ Currents: Two-Pore Domain Potassium Channels. Physiological Reviews, 90(2), 559-605.
- 4. Schmidt C, et al. (2015). Altered atrial K+ currents may provide a substrate for atrial fibrillation in chronic kidney disease. Clinical and Experimental Pharmacology and Physiology, 42(7), 768-778.
- 5. Bonnet S, et al. (2019). TASK1 channels in pulmonary arterial smooth muscle cells underlie a sex difference in the response to hypoxia. The Journal of Physiology, 597(9), 2411-2428.
- 6. Batista D, et al. (2008). Pungent agents from Szechuan peppers excite sensory neurons by inhibiting two-pore potassium channels. Nature Neuroscience, 11, 772-779.
- 7. Rödström, K.E.J., et al. A lower X-gate in TASK channels traps inhibitors within the vestibule. Nature 582, 443–447 (2020).

Some of the work was performed at NYU Langone Health's Cryo-Electron Microscopy Laboratory (RRID: SCR_019202), which is partially supported by the Laura and Isaac Perlmutter Cancer Center Support Grant NIH/NCI P30CA016087

Engineering an off-switch for background TREK1 potassium channels

Elena B. Riel[1†], Louis Goldberg[1†], Paul Riegelhaupt

[1]Department of Anesthesiology, Weill Cornell Medicine, New York, † Authors contributed equally to this work

Abstract

Background TREK1 K2P potassium channels are among the best studied K2P channels and known to modulate cellular excitability. We aim to design TREK1-based molecular tools to control neuronal activity. In this work we used the FKBP (FK506-binding protein) inducible homodimer system to engineer a controlable off-switch for TREK1 channels.

TREK1 strucutre

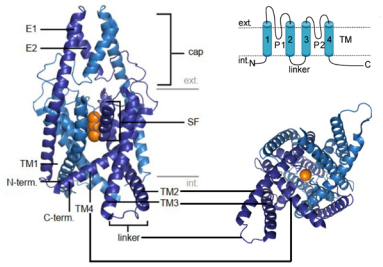

Figure 1 - TREK1 Strucutre & topology model. PDB:EMD-27386, Schmidpeter et al. (2023). TREK1 is a functional dimer with four transmembrane domains (TM) and two pore-loops (P1/P2) in tandem in each subunit. N- & C-terminal domains extend into cytosol. P1 and P2 loop extensions (E1 / E2) project into extracellular site and form a cap structure.

Inducible Homodimer System

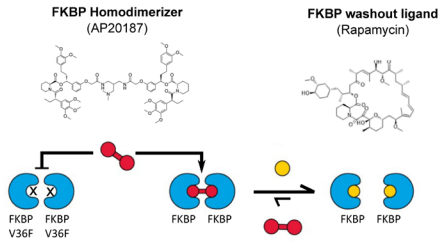

Figure 2 - Inducible Homodimer System. AP20187 is able to bind two FK506-binding proteins (FKBP). Introduction of the V36F mutation reders the FKBP insensitive to AP20187. Dimerization can be reversed by the application of rapamycin that binds FKBP with a higher affinity. Clontech Lanoratories, Inc. A Takara Bio Company iDimerizeTM Inducible system, PT5178-1 (111115) p.12.

Engineering concept and mutant creation

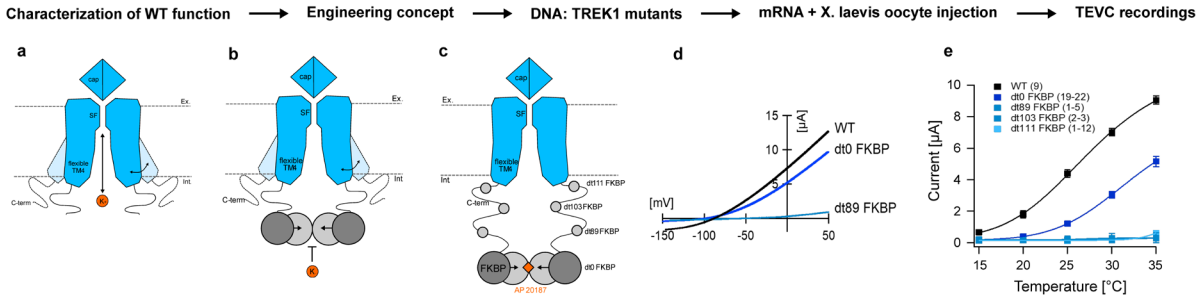

Figure 3 - Engineering workflow, mutant creation and characterization. a. TREK1 WT cartoon indecating a large freely accessible pore and the flexible TM4 of each subunit in tere up- (active) and down (inactive) state. **b.** Engineering concept showing the dislocation of the TM4 helix to the downstate by the introduction of a dimerizable system. **c.** TREK1 mutants with introduced FKBP domain at the C-terminal domain (CTD) of each channel monomer with variing CTD chain length. **d.** Exemplary trace of WT, dt0 FKBP and dt89 FKBP mutants recorded using Two-electrode voltage clamp (*X. laevis*). **e.** Mean current [µA] of WT and mutant channels obtained from recordings as shown in d.

Control experiments

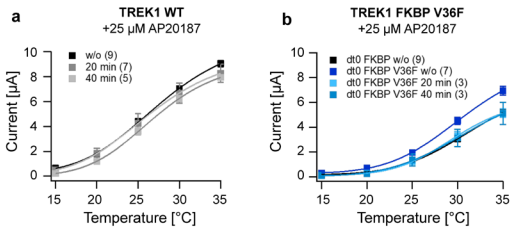

Figure 4 - AP20187 has no effect on WT and control mutant channel dt0 FKBP V36F. a. TREK1 WT temperature dependent activation with and without (black) previous incubation in ND96 solution containing 25 µM AP20187 for 20 min (dark gay) and 40 min (light gray). **b.** FKBP V36F mutants are unable to dimerize upon AP20187 application. V36F mutation was introduced into the TREK1 dt0 FKBP channel and its activity was recorded with and without previous incubation in AP20187 containing solution. Recorings were carried out as shown in Figure 3d.

Dimerization experiment

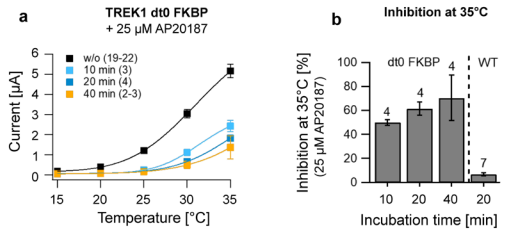

Figure 5 - AP20187 reduces activity of TREK1 dt0 FKBP. a. Mean temperature dependent current of TREK1 dt0FKBP with and without (black) incubation in 25 µM AP20187 containing ND96 solution for 10 (light blue), 20 (blue) and 40 (orange) minutes. **b.** Percentage of current inhibition upon AP20187 at 35°C, normalized to WT currents w/o treatment.

Conclusion

Our results demonstrate a proof of principle that proteine fusions to the C-terminal region of the channel are suitably positioned to modulate channel activity and serves us as a template for the introduction of other inducible systems (i.e. light inducible systems).

Isoflurane alters presynaptic endoplasmic reticulum calcium dynamics in wild-type and malignant hyperthermia-susceptible rodent hippocampal neurons

Weill Cornell Medicine

Vanessa Osman PhD[1], Iris Speigel PhD[2], Kishan Patel[2], and Hugh C Hemmings Jr, MD, PhD[1,2]

Department of Pharmacology[1], Department of Anesthesiology[2], Weill Cornell Medicine, New York, NY

Introduction

Volatile anesthetics

Volatile anesthetics are essential to modern medicine, but despite their widespread clinical use, their cellular and molecular mechanisms of action remain unclear. Pre-synaptically, volatile anesthetics alter synaptic transmission by depressing activity dependent Ca^{2+} influx which decreases neurotransmitter release reducing synaptic vesicle (SV) exocytosis [(1)]. The mechanisms involved in regulating presynaptic Ca^{2+} are unclear.

Endoplasmic Reticulum (ER)

The ER is the largest store of releasable Ca^{2+} [(2)]. Axonal ER Ca^{2+} controls presynaptic Ca^{2+} and SV exocytosis through release and sequestration [(3)].

ER Ca^{2+} Pathways

ER Ca^{2+} efflux: Ryanodine receptors (RyR) and inositol 1,4,5-triphosphate receptors (IP_3R) mediate ER Ca^{2+} release.

ER Ca^{2+} uptake: Sarcoplasmic/endoplasmic reticulum Ca^{2+} ATPase (SERCA) pump pumps Ca^{2+} into the ER.

Malignant Hyperthermia (MH)

MH is a pharmacogenetic disorder that can result from mutations in RyR. It is characterized by a hypermetabolic reaction to volatile anesthetics resulting in hyperthermia, acidosis, and muscle rigidity [(4)]. MH is modeled by a mouse with a T4826I-RYR1 mutation. Dantrolene, a RyR antagonist, is effective in treating MH [(5)].

Methods

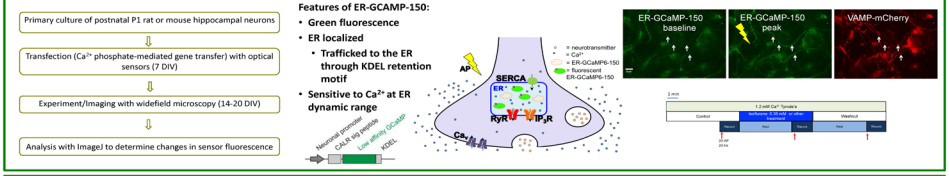

Rat

Isoflurane reduces baseline and stimulation-evoked ER Ca^{2+} concentration

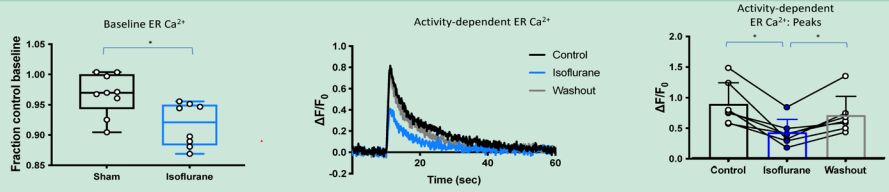

Mouse

T4826I-RYR1 (MH susceptibility) mutation enhances isoflurane inhibition of activity-dependent ER Ca^{2+} increase, activity-dependent presynaptic cytosolic Ca^{2+} increase, and SV exocytosis

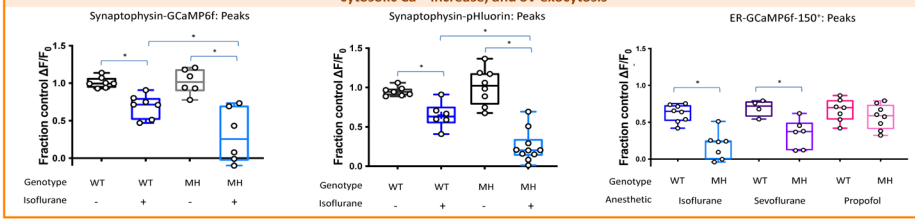

Conclusions

- Isoflurane depresses ER Ca^{2+} levels at baseline
- Isoflurane inhibits peak ER Ca^{2+} during electrical stimulation
- The T4826I-RYR1 MH mutation enhances inhibition by isoflurane of presynaptic synaptic vesicle exocytosis, presynaptic cytosolic Ca^{2+}, and ER Ca^{2+}
- In T4826I-RYR1 mutant mice, inhibition of ER Ca^{2+} by the volatile anesthetic sevoflurane, but not by the IV anesthetic propofol, is also enhanced

References

1. Baumgart JP, Zhou ZY, Hara M, Cook DC, Hoppa MB, Ryan TA, Hemmings HC Jr. Isoflurane inhibits synaptic vesicle exocytosis through reduced Ca^{2+} influx, not Ca^{2+}-exocytosis coupling. Proc Natl Acad Sci U S A. 2015 Sep 22;112(38):11959-64.
2. Ashby MC, Tepikin AV. ER calcium and the functions of intracellular organelles. Semin Cell Dev Biol. 2001 Feb;12(1):11-7.
3. de Juan-Sanz J, Holt GT, Schreiter ER, de Juan F, Kim DS, Ryan TA. Axonal Endoplasmic Reticulum Ca^{2+} Content Controls Release Probability in CNS Nerve Terminals. Neuron. 2017 Feb 22;93(4):867-881.e6.
4. Rosenberg H, Pollock N, Schiemann A, Bulger T, Stowell K. Malignant hyperthermia: a review. Orphanet J Rare Dis. 2015 Aug 4;10:93.
5. Cannon SC. Mind the magnesium, in dantrolene suppression of malignant hyperthermia. Proc Natl Acad Sci U S A. 2017 May 2;114(18):4576-4578.

Funding

NIH R01 GM058055 (HCH)

NIH F31 GM133115-03 (VO)

Propofol restores HCN1 epilepsy mutants and reveals non-canonical voltage-dependent gating in HCN channels

Elizabeth D. Kim[1]*, Xiaoan Wu[2]*, Sangyun Lee[1], Gareth R. Tibbs[1], Kevin P. Cunningham[2], Marta E. Perez[2], Peter A. Goldstein[1], Alessio Accardi[1], H. Peter Larsson[2], and Crina M. Nimigean[1]
[1]Dept of Anesthesiology, Weill Cornell Medical College, New York, NY 10065 | [2]Dept of Physiology and Biophysics, University of Miami Miller School of Medicine, Miami, FL 33136 | * equal contribution

ABSTRACT

Hyperpolarization-activated cyclic nucleotide-gated (HCN) ion channels are membrane proteins essential for pacemaking activity and neural signaling. Drugs inhibiting HCN1 are promising candidates for targeting and treating neuropathic pain and epileptic seizures. To date, clinical ion channel pharmacology predominantly revolves around inhibition via pore blockers. Pore blockers are often non-specific and consequently generate unwanted side effects. In contrast, allosteric drugs do not target the pore and have the potential to achieve greater selectivity. Propofol (2,6-di-*iso*-propylphenol) is a known HCN1 small molecule allosteric inhibitor but the structural basis of its action has yet to be defined. Here, using single particle cryo-EM and electrophysiology, we show that propofol inhibits HCN1 channels by binding, in a state-dependent manner, to a mechanistic "hotspot" that lies in a groove between the S5 and S6 transmembrane helices. Two human HCN1 channel polymorphisms - D401H in S6 and M305L in S5 in this groove - associated with early infantile epileptic encephalopathy (EIEE) act by destabilizing HCN1 closed states. We found that propofol restored voltage-dependent closing in these mutants. To understand the mechanism of propofol, we tracked voltage sensor movement in spHCN channels and found that propofol inhibition is independent of voltage sensor conformational changes. Mutations at the homologous methionine in spHCN and at a nearby conserved phenylalanine in S6 in this groove, similarly, destabilize closing without disrupting voltage sensor movements. We propose a model for voltage-dependent gating in HCN channels in which propofol allosterically inhibits the channels by stabilizing closed-state interactions between S5 and S6, which we show to be central to the non-canonical coupling between the voltage sensor and gate in HCN channels. Our findings open the way to exploit this site to design novel, specific drugs targeting HCN-channelopathies.

INTRODUCTION

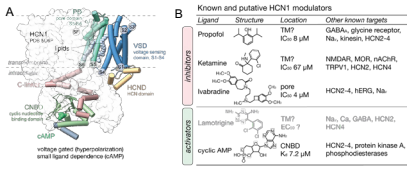

Fig 1. *A)* HCN1 channel architecture consists of 5 main components (highlighted in different colors). Modulation of ion channel activity by small molecules occurs through multiple sites. Many toxins and blockers produce their effect by blocking the pore. Ligands, such as cyclic nucleotides, can activate channels. Other small molecules bind in the transmembrane domain within a protomer or in between protomer subunits. *B)* Summary of HCN1 channel interactors, their location of binding, and other protein targets. The majority of HCN1 inhibitor compounds are unspecific and target the pore. However, propofol exhibits slight specificity towards HCN1 than other HCN isoforms (HCN2-4).

CONCLUSIONS

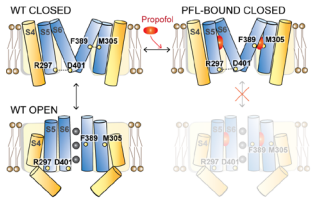

We identified a HCN1-propofol binding site that is a state-dependent pocket

Propofol-like drugs can potentially be used to repair disease-associated HCN channels with weak or no voltage sensitivity

A Met-Phe interaction that couples the VSD and pore is strengthened by propofol

RESULTS

CryoEM densities of candidate propofol-HCN1 binding sites were determined

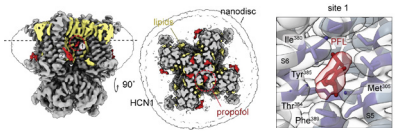

Fig 2. Density maps of HCN1 in the presence of propofol. Highlighted in yellow are visible lipid densities surrounding HCN1 (grey). For clarity, the top view (left) is cross sectioned at the dashed line shown in the side view (right). The red dashed circles are the locations of the putative propofol (red) sites. On the right, zoomed in view of binding site 1.

Site 1 appears to be state-dependent binding pocket

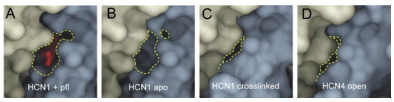

Fig 3. Shown are space filled models of *A)* HCN1 + propofol (PFL), *B)* HCN1 closed (PDB 5U6O [1]), *C)* HCN1 closed with the voltage sensor crosslinked in a hyperpolarized conformation (PDB 6UQF, [2]), and *D)* HCN4 in the open state (PDB 7NMN, [3]). Adjacent subunits are colored in blue and yellow and propofol in red. The propofol binding pocket (dashed yellow lines) in the closed states (panels *A* and *B*) is no longer present in the HCN1 crosslinked or HCN4 open state (panels *C* and *D*).

Site 2 is non-specific for propofol binding

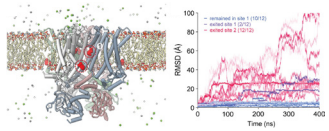

Fig 4. Shown is an overview of the molecular dynamics simulation system. HCN1 was solvated in POPC lipids (yellow) and propofol (red) molecules bound at site 1 and site 2 are shown in spheres. K+ and Cl- ions are shown in green and gray spheres. Plotted is the RMSD of propofol from their originating positions. All 12 propofols unbound from site 2.

Mutation of site 1 residues resulted in reduced druggability

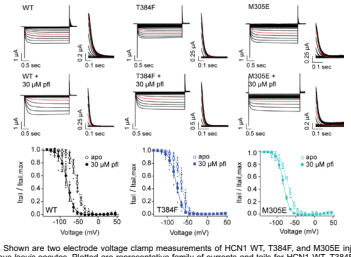

Fig 5. Shown are two electrode voltage clamp measurements of HCN1 WT, T384F, and M305E injected *Xenopus laevis* oocytes. Plotted are representative family of currents and tails for HCN1 WT, T384F, and M305E in the absence and presence of propofol. Voltage clamp ranged from +45 mV to -125 mV with a tail potential measured at +50 mV. Current response at -85 mV is highlighted in red. For WT (n ≥ 21), T384F (n ≥ 11), and M305E (n ≥ 3) replicates were recorded after a 20 min incubation with carrier DMSO or 30 uM propofol. Tail currents were fitted with a Boltzmann equation in the absence (open, dashed) and presence (filled, solid) of propofol.

Propofol restores function of disease-causing HCN1 mutants

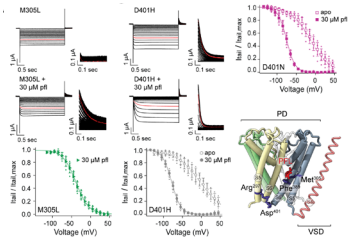

Fig 6. Shown are two electrode voltage clamp measurements of HCN1 M305L and D401H in the absence and presence of propofol. Voltage clamp ranged from +45 mV to -125 mV with tail currents measured at +50 mV. The current response at -85 mV is highlighted in red. Tail currents were fitted with a Boltzmann equation for M305L (n = 6), D401H (n ≥ 11), and D401N (n ≥ 11). On the bottom right, a schematic of the intraprotomer S5-S6 helix Met-Phe interaction and bundle crossing interprotomer S5-S6 helix Arg-Asp salt-bridge interaction with respect to the propofol binding site (red). Individual subunits within the PD are highlighted (green, yellow, white, blue) and the S4 helix of the VSD is in red-brown.

Propofol inhibits current without changing voltage sensor movement

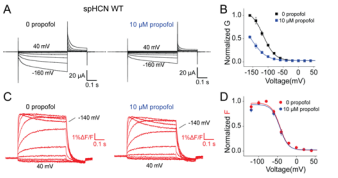

Fig 7. *A)* Representative current traces from spHCN WT channels from the same oocyte before and after the application of 10 µM propofol. Dashed lines indicate no currents. *B)* GV relations from spHCN channels before (black) and after (blue) the application of 10 µM propofol. The conductance at -160 mV was reduced by 46 ± 2 % (n=3). *C)* Representative fluorescence traces from spHCN WT channels from the same oocyte before and after the application of 10 µM propofol. The amplitude of the fluorescence signal was slightly reduced after the application of propofol due to the photobleaching and/or internalization of labeled channels. *D)* FV relations from spHCN channels before (red) and after (blue) the application of 10 µM propofol.

Met-aromatic interactions couple the PD to VSD in voltage-gated HCN1 channels

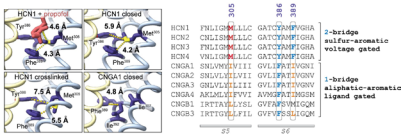

Fig 8. Local structure of HCN1 [1-3] and CNGA1 [4] around the Met^{305}–Phe^{389} interaction. Approximate distances between atoms (dashed yellow lines) are labeled between methionine, isoleucine, and the adjacent aromatic rings (purple). Propofol is colored in pink and adjacent protomers are in blue and yellow. On the right, a multiple sequence alignment between human HCN and CNG isoforms. Residue numbering follows the HCN1 amino acid sequence. A single aliphatic-aromatic interaction (1-bridge) exists in CNG channels which are ligand gated. In contrast, an interaction between methionine with two aromatic residues (2-bridge) occurs in HCN channels which are voltage gated.

REFERENCES

[1] Lee, Cell 2017; [2] Lee, Cell 2019; [3] Saponaro, Mol Cell 2021; [4] Xue, Neuron 2021

We thank Maria Falzone and Philipp Schmidpeter for assistance with cryoEM freezing and processing, Matthew Ferrer for help with two electrode voltage clamp recordings, the New York Structural Biology Center and New York University Langone Health for cryoEM screening and data collection, and the members of the Nimigean and Riegelhaupt labs for their scientific input. We gratefully acknowledge Roderick Mackinnon for the pEG BacMam-HCN1em and PET32a-eGFP nanobody constructs.
This work is supported by the National Institutes of Health F32GM145091 (EDK), the Hartwell Foundation (EDK), and National Institutes of Health GM124451 (CMN), National Institutes of Health GM139164 (HPL), National Institutes of Health GM128420 (AA), and National Institutes of Health R42NS129370 (PAG)

Calcium-gated potassium channel blockade via membrane-facing fenestrations

Chen Fan[1], Emelie Flood[#2], Nattakan Sukomon[#1], Shubhangi Agarwal[1], Toby W. Allen[*2], Crina M. Nimigean[*1,3]

1 Department of Anesthesiology, Weill Cornell Medicine, New York, USA. 2 School of Science, RMIT University, Melbourne, Australia 3 Departments of Physiology and Biophysics, Weill Cornell Medicine, New York, USA
# Indicates the authors that contributed equally to the manuscript *Indicates corresponding authors
Chen Fan's current address: Science for Life Laboratory, Department of Biochemistry and Biophysics, Stockholm University, Solna, Sweden. **Emelie Flood's current address:** Schrödinger, Inc., 1540 Broadway, 24th floor, New York, NY 10036, USA

Abstract-

Blocker molecules have been traditionally used as probes to investigate the pore structure and the gate locations in ion channels. Specifically, quaternary ammonium (QA) compounds can bind in the large pore cavity to block not only the open but also closed conformations of large conductance calcium-activated potassium channels. This has been interpreted to mean that blockers can access the pore through the intracellular bundle-crossing constriction in the closed state. However, structures of calcium-free closed MthK, a *Methanobacterium thermoautotrophicum* homolog of eukaryotic large conductance calcium-activated K (BK) channels, revealed a tightly-constricted and apparently impermeable intracellular bundle-crossing. Here, we investigated how intracellular blocker molecules (TPeA) access the closed MthK pore. We solved structures of closed MthK with bound QAs, and a high-resolution structure of closed wt MthK without blockers using single-particle cryo-EM. These structures reveal the presence of lipids bound in and near membrane-facing fenestrations that appear between adjacent subunits in the closed channel. This pathway was experimentally validated by showing that a mutant channel with narrower fenestrations in the closed conformation, expected to impede TPeA access, displayed no closed-state block in the same TPeA concentration range shown to block the WT channel. The high degree of structure and sequence conservation in this region between BK and MthK channels suggest that these fenestrations play similar roles in both channels. Thus, the membrane fenestrations represent a non-canonical pathway for selective targeting of specific channel conformations, opening novel ways to selectively drug the large conductance calcium-activated potassium channel family.

Introduction

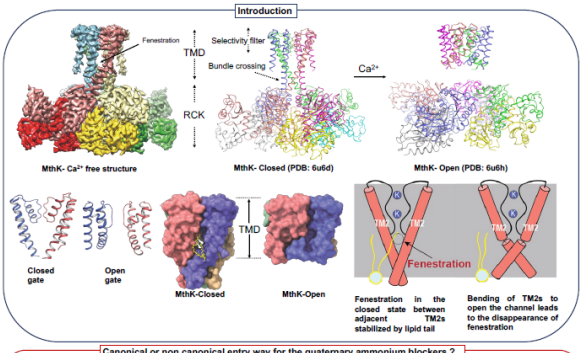

Canonical or non canonical entry way for the quaternary ammonium blockers ?

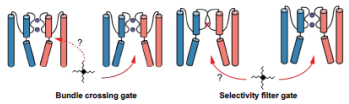

Result 1 - Wt MthK- bound to TpeA in closed state beneath the selectivity filter

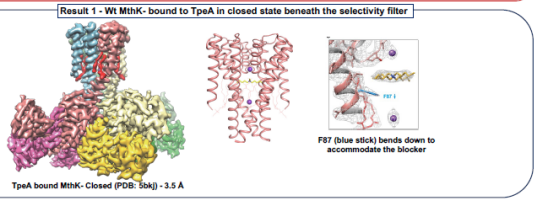

Mutations designed to change the size and hydrophobicity of fenestrations

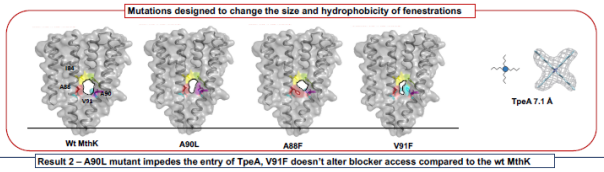

Result 2 – A90L mutant impedes the entry of TpeA, V91F doesn't alter blocker access compared to the wt MthK

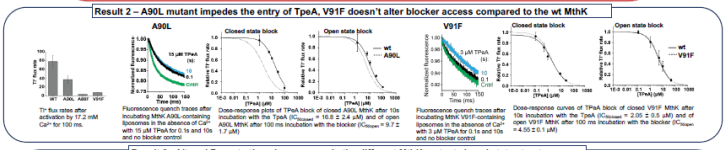

Result 3 - Altered Fenestration sizes as seen in the different MthK mutant closed state structures

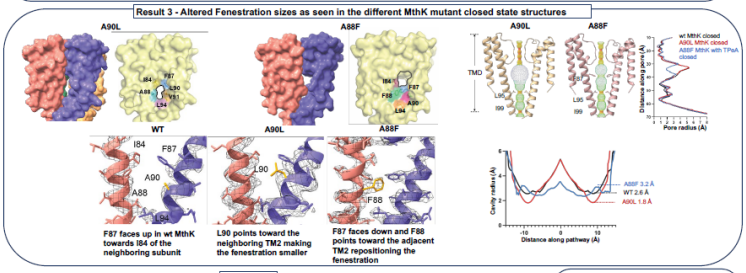

Conclusion

- TPeA entry is impeded through the narrower fenestrations of closed A90L MthK.
- QA blockers can enter and block the closed pore of MthK channels via a non-canonical membrane-facing fenestration path, despite the closed intracellular gate.
- This novel access pathway into the pore of calcium-gated potassium channels opens up possibilities to design much needed specific state-dependent drugs targeting these therapeutically relevant ion channels.

Acknowledgements:
We thank L. Yan, M. Kopylov and E. Eng for their support during and data collection at the Simons Electron Microscopy Center and National Resource for Automated Molecular Microscopy located at the New York Structural Biology Center, supported by grants from the Simons Foundation (SF349247), NYSTAR, and the NIH National Institute of General Medical Sciences (GM103310). W. Rice and B. Wang for data collection at NYU Langone Health's Cryo-Electron Microscopy Laboratory (RRID: SCR_019202). The work presented here was sponsored in part by the NIH GM080352 to CN.

Reference:
Fan, C. *et al.* Ball-and-chain inactivation in a calcium-gated potassium channel, *Nature* **580**, 288-291, doi:10.1038/s41586-020-2114-0 (2020).

HS-AFM Single-Molecule Structural Biology Uncovers Basis of Transporter Wanderlust Kinetics

Yining Jiang,[1,2] Simon Scheuring[2,3,4]

[1] Biochemistry & Structural Biology, Cell & Developmental Biology, and Molecular Biology (BCMB) Program, Weill Cornell Graduate School of Biomedical Sciences, 1300 York Avenue, New York, NY-10065, USA.
[2] Weill Cornell Medicine, Department of Anesthesiology, 1300 York Avenue, New York, NY-10065, USA.
[3] Weill Cornell Medicine, Department of Physiology and Biophysics, 1300 York Avenue, New York, NY-10065, USA.
[4] Kavli Institute at Cornell for Nanoscale Science, Cornell University, Ithaca, New York 14853, USA.

Abstract

As atomic structures of membrane proteins are readily resolved and predicted, there emerges an urgent need to investigate the real-time structural dynamics at the single molecule level to obtain novel insights into membrane structural biology. Here, we present a high-speed atomic force microscopy (HS-AFM) based method to isolate and immobilize individual membrane proteins in an extended lipid bilayer, while preserving their structural dynamics. Using Glt_{Ph}, a trimeric aspartate transporter, as a model protein, we demonstrate that HS-AFM combined with the presented strategy was able to track structural dynamics of individual protomers at sub-second temporal resolution and sub-nanometer spatial resolution for tens of seconds. We developed a principal component analysis (PCA) based method to sort protomers at each time point into different conformations according to their structural features, reconstructing a structure-time trace for each protomer of a single molecule. Using the previously developed localization AFM (LAFM) method, we calculate Angstrom-resolution Glt_{Ph} surface structures of single molecules as it transits through several conformational states in the transport cycle. Our work enables direct observation and analysis of the structure and dynamics of individual unlabeled membrane proteins, unlocking the potential of HS-AFM in the study of single-molecule structural biology.

Backgrounds

- **The PDB structures of major Glt_{Ph} conformations**

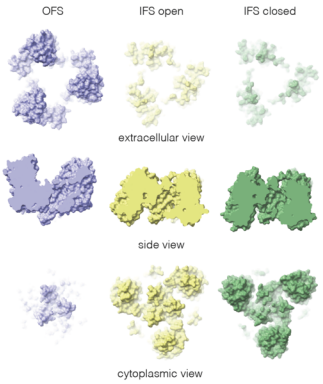

- **High-speed atomic force microscopy**

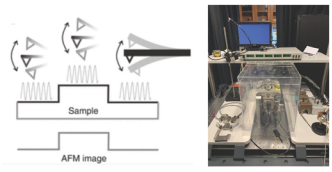

Results

- **Tracking individual membrane transporters with high-resolution and stability**

1. The dense packing of Glt_{Ph}

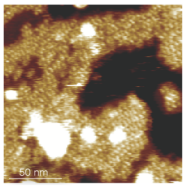

2. Immobilized Glt_{Ph} in an extended lipid bilayer

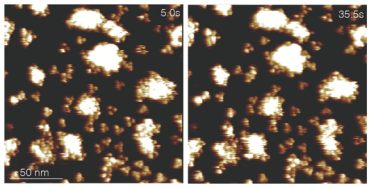

3. Isolated individual Glt_{Ph} molecules

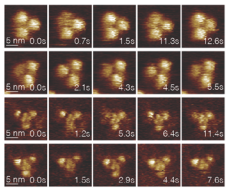

- **Sorting promoter observations into different conformations**

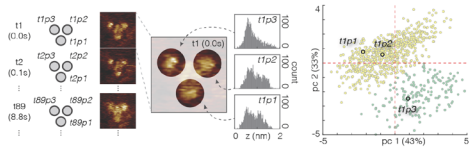

- **LAFM maps of the three maior GltPh conformations**

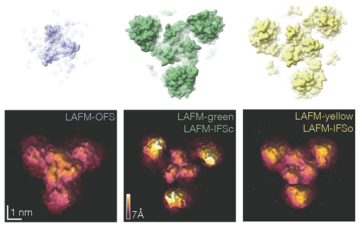

- **Three-state conformation dynamics of individual Glt_{Ph} promoters**

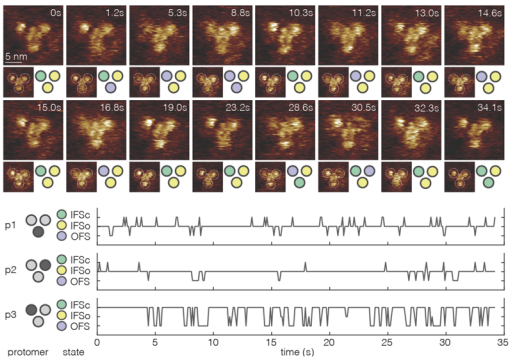

Acknowledgement

Funding: Work in the Scheuring laboratory was supported by grants from the National Institute of Health (NIH), National Center for Complementary and Integrative Health (NCCIH), DP1AT010874 and National Institute of Neurological Disorders and Stroke (NINDS), R01NS110790, and by the Kavli Institute at Cornell.

Author contributions: Y.J. and S.S. designed the study; Y.J. performed all HS-AFM experiments; Y.J. and S.S. performed HS-AFM image processing and data analysis; Y.J. and S.S. wrote the manuscript.

Wang & Boudker, *eLife*, 2020
Matin et al., *Nat Commun*, 2020
Ruan et al., *PNAS*, 2017
Akyuz et al., *Nature*, 2013
Jiang et al., in revision

Synaptic metabolic vulnerability is cell- and phenotype-specific in hippocampal neurons from rats

Daniel Cook[1], MD, Kirsten Bredvik[2], BS, Timothy Ryan[1,2], PhD
Department of Anesthesiology[1] and Biochemistry[2], Weill Cornell Medicine, New York, NY

Weill Cornell Medicine
Anesthesiology

INTRODUCTION

The human central nervous system (CNS) has a high metabolic demand, consuming 20% of the body's oxygen despite constituting only 2% of body mass.[1] Interruptions in the supply of fuel to the brain impair CNS function within minutes and may lead to permanent dysfunction. The release of chemical neurotransmitters from nerve terminals during synaptic vesicle recycling is a substantial metabolic load to neurons, and impaired synaptic metabolism causes arrest of vesicle endocytosis.[2] However, the determinants of metabolic vulnerability of neurons and individual nerve terminals are not well understood. Here, we used a genetically-encoded, fluorescent biosensor of synaptic vesicle recycling, synaptophysin-pHluorin (sy-pH), expressed in excitatory and inhibitory neurons in dissociated hippocampal cultures to compare the ability of individual nerve terminals to sustain synaptic vesicle recycling during fuel deprivation. We demonstrate that the metabolic vulnerability of neurons is both cell- and phenotype-specific and not fully explained by the metabolic load of synaptic vesicle recycling.

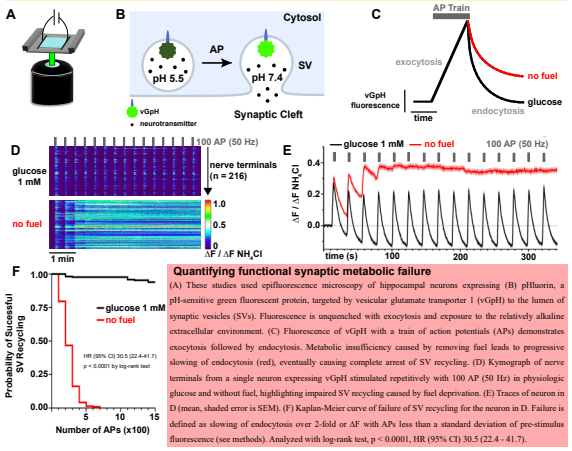

Quantifying functional synaptic metabolic failure

(A) These studies used epifluorescence microscopy of hippocampal neurons expressing (B) pHluorin, a pH-sensitive green fluorescent protein, targeted by vesicular glutamate transporter 1 (vGpH) to the lumen of synaptic vesicles (SVs). Fluorescence is unquenched with exocytosis and exposure to the relatively alkaline extracellular environment. (C) Fluorescence of vGpH with a train of action potentials (APs) demonstrates exocytosis followed by endocytosis. Metabolic insufficiency caused by removing fuel leads to progressive slowing of endocytosis (red), eventually causing complete arrest of SV recycling. (D) Kymograph of nerve terminals from a single neuron expressing vGpH stimulated repetitively with 100 AP (50 Hz) in physiologic glucose and without fuel, highlighting impaired SV recycling caused by fuel deprivation. (E) Traces of neuron in D (mean, shaded error is SEM). (F) Kaplan-Meier curve of failure of SV recycling for the neuron in D. Failure is defined as slowing of endocytosis over 2-fold or ΔF with APs less than a standard deviation of pre-stimulus fluorescence (see methods). Analyzed with log-rank test, p < 0.0001, HR (95% CI) 30.5 (22.4 - 41.7).

Methods

Cell Culture

Protocols were approved by Weill Cornell Medicine IACUC. Dissociated hippocampal neurons from postnatal day 0-2 Sprague-Dawley rats of both sexes were plated on coverslips. Transfection occurred on day in vitro (DIV) 6-8 with sy-pH under either CaM kinase II (CaMKII) or DLX promoter to drive expression in glutamatergic or GABAergic neurons, respectively. Experiments were performed on DIV 14-21.

Live-Cell Imaging

Images were acquired with a laser-illuminated epifluorescence microscope and Andor iXon+ EMCCD. Coverslips were loaded onto a custom chamber, maintained at 37°C, and perfused with Tyrode's solution buffered with HEPES to pH 7.4 and containing glucose 1 mM or no glucose. Action potentials (APs) were elicited with 1 ms field depolarizations to generate 100 APs in 2 s every 22 s. At the end of experiments, Tyrode's solution with equimolar replacement of NaCl with NH_4Cl was perfused to alkalinize intracellular sy-pH to normalize ΔF to the total releasable pool of vesicles.

Analysis

ImageJ was used to calculate fluorescence with local background subtraction. To facilitate robust single nerve terminal analysis, terminals were excluded if ΔF was less than 3 standard deviations (SDs) of the pre-stimulus baseline ($\sigma_{F_{pre-stim}}$) or if ΔF with NH_4Cl was less than 5 $\sigma_{F_{pre-stim}}$. The criteria to define arrest of synaptic vesicle recycling are 1) 2 sequential AP responses in which recovery of fluorescence is less than half the recovery of the initial stimulus or ΔF less than 0pre-stim and 2) over half of subsequent stimuli must meet either of these criteria. Statistical analysis was performed with Prism v9 with significance defined as $p < 0.05$.

Acknowledgements

This work is supported by the National Institutes of Health (NS036942 and NS11739 awarded to TAR; K08GM148935 to DCC), the Foundation for Anesthesia Education and Research (MRTG-02-15-2020-Cook awarded to DCC), and the Burroughs Wellcome Weill Cornell Physician Scientist Academy (DCC).

References:

1. Mink JW et al. Am J Physiol 1981; 241(3): 203-12.
2. Rangaraju V et al. Cell 2014; 156(4), 825-35.

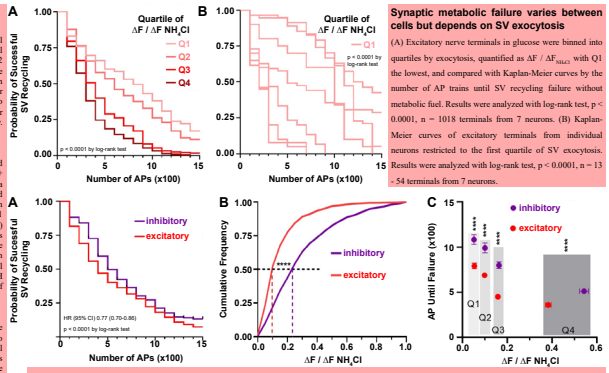

Synaptic metabolic failure varies between cells but depends on SV exocytosis

(A) Excitatory nerve terminals in glucose were binned into quartiles by exocytosis, quantified as ΔF / ΔF_{NH4Cl} with Q1 the lowest, and compared with Kaplan-Meier curves by the number of AP trains until SV recycling failure without metabolic fuel. Results were analyzed with log-rank test, p < 0.0001, n = 1018 terminals from 7 neurons. (B) Kaplan-Meier curves of excitatory terminals from individual neurons restricted to the first quartile of SV exocytosis. Results were analyzed with log-rank test, p < 0.0001, n = 13 - 54 terminals from 7 neurons.

Inhibitory neurons exhibit greater metabolic endurance compared to excitatory neurons despite increased SV recycling imposing a higher metabolic load

(A) Nerve terminals of excitatory and inhibitory neurons were compared with Kaplan-Meier curves by the number of AP trains until SV recycling failure. Results were analyzed by log-rank test, p < 0.0001, HR (95% CI) 0.77 (0.70 - 086). (B) Because SV recycling is a major metabolic load on neurons, differences in SV release between neuronal phenotypes may impact their apparent metabolic resilience. Thus, SV exocytosis in glucose was compared between excitatory and inhibitory neurons with cumulative frequency plots, revealing that inhibitory neurons have increased SV exocytosis. Results were analyzed with Mann-Whitney test, **** p < 0.0001. (C) Excitatory and inhibitory nerve terminals were binned according to the quartiles used previously for excitatory neurons. Terminals of excitatory and inhibitory neurons were compared within quartiles by the number of AP trains until SV recycling failure. Dots are mean, error bars are standard deviation. Data were analyzed with unpaired t-test and Bonferroni-Dunn correction for multiple comparisons. **** p < 0.0001, For A-C, n = 1012 and 878 from 7 and 6 excitatory and inhibitory neurons, respectively.

CONCLUSIONS

We demonstrate that SV exocytosis is a determinant of metabolic vulnerability. However, terminals with similar SV release differ between neurons in their ability to sustain synaptic vesicle recycling during fuel deprivation. Moreover, inhibitory neurons are more metabolically resilient to fuel deprivation compared to excitatory neurons. These results support that the metabolic vulnerability of neurons is both cell- and phenotype-specific and not fully explained by the metabolic load of synaptic vesicle recycling. Future studies will address the biochemical differences causing greater metabolic endurance of inhibitory neurons.

Blast injury induces sex-dependent changes in structural connectivity along nociceptive fiber tracts

Weill Cornell Medicine
Amanda Simon[1], Keith Jamison[1], Iryna Popovych[2], Amy Kuceyeski[1] and Paola Calderon[1]
[1] Weill Cornell Graduate School, New York, NY [2]Weill Cornell Medicine, NYC, NY

Introduction

- Traumatic Brain Injury (TBI) is a leading cause of death and disability in the United States. Very little attention has been devoted to understanding the neurological mechanism of TBI-induced pain and its role in motor rehabilitation despite both being common after trauma
- Our mouse model of Secondary Blast Injury (SBI) demonstrated divergent motor recovery outcomes on the rotarod independent of cognitive performance (A). Damage along lateral parabrachial nucleus (PBNL)-mediated nociceptive pathways – not motor pathways - correlated with rotarod performance (B,C)[1]

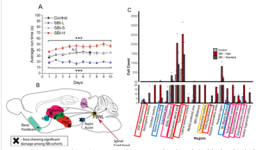

  - Later experiments revealed increased pain-related behavior in low-performing SBI mice
- **Goal: To use a multipronged approach to uncover the structural and functional neuroanatomical correlates of divergent post-SBI recovery outcomes**

Hypothesis

TBI induces adverse changes in nociceptive fiber tracts leading to disparate motor performance

Methods

- **Diffusion Tensor Imaging (DTI):** Diffusion data collected from perfused brain specimens from control and SBI mice 3-4 weeks post-injury (Female N=16 (8 control, 8 SBI); Male N=20 (8 control, 12 SBI)), preprocessed using the FSL neuroimaging library and aligned to the Waxholm Space (WHS) Atlas of the C57BL/6 mouse brain to generate fractional anisotropy (FA) maps for each specimen. ROI masks generated to measure mean FA across the brain for each specimen.
- **Probabilistic Tractography:** MRTrix3 toolbox generated probability distribution functions on the principal fiber direction at each voxel in the PBN for each specimen. With PBN as a seed region, we measured streamline count, volume and density between it and target efferents. For all tests, we used Shapiro-Wilks test to confirm parametricity, then conducted two-tailed tests to compare groups and determined which SBI group drove the results.
- **Myelin Basic Protein (MBP) Immunofluorescence:** After DTI, subset of samples were stained for anti-MBP with a secondary stain of Alexa Fluor 555. Samples were imaged at MSK and assessed for immunofluorescence using ImageJ
- **Chemogenetic Manipulation + Rotarod:** Injected Vglut+ mice with Cre-inducible hm4D(Gi/Gq) Designer Receptors Exclusively Activated by Designer Drugs (DREADDs) bilaterally into the PBN. After two weeks, mice were implanted with an intracranial cannula into cerebellar lobule III (Cbl3) and after recovering were assessed for motor performance on the rotarod before and after CNO administration

Results

Figure 1: Mean FA Analysis revealed sex-dependent maladaptive changes driven by standard and low performers

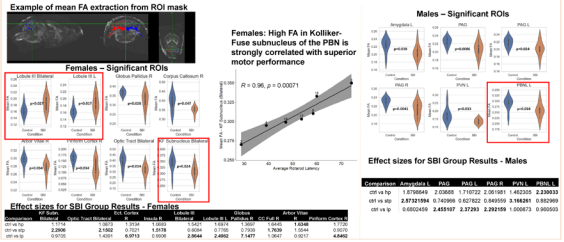

Figure 2: Probabilistic Tractography reveals unilateral increase in myelination driven primarily by standard and low performers observed in both male and female SBI cohorts along PBN-Cbl3 Pathway in females

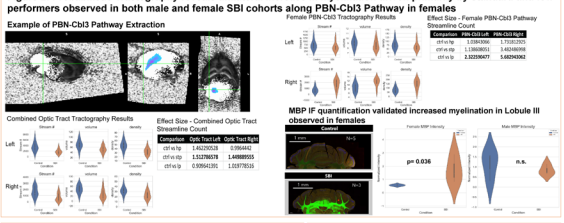

Figure 3: Probabilistic Tractography reveals that SBI males exhibit decreased myelination of left PBN-Cbl3 pathway in high performers

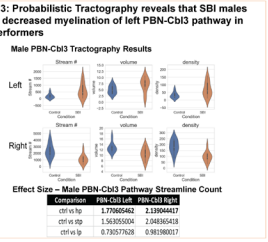

Effect Size – Male PBN-Cbl3 Pathway Streamline Count

Comparison	PBN-Cbl3 Left	PBN-Cbl3 Right
ctrl vs hp	1.770605462	2.139044417
ctrl vs stp	1.563055004	2.048365418
ctrl vs lp	0.730577628	0.981980017

Figure 4: PBNL projects to Lobule III

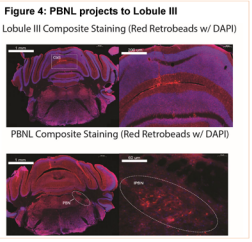

Figure 5: Confocal Microscopy reveals staining in Cbl (1,3) end terminals and granule cell rosettes (2) upon AAV injection of hM4D(Gi)-mCherry

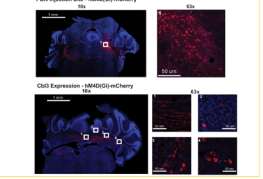

Figure 6: Silencing PBN end terminals in Cbl3 significantly improved motor performance

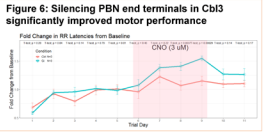

Conclusions

- SBI model shows damage to a similar profile of neural substrates as observed in human patients, thus validating it as an effective means of studying post-SBI sequelae. Findings also support sex-dependent outcomes in brain injury reported in literature
- Despite the sex-dependent changes observed, both male and female SBI groups exhibit maladaptive changes along the PBN-Cbl3 pathway that correspond to motor performance:
  - Males: decreased myelination of left PBN-Cbl3 pathway in high performers improves motor performance by reducing nociceptive signaling
  - Females: damage to the GABAergic Kolliker-Fuse nucleus (part of PBN) combined with increased myelination of right PBN-Cbl3 pathway in low performers leads to disinhibition of excitatory nociceptive relay and poor motor performance

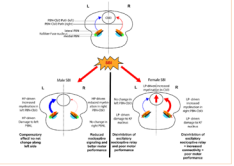

References

1. Gamboa, J., Horvath, J., Simon, A., Islam, M. S., Gao, S., Perk, D., ... & Calderon, D. P. (2021). Secondary-blast injury in rodents produces cognitive sequelae and distinct motor recovery trajectories. *Brain research*, *1755*, 147275-147275.

Structural basis of pH-dependent activation in CLC transporters

Eva Fortea[1], Sangyun Lee[1], Rahul Chadda[2], Janice L. Robertson[2], Olga Boudker[1] and Alessio Accardi[1]

1 Department of Physiology and Biophysics, Weill Cornell Medical School, United States

2 Department of Biochemistry and Molecular Biophysics, Washington University School of Medicine, United States

Introduction

- Activity of dimeric **CLC** Cl^- **channels** and Cl^-/H^+ **transporters** is controlled by the **common gate mechanism:** when the gate is closed both protomers are silenced and they become independently active when it opens.
- Mutations affecting common gating in human CLCs cause several **genetic diseases**. (e.g. myotonia (CLC-1), Dent's disease (CLC-5), osteopetrosis (CLC-7))
- In **Cryo-EM**, we found that under activating conditions (**low pH**), the cytosolic helix A's (αA) of the bacterial **CLC-ec1 Cl^-/H^+ transporter** disengage from the sister protomers, leading to **opening of the H^+ pathways in both protomers**.
- **Cys based crosslinks** aimed at preventing disengagement of αA reversibly inhibit Cl^- flux, indicating opening of the H^+ pathway is required for activation.
- **Single-molecule fluorescence microscopy (smFRET)** shows that opening of the H^+ pathway occurs over seconds, indicating it is a slow activation mechanism.
- **Molecular dynamics (MD) simulations** show that the rearrangement allows water structure which mediates H^+ transport and facilitates Cl^- pore opening.
- Mutations at disease-causing sites favor active CLC-ec1 conformations and also **accelerate common gate opening in human CLC-7** transporter.
- Common gate activation in CLC transporters entails the cooperative opening and hydration of the H^+ pathways, which allow dynamic openings of the Cl^- pores.

Cryo-EM reveals pH and Cl^- dependent conformational rearrangements at the dimer interface of CLC-ec1

- In **Swap (SW),** the N-terminal α-helices (αA) interacts with αRs and H-I loops of the sister protomer and **occlude** the intracellular access of the **H^+ pathway**.
- In **Turn (TN)**, found at low pH, the αAs disengages from the sister protomer, **opening** the intracellular **H^+ pathway**.
- In **Twist (TW),** found at low pH and high Cl^-, with the **H^+ pathway open**, each protomer undergoes rigid body translational movement on the dimer interface.

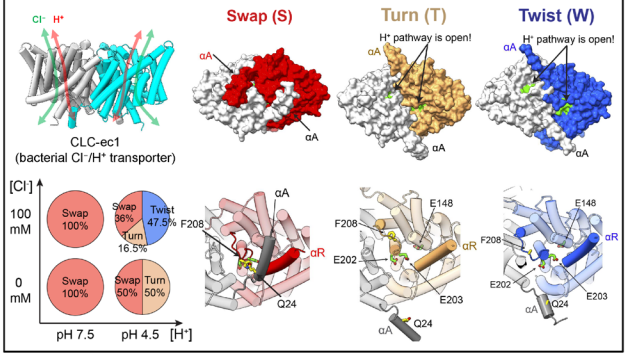

Crosslinking the dimer interface shows that disengagement of αA from αR is required for function

- **L25C/A450C** (crosslinked between αA and αR, named as **Bottom** crosslink) adopts Swap-like (~80%) and Twist (~20%) in cryoEM at low pH and high Cl^-. Chloride efflux mediated by the L25C/A450C mutant is only **~20% of WT**, and with TCEP rescues activity to ~50% of WT.
- **R230C/L249C** (crosslinked between αI and αJ, named as **Top** crosslink) adopts Swap (~66%) and Turn (~33%) and is nearly fully functional as WT, indicating Twist is dispensable for function.

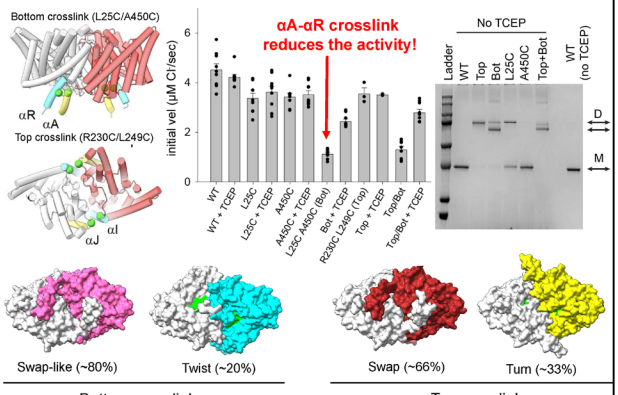

smFRET shows that αA movement is too slow for transport

- αA movement occurs in ~seconds, which is 2~3 orders of magnitude slower than the turn-over rate of transport of CLC-ec1, ~0.5 ms.
- Lowering pH stabilizes low FRET state (with αA disengaged), consistent with cryo-EM resolved in the detergent micelle.

We propose opening of the H^+ pathway is a gating mechanism of CLC-ec1

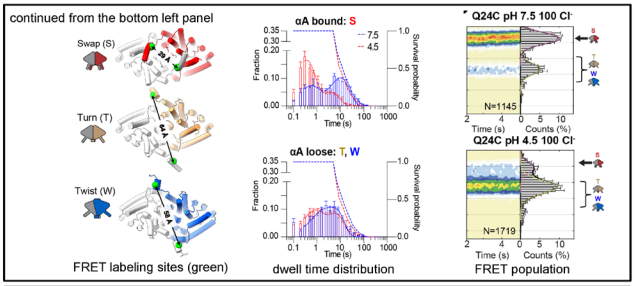

MD simulations show that opening of H^+ pathway allows hydration of the H^+ pathway and opening of the external Cl^- gate

In Turn and Twist (with αA disengaged) the H^+ pathway is **hydrated**, showing frequent formation of **short water wires** which facilitate H^+ transport, and increased **open** probability of the external **Cl^- gate**, compared to Swap.

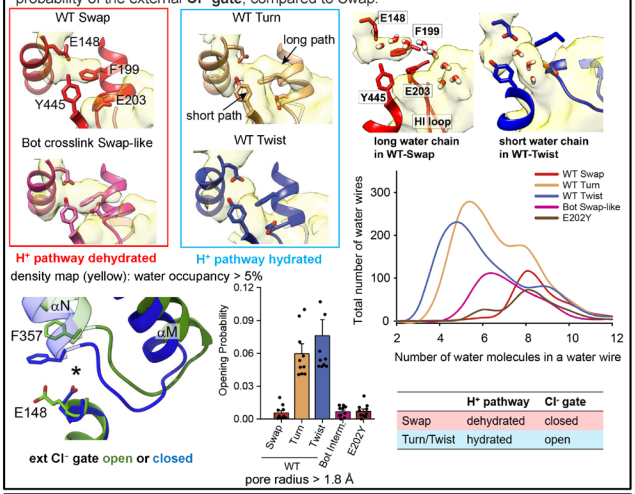

	H^+ pathway	Cl^- gate
Swap	dehydrated	closed
Turn/Twist	hydrated	open

E202Y mutant shows that hydration of H^+ pathway is required for function

- E202Y adopts a single Turn-like conformation with αA disengaged, but inactive
- Y202-Y202 stacking induces displacement of E203 away from H^+ pathway

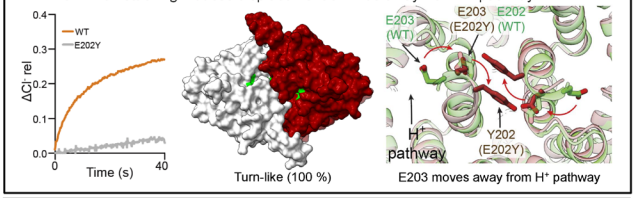

Mutations destabilizing Swap in CLC-ec1 accelerate common gate activation in the mammalian CLC-7 transporter

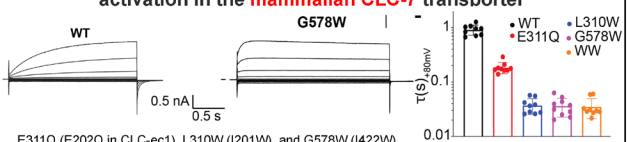

pH dependent activation of CLC

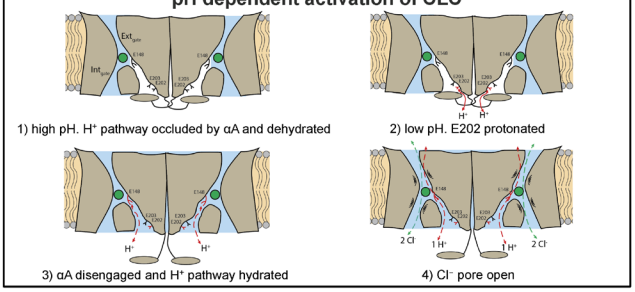

Cryo-EM structures and functional characterization of the human TMEM16E protein and GDD associated mutations

Eleonora Di Zanni[1], Nicole Rychlik[1], Zhang Feng[1], Elizabeth D. Kim[1], Alessio Accardi[1,2,3]

1 Department of Anesthesiology, Weill Cornell Medical College; 2 Department of Biochemistry, Weill Cornell Medical College; 3 Department of Physiology and Biophysics, Weill Cornell Medical College

ABSTRACT

TMEM16E is a transmembrane protein highly expressed in bone tissue and skeletal muscle, indeed different mutations in the human TMEM16E (ANO5 or GDD1) gene are associated with the autosomal dominant bone disease gnathodiaphyseal dysplasia (GDD) or with different recessive forms of muscular dystrophy (LGMD2L, limb-girdle muscular dystrophy-2L and distal MMD3, Miyoshi muscular dystrophy-3). At present, nine GDD-causing TMEM16E/Ano5 mutations have been identified leading to amino acid exchanges at six positions, while more than 70 frameshift, nonsense, insertion, deletion and aberrant splicing mutations have been reported in muscular dystrophy patients. Due to its intracellular localization, it's hard to investigate the function of this protein in its native environment with cell-based assays,-therefore its physiological role is still very unclear. Previous studies have demonstrated that TMEM16E, as other members of the TMEM16s family, is a Ca^{2+} activated phospholipid scramblase.

To better understand TMEM16E physiological role and how it concurs in the pathogenesis of GDD, we resolve the cryoEM structure of the protein in detergent in the absence and presence of Ca^{2+} and we reconstitute the protein into liposome to assess the lipid transport activity of the purified protein.

Our results reveal that while the overall structure is similar to the other proteins of the TMEM16s family, TMEM16E α3 and α4 show a larger tilt towards α6. Surprisingly no structural rearrangements occur upon Ca^{2+} binding, even when all the three Ca^{2+} binding site are occupied. Furthermore, only one Ca^{2+} ion density for each site has been identified in the ligand bound conformation; this observation is in contrast with the presence of two Ca^{2+} ions bound in the other TMEM16 proteins. Nonetheless we find that the TMEM16E is still Ca^{2+} dependence when we test the activity of proteo-liposome in soybean lipids.

As previously reported, GDD-causing mutations have a gain-of-function phenotype showing phospholipid scrambling activity even at basal cytosolic Ca^{2+} concentrations. Here we want to investigate the substitution of Arg582 to Ile, a new GDD mutation that lies in the extracellular loop α5-α6. Our cell-based scrambling assay reveals that R582I mutant has scrambling activity in the absence of Ca^{2+} ionophore, while the WT protein show no activity in the same condition. We are currently expressing and purifying the protein carrying the mutation R582I to investigate which structural rearrangement underlie the activity of the protein in absence of Ca^{2+}.

INTRODUCTION

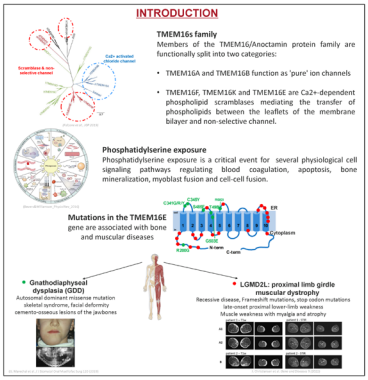

TMEM16s family

Members of the TMEM16/Anoctamin protein family are functionally split into two categories:

- TMEM16A and TMEM16B function as 'pure' ion channels
- TMEM16F, TMEM16K and TMEM16E are Ca2+-dependent phospholipid scramblases mediating the transfer of phospholipids between the leaflets of the membrane bilayer and non-selective channel.

Phosphatidylserine exposure

Phosphatidylserine exposure is a critical event for several physiological cell signaling pathways regulating blood coagulation, apoptosis, bone mineralization, myoblast fusion and cell-cell fusion.

QUESTIONS

1) **What are the structural features of the TMEM16E?**

2) **What are the structural rearrangement associated with GDD mutants?**

METHODS and RESULTS

Protein expression and purification optimization
CryoEM structure of human TMEM16E

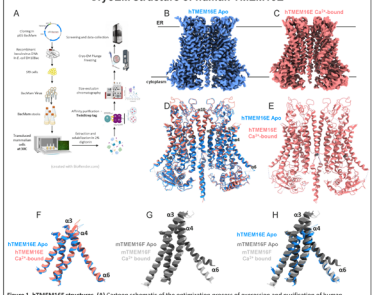

Figure 1. hTMEM16E structures. (A) Cartoon schematic of the optimization process of expression and purification of human TMEM16E protein for CryoEM. Cryo-EM map of hTMEM16E in digitonin in presence (**B**) and absence (**C**) of calcium at 3.3 Å and 3.2 Å, respectively. (**D**) Cartoon representation of a superposition of the Ca^{2+}-bound (light red) and Ca^{2+}-free hTMEM16E (light blue) dimer. Both structures superimpose with a root mean square deviation (RMSD) of 1.2 Å. Transmembrane helices are labelled, and the membrane boundary is indicated. Cryo-EM density of the Ca^{2+}-binding site. (**E**) The difference map (dark grey) between the +Ca^{2+} and 0 Ca^{2+} maps show density only for one Ca^{2+} ion for each binding site.
Comparison of the Ca^{2+}-dependent rearrangements of TMEM16 homologues. (**F**) Superimposition of the α-helices 3–6 between the Ca^{2+}-bound structures of hTMEM16E (light red) and Ca^{2+}-free structure of hTMEM16E (light blue) displaying no structural rearrangement upon Ca^{2+} binding. (**G**) Superimposition of the α-helices 3–6 between the Ca^{2+}-bound structures of mTMEM16F (light gray) and Ca^{2+}-free structure of mTMEM16F (dark grey) showing the bending of TM6 in absence of Ca^{2+}. (**H**) Superimposition of the α-helices 3–6 between mTMEM16F in both Ca^{2+}-bound (light gray) and Ca^{2+}-free (dark grey) state and hTMEM16E in absence of Ca^{2+} (light blue) showing the TMEM16E TM6 in the same conformation of the Ca^{2+} bound TMEM16F.

Phospholipid Scramblase Assay

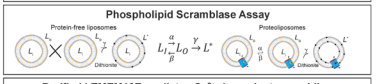

Purified hTMEM16E mediates Ca^{2+}-dependent scrambling

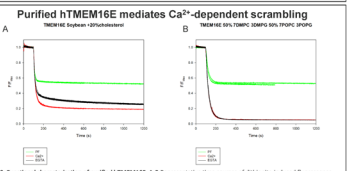

Figure 2. Functional characterization of purified hTMEM16E. A-B Representative time courses of dithionite-induced fluorescence decay in protein-free liposomes (green) or in aTMEM16 proteoliposomes with (red) or without (black) Ca^{2+}. Liposomes were formed from (**A**) soybean polar lipids and cholesterol, or (**B**) in a 50-50 mixture comprised of short chain1,2-dimyristoyl-sn-glycero-3-phosphocholine (DMPC, C14:0) and 1,2-dimyristoyl-sn-glycero-3-phospho-(1'-rac-glycerol) (DMPG, C14:0) and 1,2-dipalmitoleoyl-sn-glycero-3-phosphocholine (16:1), 1,2-dipalmitoleoyl-sn-glycero-3-(1'-rac-glycerol) (16:1) 1-palmitoyl-2-oleoyl-glycero-3-phosphocholine (POPC, 16:0-18:1), POPG (16:0-18:1). A 7.3 PC:PG headgroup ratio was maintained in this mix. Note that the membranes in (**B**) are thinner than those in (**A**) which results in accelerated kinetics of scrambling.

Cell-based phospholipid scramblase assay

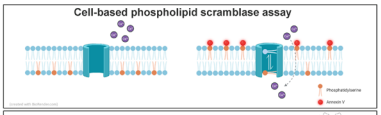

R582I GDD mutation is "constitutively" active in cells

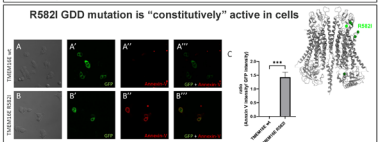

Figure 3. Gain of function mutation leads to scrambling of TMEM16E in absence of Ca^{2+} ionophore. (A – B‴) Confocal images of HEK293 TMEM16F ko cells transfected with (A – A‴) TMEM16E$_{wt}$-GFP wild-type and (B – B‴) p.Arg582Ile (R582I), stained with Alexa555-conjugated Annexin-V in the absence of Ca^{2+} ionophore. (A, B) show transmission light, (A', B') green channel (GFP), (A'', B'') red channel (Alexa555) and (A''', B''') merge of green and red channels. (C) Whereas the TMEM16E wild-type is not scrambling in absence of the Ca^{2+} ionophore, the mutation TMEM16E R582I is showing scrambling activity.

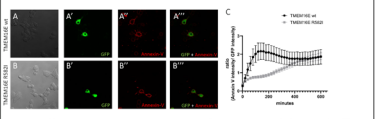

Figure 4. Gain of function mutation leads to a slower scrambling activity of TMEM16E in presence of Ca^{2+} ionophore. (A – B‴) Confocal images of HEK293 TMEM16F ko cells transfected with (A – A‴) TMEM16E$_{wt}$-GFP wild-type and (B – B‴) p.Arg582Ile (R582I), stained with Alexa555-conjugated Annexin-V in the presence of Ca^{2+} ionophore. (A, B) show transmission light, (A', B') green channel (GFP), (A'', B'') red channel (Alexa555) and (A''', B''') merge of green and red channels. (C) Ratio between the Annexin V and GFP intensity show a slower scrambling activity in the mutation of TMEM16E R582I (grey) compared to TMEM16E wild-type (black) in presence of Ca^{2+} ionophore.

SUMMARY and FUTURE DIRECTIONS

Human TMEM16E CryoEM structure

- TMEM16E CryoEM structures do not show any structural rearrangement in the Ca^{2+}-bound conformation.
- We detect density for one Ca^{2+} ion in the orthosteric binding sites located near the TM6 groove. Other TMEM16s homologues have two Ca^{2+} ions in these sites.
- Purified TMEM16E mediates Ca^{2+}-dependent scrambling when reconstituted in proteoliposomes formed from a physiological mix of lipids.
- Scrambling is accelerated by reconstitution in thinner membranes.

GDD associated TMEM16E mutations

- The R582I-GDD mutation, similarly to other GDD mutants, is active in basal Ca^{2+} concentration, resulting in a constitutively active scramblase.
- Currently, we are expressing and purifying the R582I mutant to investigate the structural rearrangement underlying the pathogenesis mechanism of GDD.

Acknowledgements

This work is supported by National Institutes of Health (NIH) Grant R01GM106717 (to A.A).
We would like to thank the New York Structural Biology Center and New York University Langone Health for cryoEM screening and data collection.

Structural basis of closed groove scrambling by a TMEM16 protein

Zhang Feng[1], Omar Alvarenga[2], Alessio Accardi[1,3,4]

1 Department of Anesthesiology, Weill Cornell Medical College; 2 Physiology, Biophysics and Systems Biology Graduate Program, Weill Cornell Medical College; 3 Department of Physiology and Biophysics, Weill Cornell Medical College;
4 Department of Biochemistry, Weill Cornell Medical College

ABSTRACT

Activation of Ca^{2+}-dependent TMEM16 scramblases induces the externalization of phosphatidylserine, a key molecule in multiple signaling processes. Current models suggest that the TMEM16 scramble lipids by deforming the membrane near a hydrophilic groove, and that Ca^{2+} dependence arises from the different association of lipids with an open or closed groove. However, the molecular rearrangements involved in groove opening and of how lipids reorganize outside the closed groove remain unknown. Using cryogenic electron microscopy, we directly visualize how lipids associate at the closed groove of Ca^{2+}-bound nhTMEM16 in nanodiscs. The 2.6 Å resolution of the cryoEM map in the Ca^{2+}-bound closed state enables us to visualize how lipid reorganize outside a closed groove resulting in a pronounced thinning of the membrane that could facilitate scrambling. Structure-based mutagenesis of lipid-interacting residues suggests that residues coordinating outer leaflet lipids have an important role specifically in closed groove scrambling. Structural and functional analyses suggest groove opening entails the sequential appearance of two α-helical turns in the groove-lining TM6 helix. Disruption of a salt bridge connecting two sides of the groove favors a closed groove and prevents formation of the second α-helical turn, suggesting the salt bridge is an important structural feature in groove opening. Finally, we show that the choice of scaffold protein and lipids affects the conformations of nhTMEM16 and their distribution, highlighting a key role of these factors in cryoEM structure determination. Our findings provide the structural basis for closed groove scrambling and reveal how lipid scrambling can occur outside a closed groove by membrane thinning. We speculate this closed groove scrambling could be a universal mechanism for other lipid scramblases without an open groove.

INTRODUCTION

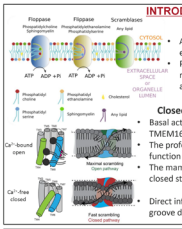

Physiological role of scrambling

- Activated scramblases externalize PS on the extracellular leaflet.
- PS exposure is critical for cell signaling pathways regulating blood coagulation, apoptosis, autophagy and cell-cell fusion.

Closed groove scrambling is supported by

- Basal activity of lipid scrambling is observation in many TMEM16 scramblases when the groove is closed.
- The professional lipid scramblases TMEM16s and Xkrs function as non-selective scramblases
- The mammalian scramblase TMEM16F has a stable closed state.

However…

- Direct information on how lipids interact with a closed groove during scrambling is lacking.

QUESTIONS

1) **How do TMEM16s interact with lipids during scrambling when groove is closed?**
2) **What are the conformational rearrangements critical for groove opening?**

RESULTS

The conformational landscape of nhTMEM16 depends on the environment

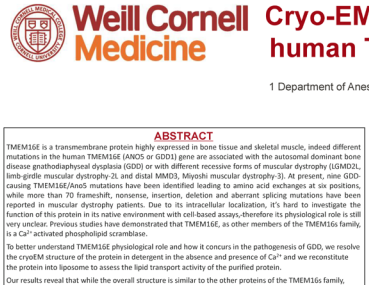

Figure 1. Cryo-EM structures of nhTMEM16 in the MSP1E3 and MSP2N2 nanodiscs. A-E. Cryo-EM maps of nhTMEM16 in nanodiscs formed from a 7:3 mix of DOPC:DOPG lipids and MSP1E3 (**A-C**) or MSP2N2 (**D-E**) scaffold proteins. (**A**) Ca^{2+}-free, closed groove, (**B**) Ca^{2+}-bound, closed groove, (**C**) Ca^{2+}-bound, open groove, (**D**) Ca^{2+}-bound, intermediate-open groove, and (**E**) Ca^{2+}-bound, open groove. **F-I.** The groove in the different conformations is viewed from the plane of the membrane. Ca^{2+} ions are shown as green spheres. **K.** The percentage of particles with a closed (black bar), intermediate (gray bar), or open (white bar) groove conformation in the datasets of Ca^{2+}-bound nhTMEM16 in MSP1E3 or MSP2N2 nanodiscs. Here, intermediate does not distinguish between the intermediate-open and -closed conformations. **L.** The accessibility of the permeation pathway of nhTMEM16 in the intermediate conformation is visualized using the program Hole. **M.** The inner diameter of the permeation pathway of nhTMEM16 in MSP1E3 or MSP2N2 nanodiscs and in the published the diameter of a putative ion conduction pathway measured in different states with Hole.

Structural basis of membrane thinning at the closed groove of nhTMEM16

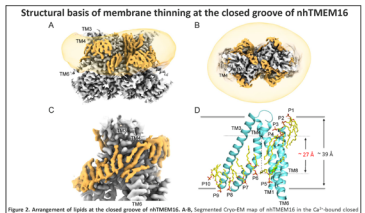

Figure 2. Arrangement of lipids at the closed groove of nhTMEM16. A-B, Segmented Cryo-EM map of nhTMEM16 in the Ca^{2+}-bound closed state (gray) and the associated lipids (orange) viewed from the membrane plane (**A**) and from the extracellular side (**B**). The map showing the density of the nanodisc membrane is low-pass filtered to 10 Å and shown in transparent orange. **C,** View of the lipids outside of the closed groove from the plane of the membrane. **D,** Stick representation of the tan pathway lipids colored in yellow (P1-P10). Dashed arrow indicates the distance between the phosphate atoms of the last lipid from the inner (P6) and outer (P4) leaflets (~27 Å) and the measured membrane thickness (~39 Å). Lipids were built up to the phosphate atom in the head. Ca^{2+} ions are displayed as green spheres.

1) There is a pronounced thinning of the membrane at the closed groove

Interactions important for closed –but not open– groove scrambling

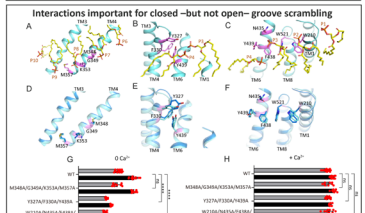

Figure 3. Identification of residues important for the closed groove scrambling. A-C, Residues coordinating the P7-P9 (**A**), P3-P4 (**B**) and P2-P4 lipids (**C**) in the Ca^{2+}-bound closed state. **D-F:** Superposition of the Ca^{2+}-bound closed state (aquamarine) to apo state (blue) with lipid-coordinating residues shown as sticks. **G-H,** Forward (a) and reverse (β) scrambling rate constants of the mutants of nhTMEM16 aimed at disrupting the protein-lipid interactions (shown in **A-C**) measured in 0 (Ca^{2+}) or 0.5 mM Ca^{2+} (**H**). Bars are averages for α (black) and β (grey) (N ≥ 3), error bars are 3. Dev., and red circles are values from individual repeats. The statistical significance of the effects of the mutants on the scrambling rate constants was evaluated with a two-sided Student's t-test with a Bonferroni correction. **** denotes p<10^{-4} after Bonferroni correction.

2) Lipid interacting residues at outer leaflet are important for closed-groove scrambling

Steps in groove opening of nhTMEM16

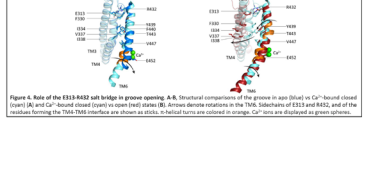

Figure 4. Role of the E313-R432 salt bridge in groove opening. A-B, Structural comparisons of the groove in apo (blue) vs Ca^{2+}-bound closed (cyan) (**A**) and Ca^{2+}-bound closed (cyan) vs open (red) states (**B**). Arrows denote rotations in the TM6. Sidechains of E313 and R432, and of the residues forming the TM4-TM6 interface are shown as sticks. α-helical turns are colored in orange. Ca^{2+} ions are displayed as green spheres.

Disruption of the E313-R432 salt bridge favors a closed groove

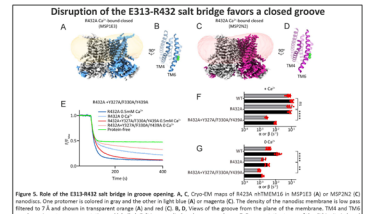

Figure 5. Role of the E313-R432 salt bridge in groove opening. A, C, Cryo-EM maps of R425A nhTMEM16 in MSP1E3 (**A**) or MSP2N2 (**C**) nanodiscs. One protomer is colored in gray and the other in light blue (**A**) or magenta (**C**). The density of the nanodisc membrane is low pass filtered to 7 Å and shown in transparent orange (**A**) and red (**C**). **B, D,** Views of the groove from the plane of the membrane. TM4 and TM6 are shown in cartoon representation and labelled. Ca^{2+} ions are displayed as green spheres. **E,** Representative traces of the dithionite induced fluorescence decay in the scrambling assay for protein free liposomes (green), or R432A nhTMEM16 and the quadruple mutant R432A+Y327A/F330A/Y439A nhTMEM16 in the presence (dark blue and dark red) and absence (light blue and light red) of Ca^{2+}. **F-G,** Forward (a) and reverse (β) scrambling rate constants of the mutants measured in 0.5 mM (**F**) or 0 Ca^{2+} (**G**). Bars are averages for α (black) and β (grey) (N ≥ 3), error bars are 5. Dev., and red circles are values from individual repeats. The statistical significance of the effects of the mutants on the scrambling rate constants was evaluated with a two-sided Student's t-test with a Bonferroni correction. **** denotes p<10^{-4} after Bonferroni correction.

Straightening of TM6 is important for closed-groove scrambling

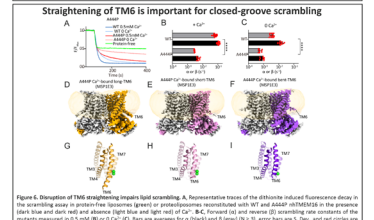

Figure 6. Disruption of TM6 straightening impairs lipid scrambling. A, Representative traces of the dithionite induced fluorescence decay in the scrambling assay in protein-free liposomes (green) or proteoliposomes reconstituted with WT and A444F nhTMEM16 in the presence (dark blue and dark red) and absence (light blue and light red) of Ca^{2+}. **B-C,** Forward (a) and reverse (β) scrambling rate constants of the mutants measured in 0.5 mM (**B**) or 0 Ca^{2+} (**C**). Bars are averages for α (black) and β (grey) (N ≥ 3), error bars are 3. Dev., and red circles are values from individual repeats. The statistical significance of the effects of the mutants on the scrambling rate constants was evaluated with a two-sided Student's t-test with a Bonferroni correction. **** denotes p<10^{-4} after Bonferroni correction. **D-I,** Cryo-EM maps of A444F nhTMEM16 in MSP1E3 nanodiscs in the long TM6 state (**D**), short TM6 state (**E**) and bent TM6 state (**F**). One protomer is colored in gray and the other in orange (**D**), pink (**E**), and purple (**F**). The density of the nanodisc membrane is low pass filtered to 7 Å and shown in transparent orange. **G-I,** The groove in the long TM6 (**G**), short TM6 (**H**) and bent TM6 (**I**) states is viewed from the plane of the membrane. Transmembrane helices are labelled and Ca^{2+} ions are displayed as green spheres.

CONCLUSIONS

- We used cryoEM to image the fungal nhTMEM16 scramblase in lipid nanodiscs formed from different scaffold proteins and found this to affect both the conformations adopted by nhTMEM16 and their distribution.
- The 2.64 Å resolution structure of Ca^{2+}-bound closed nhTMEM16 reveals how lipids arrange near the groove, thus showing how the scramblase thins the membrane outside a closed groove.
- Mutating residues that coordinate outer leaflet lipids near the closed groove impairs scrambling only in the absence of Ca^{2+}, suggesting these interactions play a specific role in closed-groove scrambling.
- Structural analysis of the transition of nhTMEM16 from closed to open state suggests that the E313-R432 salt bridge could be involved in groove opening. Disruption of this interaction by the R432A mutation trapped nhTMEM16 in a closed-groove conformation, suggesting the salt bridge is critical for groove opening.

Acknowledgements

The authors thank members of the Accardi lab, Harel Weinstein and George Khelashvili for helpful discussions and suggestions. The work was supported by National Institutes of Health (NIH) Grant R01GM106717 (to A.A.). Some of this work was performed at the Simons Electron Microscopy Center and National Resource for Automated Molecular Microscopy located at the New York Structural Biology Center, supported by grants from the Simons Foundation (SF349247), NYSTAR, and the NIH National Institute of General Medical Sciences (GM103310). Part of the work was performed at NYU Langone Health's Cryo-Electron Microscopy Laboratory (RRID: SCR_019202) with the help of Dr. Bing Wang and Dr. William Rice, and at the Cryo-EM Core Facility at Weill Cornell Medical College with the help of Dr. Carl Fluck. Initial screening was performed at NYU Langone Health's Cryo-Electron Microscopy Laboratory (RRID: SCR_019202) and the Cryo-EM Core Facility at Weill Cornell Medical College.

Clinical Research Studies

1. **Evaluation of Wearables for Preoperative Cardiorespiratory Fitness Screening and Risk Stratification in Geriatric Surgery**
   PI: *Richard Boyer, MD, PhD*
   Protocol #: 21-04023531
   This prospective, observational clinical study tests the hypothesis that wearable measurements of cardiorespiratory fitness (CRF) are predictive of postoperative complications in older adult patients undergoing major surgery.

2. **Identifying Neurocognitive Outcomes and Electroencephalography Correlates in Elderly Patients Following Transcatheter Aortic Valve Replacement Performed Under Sedation: A Pilot Study**
   PI: *Diana Khatib, MD*
   Protocol #: 21-01023123
   The overall purpose of this pilot study is to examine the incidence and prevalence of post-operative delirium (POD) and associated neurocognitive changes in patients undergoing transcatheter aortic valve replacement (TAVR) procedures and additional procedures under monitored anesthetic care (MAC). Additionally, Sedline EEG monitoring and recording are completed during the procedure to explore the possible correlation between intraprocedural EEG changes and the development of neurocognitive changes.

3. **A Sequenced Strategy for Improving Outcomes in People with Knee Osteoarthritis Pain (SKOAP)**
   PI: *Neel Mehta, MD*
   Protocol #: 20-09022645
   Multi-center, randomized, controlled trial with two phases investigating both non-invasive treatments, including physical therapy and duloxetine, as well as minimally invasive treatments, including steroid injections, GNB, and RFA, to treat knee osteoarthritis pain. In collaboration with John's Hopkins University and Duke University.

4. **A 5-year Superion(R) IDS Clinical Outcomes Post-Approval Evaluation (SCOPE)**
   PI: *Neel Mehta, MD*
   Protocol #: 21-04023564
   This is a prospective, multi-center, single-arm observational post-approval study to compile real-world outcomes as well as evaluate the safety and effectiveness of the Superion® IDS in routine clinical practice. The Superion® IDS is a FDA approved non-fusion, spinal column load-sharing device that uses "indirect" compression to stabilize the spine for patients with lumbar spinal stenosis.

5. **PROtective ventilation with high versus low PEEP during one-lung ventilation for THORacic surgery - PROTHOR: A randomized control trial**
   PI: *Matthew Murrell, MD, PhD*
   Protocol #: 17-01017890
   Multi-center, randomized, controlled trial investigating the use of a higher or lower PEEP strategy in reducing postoperative pulmonary complications in patients undergoing thoracic surgery with one-lung ventilation. In collaboration with Technische Universität Dresden.

6. **Impact of surgical revascularization strategy on left ventricular function, myocardial perfusion and clinical outcomes**
   PI: *Lisa Rong, MD, MSCE, FASE, FACC*
   Protocol #: 21-05023605
   This is a prospective study designed to test the central hypothesis that early improvement in myocardial strain will be less with multiple arterial grafting (MAG) than single arterial grafting (SAG) (stemming from less initial increase in myocardial perfusion) requiring increased pharmacologic support (vasopressor and inotropes), and that early LV strain recovery will predict better clinical outcomes than conventional indices (LV ejection fraction, volume).

7. **Non-Invasive Monitoring of Brain Activity in Altered Conscious States**
   PI: *Seyed A. Safavynia, MD, PhD*
   Protocol #: 18-01018908
   This study will use functional near-infrared spectroscopy (fNIRS) and electroencephalography (EEG) to monitor brain activity in delirious and lucid states during recovery from general anesthesia. By analyzing hemodynamic and electrical activity within the brain, we will quantify differences in cerebral hemodynamics and cortical connectivity during episodes of PACU delirium. This study is sponsored by the Foundation for Anesthesia Education and Research and the Charles A. Frueauff Foundation.

8. **Machine Learning-Backed Contactless Sensors to Estimate Frailty and Predict Postoperative Outcomes**
   PI: *Joseph Scarpa, MD, PhD*
   Protocol #: 21-01023137
   A feasibility study that aims to assess the predictive capability and social acceptability of contactless sensors (depth cameras and floor-mounted accelerometers) to predict frailty and postoperative outcomes. In collaboration with Virginia Tech Civil and Environmental Engineering.

9. **Frailty and Autonomic Dysfunction as Predictors of Intra- and Post-operative Morbidity: A Prospective Study**
   PI: *Julia Scarpa, MD, PhD*
   Protocol #: 22-03024487
   The overall objective of this prospective, observational study is to determine the role of preoperative frailty and autonomic dysfunction on perioperative hemodynamic stability and morbidity. Subjects will complete questionnaires and will be monitored with an ambulatory physiologic research device (NINscan) throughout the preoperative evaluation, the intraoperative course, and the immediate postoperative period to assess cardiovascular stability, cerebrovascular parameters, and perfusion-related morbidity. We hypothesize that preoperative frailty and autonomic function classifications will correlate with increased incidence and severity of perioperative hemodynamic instability and morbidity.

Chart, Observational, & Survey Studies

1. **Low Dose Naltrexone (LDN) Dosing Regimen and Side Effect Patient Survey**
   PI: *Neel Mehta, MD*
   Protocol #: 22-11025360
   This study uses a survey questionnaire to gather information about LDN dosing regimens and side effects, and which chronic pain conditions LDN was prescribed for.

2. **Delayed Recovery of Consciousness after Anesthetic Coma in Survivors of COVID-19 Hypoxemic Respiratory Failure**
   PI: *Seyed A. Safavynia, MD, PhD*
   Protocol #: 20-08022490
   A retrospective analysis of clinical data from critically-ill NewYork-Presbyterian/Weill Cornell COVID-19 patients, with a primary aim to characterize functional neurophysical changes associated with delayed recovery of consciousness in severe COVID. In collaboration with the Columbia University Irving School of Medicine and sponsored by the JumpStart Research Career Development Grant.

3. **Preoperative Transglomerular Gradient and the Risk of Developing AKI in Patients undergoing Elective Cardiac Surgery: The PRO - AKI study**
   PI: *Ankur Srivastava, MD*
   Protocol #: 22-03024560
   The primary objective of this study is to investigate the effect of the preoperative transglomerular pressure gradient on the development of acute kidney injury (AKI) in patients undergoing elective cardiac surgery. The secondary objective of this study is to investigate the effects of preoperative pulmonary artery pressure, cardiac output, cardiac index, anemia, and MAP on the development of AKI in patients undergoing elective cardiac surgery.

4. **Patients Perspectives on Non-Utilization of Neuraxial Labor Analgesia During Labor and Delivery**
   PI: *Robert White, MD, MS*
   Protocol #: 22-05024854
   A qualitative study that utilized open-ended individual interviews to understand patient-level factors (ex: maternal age, education, culture, pain perception, and parity) for declining or waiving access to neuraxial labor analgesia during labor and delivery. Sponsored by the Foundation for Anesthesia Education & Research.

5. **Applying the Patient Priorities-Aligned Decision-Making Model in a Pain Management Setting**
   PI: *Lisa Witkin, MD*
   Protocol #: 22-08025126
   This study utilized an anonymous Qualtrics survey to evaluate the attitudes, preferences, and beliefs regarding patient-centered care models of board-certified pain management physicians across the country from a variety of backgrounds and practice settings as well as their willingness to adopt a patient priorities model.

Registry Studies

1. **Leveraging ROTEM to Greater Advantage**
   PI: *Meghann Fitzgerald, MD, Andrew Milewski, MD, PhD*
   Protocol #: 23-08026373
   This protocol establishes a retrospective and prospective registry of ROTEM curves and coagulation profiles from ROTEM tests performed across this institution. Through a variety of analytical and machine-learning approaches, we aim to develop algorithms that predict the trajectories of ROTEM curves in real time to enable early estimation of ROTEM parameters and, consequently, to accelerate decisions making for targeted transfusion therapy in bleeding patients.

2. **Weill Cornell Center for Human Rights Registry**
   PI: *Gunisha Kaur, MD, MA*
   Protocol #: 18-10019677
   This study aims to create a database for clients seeking services at the Weill Cornell Center of Human Rights (WCCHR).

3. **Pediatric Craniofacial Surgery Perioperative Registry (PCSPR)**
   PI: *Jennifer Lee, MD*
   Protocol #: 15-04016130
   Multi-center registry to capture information relating to the perioperative course and management of children undergoing craniofacial reconstructive surgery. The aggregate multi-institutional data set will be used for benchmarking for national quality improvement efforts. In collaboration with the
   Children's Hospital of Philadelphia.

4. **Spinal Cord Stimulator Implant Registry**
   PI: *Neel Mehta, MD*
   Protocol #: 18-11019714
   We propose the creation of a registry that looks to collect longitudinal data from the approx 300-400 patients pre- and post-implantation of SCS currently treated by the Pain Management clinic. We intend to present collect over the lifetime of the device and include factors like trends comparing efficacy against various diagnoses, opioid use and pain scores.

5. **Pediatric Difficult Intubation (PeDI) Registry - Improving Safety and Quality of Airway Management in Children with Difficult Airways**
   PI: *Jasmine Patel, MD*
   Protocol #: 16-02016988
   Observational, multi-center study data collection to establish a registry that will allow participating institutions to assess the outcomes of care of children with Difficult Direct Laryngoscopy (DDL) and to facilitate comparison to the other institutions' difficult airway management practices and outcomes. In collaboration with the Children's Hospital of Philadelphia.

6. **Perioperative Transesophageal Echocardiography Registry**
   PI: *Lisa Q. Rong, MD*
   Protocol #: 17-08018484
   The goal of this study is to establish a retrospective and prospective pre-, intra-, and postoperative anesthesia echocardiography data registry for subjects who have received anesthesia services for cardiac surgery with intraoperative transesophageal echocardiography at New York-Presbyterian Hospital/Weill Cornell Medical College since 2010.

7. **Chronic Pain Registry**
   PI: *Lisa Witkin, MD*
   Protocol #: 17-05018203
   To establish a retrospective chronic pain patient data registry for patients with chronic pain, and to use the patient data registry, Practice Based Evidence (PBE), and Clinical Practice Improvement (CPI) methodology to identify specific pain management interventions that are most effective for specific patient types with chronic pain.

8. **The Development and Implementation of a Collaborative Health Outcomes Information Registry for the Weill Cornell Multidisciplinary Spine Center**
   PI: *Lisa Witkin, MD*
   Protocol #: 17-01017897
   This study aims to develop and implement a patient-reported outcomes data collection system for the Weill Cornell Center for Comprehensive Spine Care. Ideally, this will allow ongoing treatment to be determined by the patients' response and progress and can improve evidence-based medicine guidance of treatment. Sponsored by the Applebaum Foundation.

Global Health Studies

1. **Assess Chronic Pain Diagnosis and Treatment in Torture Survivors**
   PI: *Gunisha Kaur, MD, MA*
   Protocol #: 20-10022730
   The goal of this 3-part study is to characterize the diagnosis of chronic pain in torture survivors. This investigation is funded by the National Institutes of Health K23 Grant.

   Aim 1: Study Aim 1 assesses whether the application of a validated pain screen, the Brief Pain Inventory Short Form, can supplement the United Nations Istanbul Protocol and improve its sensitivity for pain detection, as compared to the gold standard (a pain specialist evaluation).

   Aim 2: This sub-study aims to qualitatively assess the challenges and acceptability of our proposed, evidence-based somatic pain treatment model - physical therapy and/or non-opioid analgesics and/or trigger point injections - and to receive feedback in terms of challenges, limitations, and acceptability of the interventions.

   Aim 3: This sub-study aims to assess the feasibility of recruiting and retaining participants in a digital pain treatment program over six months by enrolling 20 participants into a digital program of pain, stress, and cardiovascular health monitoring.

Education Studies

1. **Experiential Curriculum for Communication and Professionalism in Anesthesiology**
   PI: *June Chan, MD*
   Protocol #: 1807019387
   This study is a retrospective analysis of data collected during the course of established curricular activities mandated by the Weill Cornell Anesthesiology Education division to evaluate its trainees.

2. **The impact of COVID-19 on the clerkship experience: a quantitative study of perspectives on telehealth, remote learning, and binary grading in clinical education**
   PI: *Dana Gurvitch, MD*
   Protocol #: 21-01023250
   To evaluate student perspectives on remote education, telehealth curricula, and binary grading during the COVID-19 pandemic to empower future curricular interventions.

3. **Pain Simulation Education Curriculum**
   PI: *Daniel Pak, MD*
   Protocol #: 22-01024333
   The purpose of this project is to collect and analyze the outcome measures of the Weill Cornell Tri-Institutional Pain Fellows in using a spine simulator model on several different simulated procedures and analyze this information to measure milestones and evaluate their performance throughout the year. In addition, survey responses pre-session and post-session will be used to collect feedback from the fellows.

4. **Anesthesiology Education Research Registry**
   PI: *Kane Pryor, MD*
   Protocol #: 14-03014915
   To design and establish a registry to assess the utility of various metrics in predicting anesthesiology resident performance outcomes.

5. **Teaching Anesthetic Induction and Intubation to Anesthesiology Interns Using Simulation**
   PI: *Liang Shen, MD*
   Protocol #: 20-02021466
   This study will aim to determine the efficacy of using structured simulation for teaching anesthesiology interns the procedures of anesthetic induction and endotracheal intubation.

Center for Perioperative Outcomes Studies

1. **Multicenter Perioperative Outcomes Group (MPOG) and Anesthesiology Performance Improvement and Reporting Exchange (ASPIRE) Performance Site**
   PI: *Hugh C. Hemmings, MD, PhD*
   Protocol #: 12-08012817
   The primary objective of this study is to assess the impact of provider feedback on anesthesiology quality measures on patient outcomes. This project will provide WCM and BMH Anesthesiologists with individualized feedback of their performance on anesthesiology quality metrics. Their individualized performance is based on information extracted from the anesthesia information management system (AIMS). This feedback, given on a monthly basis, will hopefully lead to positive behavior changes among the anesthesiology providers, which will result in better care for patients.

2. **Primary Graft Dysfunction in the Black Heart Transplant Recipient with SDOH**
   PI: *Mandisa Jones, MD*
   Protocol #: 23-03025844
   The proposed study will explore risk factors associated with primary graft failure in Black heart transplant recipients and assess the contribution of severe primary graft failure to in hospital and one year mortality in this population. The primary outcome is a binary measure of primary graft failure within 24 hours of transplant. Secondary outcomes are mortality during the transplant admission and mortality in the first-year post-transplant.

3. **Reference values for post-induction hemodynamic measures in pediatric patients undergoing general anesthesia for non-cardiac surgery**
   PI: *Kane O. Pryor, MD*
   Protocol #: 23-02025736
   The primary objective of this study is to define reference ranges for intraoperative hemodynamic measures (heart rate, systolic blood pressure, diastolic blood pressure) for pediatric patients classified as ASA-PS 1 or 2 and undergoing general anesthesia for both operative and non-operative non-cardiac procedures according to age group, sex, and body temperature. The primary goal is to develop a holistic hemodynamic reference standard for use in the intraoperative setting.

4. **Multicenter Analysis of Benzodiazepine Use in Patients Undergoing Non-Operating Room Cardiac Procedures**
   PI: *Lisa Q. Rong, MD*
   Protocol #: 22-04024670
   In this retrospective cohort study, we use a multicenter perioperative electronic medical record data to identify practice patterns regarding benzodiazepine use in non-operating room cardiac procedures that require anesthetic management. We hypothesize that patient, clinician, and institutional factors will be independently associated with benzodiazepine use during non-operating room anesthesia (NORA) procedures, and the majority of the variation in benzodiazepine use will be explained by institution and clinician rather than patient factors.

5. **Evaluation of a Novel Patient Monitor in the Perioperative Setting**
   PI: *Zachary A. Turnbull, MD, MBA, MS*
   Protocol #: 22-05024803
   This is a dual-center, pre-/post-, observational study. In this proposed study, we aim to evaluate the impact of a novel patient monitor, known as the Philips Visual Patient Monitor (VP), on deviations from expected physiologic ranges. This novel monitor, which was developed in a collaboration between faculty at University of Zurich Hospital and Philips, features a patient aviator to provide visual cues for common physiologic deviations, such as bradycardia.

6. **SONAR: Perioperative Readiness Tool?**
   PI: *Zachary A. Turnbull, MD, MBA, MS*
   Protocol #: 23-01025642
   Our study seeks to leverage SONAR (an acronym for Surgery, Operating Room, Preoperative Nursing, Anesthesia, Preoperative Complete), an electronic tool in Epic that visually tracks preoperative readiness, to improve first case on time start rates and the case turnover time by allowing care teams to proactively be aware of and identify gaps in OR case preparation.

7. **The impact of team familiarity on operational efficiency and postoperative outcomes**
   PI: *Zachary A. Turnbull, MD, MBA, MS*
   Protocol #: 23-09026546
   The primary objective of this study is to quantitatively measure the relationship between team familiarity and operational efficiency and postoperative outcomes. Team familiarity will be defined as how often attending anesthesiologists and surgeons have worked together. Our aim is to study the relationship between team familiarity and (1) Operational efficiency which will focus on post-operative time points (procedure end to anesthesia end time) and (2) PACU outcomes (LOS and pain control measurements).

8. **Health Disparities in Obstetrical Care and Delivery Outcomes Before and After Implementation of an Enhanced Recovery After Surgery Protocol**
   PI: *Robert S. White, MD, MS*
   Protocol #: 21-10024035
   The first aim of this study is to study the effect that Enhanced Recovery After Surgery for cesarean delivery (ERAS-CD) implementation has on postoperative complications and readmissions after planned and unplanned cesarean deliveries. We also plan to analyze the impact of patient race/ethnicity, spoken language, and insurance status on postoperative complications and readmissions.

9. **MPOG: Racial disparities in cesarean delivery anesthesia type by race/ethnicity and social determinants of health**
   PI: *Robert S. White, MD, MS*
   Protocol #: 23-04025937
   The overall purpose of this study is to use the MPOG database to examine if patient race/ethnicity is associated with the type of anesthesia (general or regional) administered in cesarean deliveries. Our primary covariate of interest is recorded patient race/ethnicity (unordered: white [reference category], Black, Hispanic, Other, or Unknown). Other patient-level variables that will be abstracted for each admission include demographic information (age; ASA PS classification system score 1-6) and a validated obstetric comorbidity index used to predict maternal end-organ injury or inpatient mortality, which has also been shown to predict general anesthesia for cesarean delivery use.

10. **Multicenter Perioperative Outcomes Group (MPOG) Geo-Coding and Sensitivity of ASPIRE Process Metrics to Social Determinants of Health**
    PI: *Robert S. White, MD, MS*
    Protocol #: 23-07026284
    This is a multicenter, retrospective study. We will use quantitative methods to investigate individual clinicians' equitable adherence with guidance-congruent surgical care. Our hypotheses are (1) Patient Black race predicts passing a composite of certain ASPIRE metrics and (2) Census tract-level (CT-level) social determinants of health (SoDH) "Neighborhood disadvantage" (ND) predicts passing ASPIRE metrics.

11. **The Development and Implementation of a Collaborative Health Outcomes Information Registry (CHOIR) for the Weill Cornell Multidisciplinary Spine Center**
    PI: *Lisa Witkin, MD, MS*
    Protocol #: 17-01017897
    This study aims to develop and implement a patient-reported outcomes data collection system for the Weill Cornell Center for Comprehensive Spine Care. Ideally, this will allow ongoing treatment to be determined by the patients' response and progress to improve evidence-based medicine guidance of treatment.

Upcoming Studies

1. **The PROTECT Trial: PeRiOperTive Enhancement of Cognitive Trajectory**
   PI: *Lisbeth Evered, PhD*
   Protocol #: Pending
   The primary aim of this multisite, prospective, pragmatic, randomized controlled trial is to demonstrate that older people (65 years and over) who undergo supported perioperative optimization strategies have a decreased incidence of perioperative neurocognitive disorders (PND) over 3 months compared to people who receive standard care. Patients will be randomized to receive perioperative optimization (treatment arm) or current standard of care (control arm). Both study groups will undergo daily delirium assessments throughout the postoperative period, alongside evaluation of perioperative neurocognitive disorder at baseline and three and 12 months postoperatively.

2. **PDN-SENSORY: A Multi-Center Randomized Controlled Trial to Evaluate Pain and Neurological Function with 10 kHz SCS in Treatment of Painful Diabetic Neuropathy**
   PI: *Neel Mehta, MD*
   Protocol #: 23-03025839
   This is a prospective, multi-center, randomized controlled trial to evaluate changes in pain and neurological function with 10 kHz spinal cord stimulation (SCS) therapy in patients with chronic, intractable lower limb pain associated with diabetic peripheral neuropathy, a condition known as painful diabetic neuropathy (PDN). Subjects will be randomized to conventional medical management (CMM) or 10 kHz SCS plus CMM.

3. **Trajectories of Recovery after Intravenous propofol versus inhaled VolatilE anesthesia (THRIVE) trial**
   PI: *Kane Pryor, MD*
   Protocol Number #: 23-09026456
   Multi-institutional randomized, control trial in order to compare patient experience, safety, and recovery after receiving intravenous or volatile gas anesthesia. In collaboration with The University of Michigan and Washington University in St. Louis.

4. **PENG vs Femoral Block for Hip Fracture Pain in the Emergency Department, A Pragmatic Cluster Crossover Trial**
   PI: *Tiffany Tedore, MD*
   Protocol #: Pending
   This cluster crossover study plans to compare the efficacy of the PENG block to the femoral block for the reduction in hip fracture pain prior to surgery and determine whether the blocks have different efficacy in intracapsular versus extracapsular hip fractures.

5. **Assessment of Preoperative Gastric Content with Ultrasound in Patients taking GLP1 Agonists**
   PI: *Marissa Weber, MD*
   Protocol Number #: 23-09026457
   Prospective study investigating delayed gastric emptying in surgical patients taking GLP1 agonists. Point-of-Care Gastric Ultrasound (POCUS) will be used to investigate the presence of full stomach preoperative in these patients. In collaboration with the Hospital for Special Surgery.

Recruitment Completed Studies

1. **Cognitive and Functional Consequences of COVID-19**
   PI: *Lisbeth Evered, PhD*
   Protocol #: 20-08022498
   This is an observational pilot study that will utilize responses from an online survey completed by COVID-19 positive patients to identify the rate of cognitive decline, disability and psychological factors in COVID-19 positive patients at 6-24 months post positive test and determine a severity-response in outcomes between those who were treated as outpatients vs ward inpatients vs ICU intubated and ventilated patients.

2. **Self-Management of Chronic Pain Using PainDrainer**
   PI: *Neel Mehta, MD*
   Protocol #: 19-04020168
   The proposed clinical investigation is a single-arm open concept trial (SAC) to evaluate if PainDrainer, a digital pain coach based on artificial intelligence (AI), will improve the self-management of chronic pain and increase quality of life. In collaboration with Lund University.

3. **Carotid Doppler Imaging Correlation with Pulmonary Artery Catheters As A Marker For Fluid Responsiveness**
   PI: *James Osorio, MD*
   Protocol #: 19-11021076
   This prospective pilot study evaluates the use of carotid doppler imaging, specifically measuring carotid blood flow, corrected carotid flow time, and respiratory variation in peak carotid velocity, to assess if these measures can be used as a reliable marker for fluid responsiveness when compared to the use of Pulmonary Artery catheters in mechanically ventilated, postoperative cardiac surgery patients.

4. **Pilot Study: Determining the Presence of Perioperative Optic Nerve Sheath Diameter Changes after Cardiac Surgery**
   PI: *James Osorio, MD*
   Protocol #: 19-09020866
   The primary objective of this study is to assess if there is an increase in optic nerve sheath diameter (ONSD) after cardiac procedures. Additionally, as a secondary objective, the study is evaluating if an increase in ONSD may be associated with an increased risk of postoperative delirium.

5. **A Randomized Controlled Study to Evaluate the Safety and Effectiveness of Boston Scientific Spinal Cord Stimulation (SCS) Systems in the Treatment of Chronic Low Back and/or Leg Pain with No Prior Surgeries (WaveWriter-SOLIS)**
   PI: *Daniel Pak, MD*
   Protocol #: 21-04023563
   This prospective, multi-center randomized controlled trial with a parallel group design evaluates the safety and effectiveness of the Boston Scientific WaveWriter Spinal Cord Stimulation (SCS) Systems with multiple modalities compared to Conventional Medical Management (CMM) in patients with chronic low back and/or leg pain who have not undergone spinal surgery.

6. **Benzodiazepine-free cardiac anesthesia for the reduction of postoperative delirium (B-Free)**
   PI: *Kane Pryor, MD*
   Protocol #: 19-11021136
   Pragmatic, multicenter, cluster crossover trial to evaluate whether a policy limiting the use of intra-operative benzodiazepine (B-Free) reduces postoperative delirium when compared with a policy of liberal benzodiazepine administration. The trial is run by the Population Health Research Institute (PHRI) and is endorsed by the Canadian Perioperative Anesthesia Clinical Trials group. The study is funded by the Canadian Institutes of Health Research (CIHR).

7. **Optimisation of Perioperative Cardiovascular Management to Improve Surgical Outcome II (OPTIMISE II) Trial**
   PI: *Kane Pryor, MD*
   Protocol #: 18-04019164
   An open, international, multi-center, randomized controlled trial of cardiac output-guided fluid therapy with low dose inotrope infusion compared to standard of care in subjects undergoing major elective gastrointestinal surgery. Sponsored by Queen Mary University of London.

8. **A Survey of Obstetrical Anesthesia Health Equity Practices at Academic Centers in the United States (US)**
   PI: *Robert White, MD, MS*
   Protocol #: 22-09025245
   This study utilized an internet-based Qualtrics survey questionnaire to collect qualitative information regarding obstetrical anesthesia practice patterns concerning healthcare disparities and efforts to address these disparities on the labor and delivery unit. (Sponsored by the Foundation for Anesthesia Education & Research).

9. **Physicians' Perspectives and Utilization of Patient-Reported Outcomes to Guide Clinical Decision-Making**
   PI: *Lisa Witkin, MD*
   Protocol #: 22-01024354
   This qualitative study used semi-structured interviews to evaluate the implementation of an electronic patient-reported outcomes registry in the pain management division of Weill Cornell Medicine in order to understand providers' beliefs and experiences using the data and how it affects their patient interaction, discussion, and guides their clinical decision-making.